# Interfacial Rheology of Globular Proteins

by

Aditya Jaishankar

B. Tech., Mechanical Engineering, 2009, Indian Institute of Technology Madras (Chennai, India)
Minor Chemistry

Submitted to the Department of Mechanical Engineering in partial fulfillment of the requirements for the degree of

Master of Science in Mechanical Engineering

at the

MASSACHUSETTS INSTITUTE OF TECHNOLOGY

June 2011





Author .....
Department of Mechanical Engineering
May 20, 2011

Certified by .....
Gareth H. McKinley
Professor, Mechanical Engineering
Thesis Supervisor

Accepted by .....
David E. Hardt
Graduate Officer, Department Committee on Graduate Students

# Interfacial Rheology of Globular Proteins

by

Aditya Jaishankar

Submitted to the Department of Mechanical Engineering
on May 20, 2011, in partial fulfillment of the
requirements for the degree of
Master of Science in Mechanical Engineering

## Abstract

Protein-surfactant mixtures appear in many industrial and biological applications. Indeed, a fluid as vital as blood contains a mixture of serum albumin proteins with various other smaller surface-active components. Proteins and other surface active molecules are often adsorbed at an air-liquid or liquid-liquid interface due to favorable thermodynamics, and these interfaces play a role in such diverse fields as stabilizing foams and emulsions, controlling high speed coatings, the blood clotting process, designing synthetic replacements of biological fluids, etc. It is thus important to understand the interfacial behavior of protein-surfactant mixtures, especially the role it can play in bulk measurements of material properties. A complete description of the dynamics of these multi-component systems is still elusive.

In this thesis, a comprehensive study of the rheology of a model globular protein solution is described. In conventional bulk rheological studies of globular protein solutions a yield-like behavior and shear thinning in the viscosity at low shear rates is observed, even for concentrations as low as 0.03% by weight. Typical explanations for this yield stress involve the introduction of long range colloidal forces that are stronger than electrostatic forces, and which stabilize a colloidal structure formed by the protein molecules. However, evidence for this structure from small angle X-ray scattering and small angle neutron scattering is lacking. In the first part of this thesis, it will be shown using interfacial steady and oscillatory shear experiments how the yield-like behavior observed in bulk rheology in fact arises out of a purely interfacial effect. We show that the yield-like behavior and shear-thinning observed in bulk rheology can be modeled by treating the interfacial layer of the adsorbed protein as a pure plastic material that yields at a critical strain. This model also accounts for the geometric dependence seen in bulk rheology experiments.

The second part of this thesis investigates the rheological consequences of adding low molecular weight surfactants to globular protein solutions. Because non-ionic surfactants compete for the interface with the protein molecules, the resulting dynamics at the fluid interface can be complex. In addition to steady and oscillatory interfacial shear rheology, a new phenomenon called interfacial creep ringing—a term used to denote the periodic oscillations arising from the coupling between instrument

inertia and interface elasticity—arises. It is demonstrated how these damped inertio-elastic oscillations can be used to rapidly estimate interfacial viscoelastic moduli and also study the effect of the addition of non-ionic surfactants to globular protein solutions. We show that exploiting the interfacial creep ringing technique is useful as a way to rapidly determine the effects of interfacial viscoelasticity. It is also observed that increasing the concentration of the competing surfactant leads to progressively decreasing ringing frequencies and amplitudes, until visible ringing completely disappears beyond a certain concentration. Finally, we indicate future avenues of work including surface particle tracking to study these complex dynamics of protein surfactant mixtures.

Thesis Supervisor: Gareth H. McKinley
Title: Professor, Mechanical Engineering

# Acknowledgments

This thesis is dedicated to my parents. Their endless and unflinching love, care and affection has been instrumental in making this thesis possible. My mother's deep interest in everything concerning me, has gone a long way in providing me direction at every step of my life. Her confidence in me always saw me through the most trying of times.

Some of my earliest memories are filled with images of watching science documentaries with my father and then discussing them at the dinner table. His interest and curiosity often exceeded my five year old self's! I am deeply indebted to them, amongst many things, for the atmosphere of free thought and discussion they established at home, for this set the background for one of the loves of my life—science.

I would like to thank my advisor, Prof. Gareth McKinley, for his valuable guidance and for providing me with multiple opportunities to enhance my skills as a researcher. He is a repository of knowledge, and has certainly taught me much that I will not forget, about rheology as well as about the method of science.

In its encounter with Nature, science invariably elicits a sense of reverence and awe. The very act of understanding is a celebration of joining, merging, even if on a very modest scale, with the magnificence of the Cosmos. And the cumulative worldwide buildup of knowledge over time converts science into something only a little short of a transnational, transgenerational meta-mind.

—**Carl Sagan**, The Demon Haunted World: Science as a Candle in the Dark.

# Contents

# List of Figures

# Chapter 1

# Introduction

Edwin A. Abbot, in his 1884 novella about a two-dimensional world 'Flatland: A Romance of Many Dimensions' (Abbot, 1884), wrote while commenting on art in this two-dimensional world,

> If my readers have followed me with any attention up to this point, they will not be surprised to hear that life is somewhat dull in Flatland. I do not, of course, mean that there are not battles, conspiracies, tumults, factions, and all those other phenomena which are supposed to make History interesting; nor would I deny that the strange mixture of the problems of life and the problems of Mathematics, continually inducing conjecture and giving the opportunity of immediate verification, imparts to our existence a zest which you in Spaceland can hardly comprehend. I speak now from the aesthetic and artistic point of view when I say that life with us is dull; aesthetically and artistically, very dull indeed. How can it be otherwise, when all one's prospect, all one's landscapes, historical pieces, portraits, flowers, still life, are nothing but a single line, with no varieties except degrees of brightness and obscurity?

Unlike art in Abbot's two-dimensional world, the rheology of two dimensions, or interfacial rheology, is considerably more interesting and has both aesthetic as well as intellectual value. It is often necessary to investigate the properties of surfaces, as

opposed to bulk properties and interfacial rheology is an exciting field in the study of soft matter that involves the study of the dynamic response of two-dimensional surfaces to deformations.

Interfacial rheology is important in a number of fields spanning food and emulsion stability (Dickinson, 1992a), high-speed coatings, enhanced oil recovery (Krägel et al., 2008), pharmaceuticals (Patapoff and Esue, 2009) and biology (Nishimura et al., 2008). Indeed, the continuous matrix phase of a fluid as vital as blood consists of surface active serum albumin proteins and various other small surface active molecules (Peters, 1996). Morgan and Woodward (1913) attempted to use the surface tension of blood as an indicator of disease, and found that the surface tension of blood is abnormally high, especially in kidney diseases. Presumably, even more useful information could be extracted from a dynamic measure of the rheology of blood. One must exercise caution here, since measurements of the rheology of whole blood (and many other complex fluids) is beset with artifacts which can lead to misleading conclusions. These artifacts often arise from interfacial effects, and it is important to account for them correctly (Merrill, 1969). Many surface active species, like globular proteins and low molecular weight surfactants, adsorb at the interface (so as to decrease the interfacial energy) and can form interfacial mono- or multi-layers (Sanchez et al., 2002; Zasadzinski et al., 2001). These interfaces or 'skins' can have distinctly different properties compared to the bulk fluid.

The idea that interfacial effects could modify observable bulk phenomena was proposed many centuries ago. In fact, the calming of oceanic waves by an oil slick on the surface is one of the oldest scientific problems, dating back to Aristotle [Problematica Physica, 23, no. 38], Plinius Secundus (the Elder) [Historia Naturalis, vol. 2, chap. 49, 77, also chap. 106], Plutarch [Moralis: Quaestiones Naturalis, vol. 11, no. 12; also Moralis: De Prima Frigido, no. 950], and elicits considerable interest even today (Scott, 1978; Alpers and Huhnerfuss, 1989). The influence of interfacial effects is seen in something as familiar as soap bubbles and foams, shown in Figure 1.0.1a. The stability of bubbles and foams is determined chiefly by the fluid drainage properties, which strongly depends on the surface viscosity properties (Murray, 2007). These

surface properties can be modified by the addition of surfactants and proteins in the case of foods. 'Ostwald ripening'—the transport of the dispersed gas or liquid phase between bubbles (Langevin, 2000)—is also influenced by the presence of surfactants and determines the stability of drops and bubbles. Foams and bubbles and their stability also turn up in more unusual areas—the leptodactyline frogs of South America lay their eggs in a floating foam nest to avoid the larvae from coming in contact with water directly (Figure 1.0.1b). This is thought to prevent predatory attack upon the larvae (Menin and Giaretta, 2003). Something as spectacular as the nature of volcanic explosions is also determined by foam stability, and the sudden collapse of foam formed at the roof of a volcanic chamber causes sudden explosions of lava from the vent of the volcano (Jaupart and Vergniolle, 2006). An exploding bubble is shown in Figure 1.0.1c. The presence of bubbles in the lava also determines its viscosity by behaving as rigid inclusions as it is flowing downhill (Dingwell, 1998), and understanding their stability and collapse can potentially have important consequences for those living downhill. Yet another interesting physical phenomenon is the formation of the so called 'liquid marbles' (Aussillous and Quere, 2001; Stocco et al., 2011), shown in Figure 1.0.1d, which are formed when highly hydrophobic particles coat the surface of a liquid drop.

The concept of a surface viscosity or interfacial viscosity appears to have first been proposed by Plateau (1869) while observing the difference in the damping of a needle on a gas-liquid surface with an adsorbed surfactant compared to the damping in the bulk. Boussinesq (1913a,b) extended this idea of a surface viscosity or interfacial viscosity when studying the boundary condition on a falling liquid drop through a bulk fluid to explain a discrepancy in theory and experiment (Edwards et al., 1991, pp. 5). The relatively young field at that point of time continued to be developed by various researchers and scientists in their attempts to explain hitherto unexplained interfacial phenomena, and ultimately led to the generalization of Boussineq's theory to 'material' interfaces of arbitrary curvature by Scriven (1960), which was a turning point in our understanding of interfacial rheology (Edwards et al., 1991).

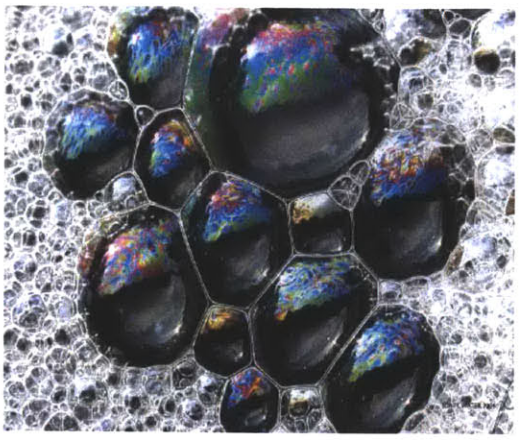

(a) The stability of bubbles and foams can be modified and controlled by the addition of surface active molecules (Murray, 2007). Image source: `http://therealisticcook.com`.

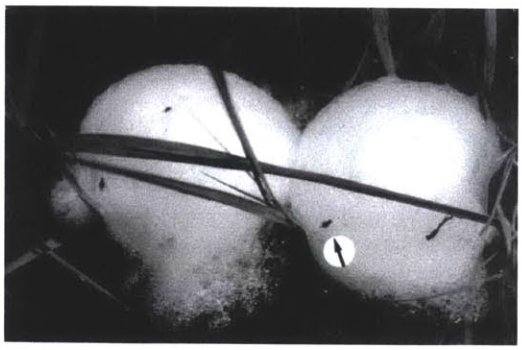

(b) Foam nests of *Physalaemus cf. fuscomaculatus*, a frog native to South America, inside which the frog's larvae are present (Menin and Giaretta, 2003).

(c) Explosion of a lava bubble at Waikupanaha, Kalapana, Hawaii, USA. Image source: `http://news.nationalgeographic.com`. Photograph by Bruce Omori/EPA/Corbis.

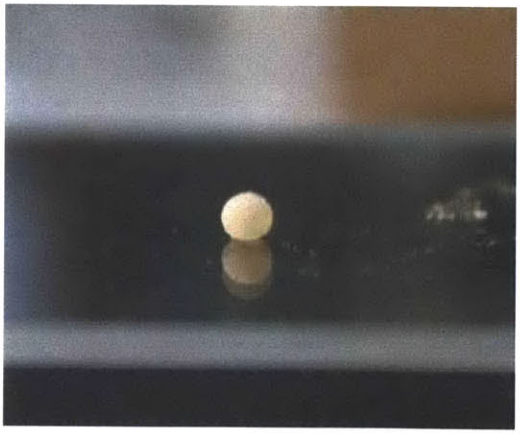

(d) Liquid marbles formed by coating fluid droplets with hydrophobic particles. Image from Aussillous and Quere (2001).

**Figure 1.0.1:** Interfacial effects present themselves in a number of physical processes and phenomena. Understanding the interfacial rheology is critical to a complete understanding of the physics.

The concept of an interfacial stress is key to understanding interfacial rheology. In bulk viscometry, a material element is sheared homogeneously and the resistance to this shearing acts upon the area of contact, which is shown in Figure 1.0.2 by the gray area. In interfacial shear rheology, the resistance to the shearing motion acts only upon a line of contact. Analogous to a bulk shear stress $\tau$, which is defined as a force per unit area (units: Pa), the surface traction or interfacial shear stress $\tau_s$ is thus defined as a force per unit length (units: Pa m). The kinematics of the deformation remains unchanged, because the shear rate $\dot{\gamma}$ is defined in the same way as in the bulk, and $\dot{\gamma} = \partial v_x/\partial y$. An interfacial shear viscosity $\eta_s$ is then defined in the usual manner and analogous to the bulk case, $\eta_s = \tau_s/\dot{\gamma}$ (units: Pa s m). Another commonly defined surface property of liquids is the surface tension $\sigma$ (units: N/m or Pa m, which is the same as that of an interfacial stress). While the surface tension $\sigma$ is a purely static measure of the forces that act at an interface, an interfacial stress gives rise to a dynamic measure of the nature of an interface undergoing deformation. If a surface is cut by an arbitrary imaginary plane, the forces arising from surface tension always act normal to the line of intersection between the surface and the imaginary plane. Interfacial stresses on the other hand are tensorial in nature and components can also act tangential to an arbitrary line drawn on the surface. In this manner a surface tension is a very different physical quantity from an interfacial stress.

The second chapter provides a background for the thesis and provides a basic introduction to rheology and viscoelasticity for unfamiliar readers. The field of interfacial rheology is introduced and different techniques to study interfacial shear rheology are presented. The materials studied and the experimental tools used in this thesis are also explained.

The third chapter presents a comprehensive study on the interfacial rheology of globular proteins (with Bovine Serum Albumin taken as the model protein) and the importance of accounting for interfacial effects while performing bulk rheology in torsional rheometers is discussed. It is also shown how the concept of the formation of colloidal crystals by globular proteins in solution is not needed to describe the


$\dot{\gamma}_{yx} = \frac{\partial v_x}{\partial y}$ $\qquad$ $\dot{\gamma}_{yx} = \frac{\partial v_x}{\partial y}$

$\tau_s$ [Pa.m] $\qquad$ $\tau$ [Pa]

$\eta_s = \frac{\tau_s}{\dot{\gamma}}$ $\qquad$ $\eta = \frac{\tau}{\dot{\gamma}}$

$\eta_s$ [Pa.s.m] $\qquad$ $\eta$ [Pa.s]

**Figure 1.0.2:** Schematic showing the nature of the deformation in interfacial and bulk shear rheology. The figure on the left depicts interfacial shear deformation, while the figure on the right depicts bulk shear deformation. Note the different units in the two cases.

unusual rheology seen in steady shear can be adequately explained by considering interfacial contributions.

The fourth chapter expands upon the work of the previous chapter and examines the interfacial rheology of protein-surfactant mixtures since most real fluids, especially biological fluids, are mixtures of globular proteins and other surface active molecules. The utility of adapting the bulk creep-ringing technique (see Section 4.2 on page 76 for a detailed description of creep ringing) for measurements of interfacial viscoelastic moduli is discussed, and the competition between a non-ionic surfactant and a globular protein for adsorption at the interface is studied using creep-ringing. Finally, the work presented in this thesis is summarized in the fifth chapter, and possible avenues for further study are outlined.

A number of recent studies have shown that interfacial effects can play an important role in a very diverse range of fields. The author earnestly hopes that this thesis is of interest to scientists who are unfamiliar with the 'Flatland' of interfacial rheology and that it aids in understanding the effective rheological response of many complex fields in which both bulk deformation and free surfaces are important.

# Chapter 2

# Experimental Techniques

A brief review of some of the techniques used for interfacial shear rheology are given in this chapter. The field of interfacial shear rheology is vast and this discussion is to merely familiarize the reader with the basic concepts of interfacial shear rheology required to understand the work herein. It is by no means intended to be exhaustive—the reader is referred to the books by Edwards et al. (1991) and Miller and Liggieri (2009) for a more extensive coverage of the field.

## 2.1 Background

### 2.1.1 Viscoelasticity

The concepts of solids and liquids are familiar to many amongst us. Intuitively, we describe a material as a solid if it undergoes a finite deformation upon the application of a finite stress, and restores its initial shape upon the removal of the applied stress.[1] Liquids, on the other hand, continuously deform upon the application of a shear stress, however small (Kundu and Cohen, 2002). Quantitatively we model ideal solids as materials that obey Hooke's law, where the shear stress in a material element $\tau$ directly proportional to the shear strain $\gamma$ ($\tau = G\gamma$), and ideal liquids as those

[1] Exceptions abound, and the shape of many solids is not restored once outside the linear regime. Beyond a certain critical stress called the yield stress, some solids can deform continuously (Kundu and Cohen, 2002).

materials that obey Newton's law of viscosity, where the shear stress in a material element $\tau$ is directly proportional to the shear strain rate $\dot{\gamma}$ ($\tau = \eta\dot{\gamma}$) (Reiner, 1960). Another useful way of thinking about the distinction between solids and liquids is in terms of the *memory* of the material (Kundu and Cohen, 2002). Solids are said to have perfect memory, since they recover their original shape upon the removal of the applied force, while Newtonian liquids have zero memory.

Many materials we encounter in daily life are ill-described by these idealizations, and the stress depends on both the strain (i.e the material exhibits elasticity) and the strain rate (i.e it exhibits viscous nature)—they posses partial memory. Such materials are hence called *viscoelastic* (Barnes et al., 1989; Reiner, 1960). There are numerous classes of constitutive equations, both linear and non-linear, that can be used to describe the behavior of these materials (Bird et al., 1987). It is useful to visualize the linear models to be combinations of springs and dashpots, with the springs representing the elastic response and the dashpots representing the viscous response of the material (Tschoegl, 1989). These two elements can be used as building blocks, and by placing them in different series and parallel configurations, a model as complicated as required to model the material can be generated, although we must keep in mind that we are restricted to linear behavior only—since both the spring and the dashpot are linear elements. Nevertheless, these models are useful because it is often possible to infer something about the microstructure of a material based on its linear viscoelastic response (Ferry, 1980), which is defined and explained in the next subsection. Also, the material parameters extracted from these linear models can conveniently be used as quality control parameters in industrial processes or material production (Barnes et al., 1989).

### 2.1.2 Bulk Rheology and Rheometry

*Rheology* is the study of the deformation and flow of matter and *rheometry* is the act of quantifying this deformation by imposing simple viscometric flows[2] on the material

[2]A viscometric flow is one in which each fluid element experiences a steady simple shearing flow (Larson, 1999).

and measuring the resulting response. Rheometric tests on Newtonian fluids—those fluids that obey the Newtonian constitutive model— give us one unique parameter, the viscosity $\eta$, which is sufficient to describe the mechanical behavior of the fluid, provided the fluid is incompressible. On the other hand, viscometric measurements on non-Newtonian fluids yield a host of different material functions which depend on shear rate, frequency, strain amplitude, etc. (Bird et al., 1987; Macosko, 1994). Most of these functions have been tabulated by Dealy (1984) and are broadly classified based on the kinematics of deformation imposed as shear or extensional functions (Barnes et al., 1989; Larson, 1999). Examples of Newtonian fluids include glycerin and water, while most polymer melts, concentrated suspensions, gels, biological fluids etc. are non-Newtonian fluids. Non-Newtonian fluids can either be shear thickening or shear thinning depending on whether the viscosity increases or decreases with shear rate, respectively. They also exhibit a range of other interesting phenomena that are not seen in Newtonian fluids, like rod-climbing, the open syphon effect, die-swell, etc. For a more detailed treatment of these and other non-Newtonian effects, the reader is referred to the book by Bird et al. (1987).

Two of the most common shear measurements are steady and oscillatory measurements. Steady shear experiments enable us to measure the steady viscosity of the fluid $\eta(\dot{\gamma})$ (units: Pa s), which is a measure of the energy dissipated per unit time (or power dissipated) in the fluid upon the imposition of a deformation. Often, the viscosity $\eta$ can be a function of shear rate $\dot{\gamma}$, and this is especially true for polymer melts and hence, more generally, $\eta = \eta(\dot{\gamma})$. As explained above, if the fluid is Newtonian, the shear stress $\tau$ in the fluid can easily be calculated from the rate-independent viscosity and the constitutive equation is simply $\tau = \eta\dot{\gamma}$. The shear viscosity of a Newtonian fluid can depend on temperature and pressure. Non-Newtonian fluids require more complicated equations of state to be used to enable the calculation of the stress from known kinematics, because the Newtonian model does not capture shear rate-dependent, time-dependent or elastic effects (Bird et al., 1987).

Most non-Newtonian fluids, for example polymer melts, exhibit 'shear-thinning'—the viscosity $\eta(\dot{\gamma})$ is a decreasing function of the shear rate $\dot{\gamma}$. This can be rationalized

by realizing that higher shear rates tend to increasingly align the flexible polymer chains in the direction of flow. This causes the chains to be less entangled, and consequently, the fluid exhibits a reduced viscosity (Larson, 1999). Although more rare, some non-Newtonian fluids can also exhibit 'shear-thickening', where as the name suggests, the viscosity $\eta(\dot{\gamma})$ is an increasing function of the shear rate $\dot{\gamma}$. Concentrated suspensions often show shear-thickening, and one common household example is 'oobleck', a concentrated suspension of corn-starch in water (Barnes et al., 1989), which derives its name from the children's book 'Bartholomew and the Oobleck' (Seuss, 1949).

Under the conditions of small deformations, much information about the nature and microstructure of the material can be extracted by modeling the material using a linear model. Two such examples are the linear viscoelastic Maxwell model (a spring and a dashpot in series) and the linear viscoelastic Voigt model[3] (a spring and a dashpot in parallel), shown in Figure 2.1.1 (Tschoegl, 1989). For the Maxwell model, the constitutive equation, or the equation that relates the stress $\tau$ to the strain $\gamma$, can be written as

$$\tau + \frac{\eta}{G}\dot{\tau} = \eta\dot{\gamma} \tag{2.1.1}$$

and likewise for the Voigt model,

$$\tau = G\gamma + \eta\dot{\gamma} \tag{2.1.2}$$

$\lambda = \eta/G$ (which has the dimensions of time) is often used as a characteristic measure of the time scale over which the viscoelastic material relaxes after the imposition of a deformation, and is termed the *relaxation time*. Imposing small amplitude oscillatory shear (SAOS) deformations is a convenient way of estimating the relaxation time and extracting the linear viscoelastic properties of different materials in the small deformation limit. The small amplitudes used minimize any change induced in the microstructure of the fluid due to the act of measurement (Larson, 1999). Let us now consider the Maxwell model, for example, and apply an oscillatory strain $\gamma(t)$ on the

[3]This is also sometimes referred to as the Kelvin model

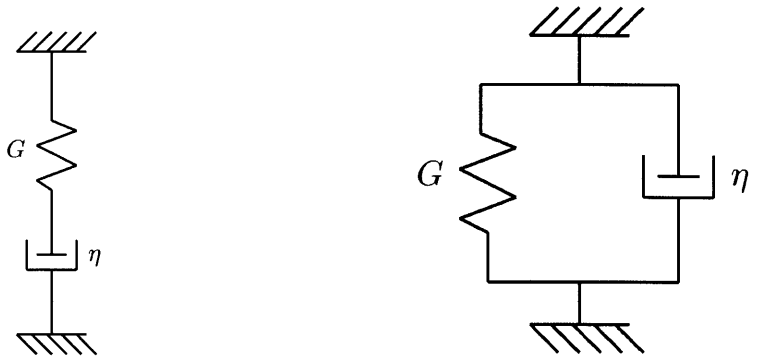


(a) (b)

**Figure 2.1.1:** Schematic diagrams of two linear viscoelastic models. (a) Linear viscoelastic Maxwell model(b) Linear viscoelastic Voigt model (Tschoegl, 1989; Macosko, 1994).

material such that $\gamma(t) = \gamma_0 \sin \omega t$, where $\gamma_0$ is the strain amplitude, $\omega$ is the frequency of oscillations and $t$ is time. This gives us a strain rate $\dot{\gamma} = \gamma_0 \omega \cos \omega t$. Substituting this into the Maxwell model and solving the resulting differential equation, we get

$$\tau = \frac{\eta \omega \gamma_0}{1 + (\lambda \omega)^2} (\cos \omega t + \lambda \omega \sin \omega t) \tag{2.1.3}$$

where $\lambda = \eta / G$ is a measure of the relaxation time of the material. It can instantly be seen that this resulting stress is the sum of an in-phase component and an out-of-phase component and hence we have $\tau = G'(\omega)\gamma(t) + (G''(\omega)/\omega)\dot{\gamma}(t)$ where

$$G'(\omega) = \frac{\eta \lambda \omega^2}{1 + (\lambda \omega)^2} \tag{2.1.4}$$

$$G''(\omega) = \frac{\eta \omega}{1 + (\lambda \omega)^2} \tag{2.1.5}$$

$G'(\omega)$ is called the viscoelastic storage or elastic modulus and $G''(\omega)$ is called the viscoelastic loss or viscous modulus. Together, they capture the viscoelastic nature of the material. Solid-like materials have $G'(\omega) > G''(\omega)$, while for liquid-like materials, $G'(\omega) < G''(\omega)$. In most real viscoelastic fluids, the material behaves liquid-like at low frequencies ($G'(\omega) < G''(\omega)$) until the $G'(\omega)$ and $G''(\omega)$ curves cross over at a certain critical frequency, beyond which the material behaves solid-like ($G'(\omega) > G''(\omega)$). For

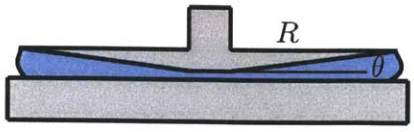


(a) Cone-and-plate fixture with radius $R$ and cone angle $\theta$.

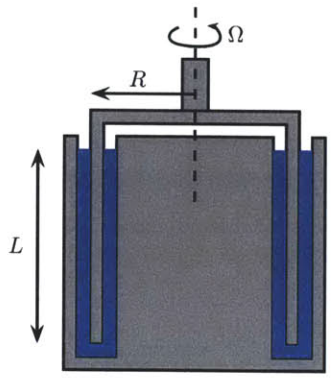


(b) Double gap Couette fixture

**Figure 2.1.2:** Examples of fixtures used to measure the torque in torsional rheometers. Not to scale.

the Maxwell model, this critical frequency is $\omega_c = 1/\lambda$ and $G'(\omega_c) = G''(\omega_c) = \eta\omega_c/2$. This crossover occurs because at high frequencies, the fluid does not have sufficient time to relax between oscillations through molecular rearrangements (Bird et al., 1987). Quite generally, it is found that the reciprocal of the cross over frequency $\omega_c$ a useful measure of the characteristic relaxation time of the material $\lambda \sim \omega_c^{-1}$ (Larson, 1999).

A rheometer measures the properties of a complex fluid as a function of shear rate $\dot{\gamma}$ or frequency $\omega$ of the imposed deformation. A known flow field is imposed on a quantity of fluid and the material properties of the fluid are then calculated based on the torque measured upon the imposition of the flow field (Bird et al., 1987). Various kinds of fixtures, or geometries[4], can be used along with torsional rheometers, each with its own advantages and disadvantages, to make these measurements. Two such fixtures, the 'cone-and-plate' (CP) geometry and the 'double gap Couette' (DG) geometry, are shown in Figure 2.1.2.

The relationship between the torque $T$ measured by the rheometer and the shear stress $\tau$ acting on the sample is determined by a purely geometric factor called the

[4]These two terms will be used interchangeably throughout this thesis

shear stress factor or simply the stress factor $F_\tau$ (units: $\mathrm{m}^{-3}$), and is given by

$$\tau = F_\tau T \tag{2.1.6}$$

The expression relating the shear rate $\dot{\gamma}$ and the angular velocity $\Omega$ is defined in a similar manner, and the shear rate factor $F_\gamma$ (dimensionless) is defined as

$$\dot{\gamma} = F_\gamma \Omega \tag{2.1.7}$$

The values of the stress factor $F_\tau$ and shear rate factor $F_\gamma$ for the cone-and-plate geometry and the double gap Couette geometry is shown in Table 2.1.2. It is emphasized that the dimensions of the stress factor $F_\tau$ change for the interfacial case, and this is discussed on page 35.

| Geometry | Stress factor $F_\tau$ ($\mathrm{m}^{-3}$) | Strain factor $F_\gamma$ |
|---|---|---|
| Cone-and-plate | $\dfrac{3}{2\pi R^3}$ | $\dfrac{1}{\tan\alpha}$ |
| Double gap Couette | $\dfrac{R_2^2 + R^2}{4\pi H R_2^2 (R_1^2 + R^2)}$ | $\dfrac{R_4^2 + R_3^2}{R_4^2 - R_3^2}$ |

**Table 2.1.1:** Table showing the stress and strain factors for the cone-and-plate and double gap Couette geometries used in this study for the bulk rheometry. The variables have been defined in the text.

Once the factors for different geometries are known, it is straightforward to calculate the viscosity. We have

$$\eta = \tau/\dot{\gamma} = F_\tau T / F_\gamma \Omega \tag{2.1.8}$$

Hence, we have for the cone-and-plate geometry (for example) that $\eta = 3T\tan\alpha/2\pi R^3\Omega$.

### Extensional Rheology

In contrast to shear rheology, in which a material element is deformed under pure shear, extensional rheology studies the material's response to extensional or elonga-

tional deformations. Extensional viscosities and relaxation times can be very different from the corresponding shear analogues. Extensional flows are important in a number of industrial applications, some of which are coatings, enhanced oil recovery, lubrication, turbulent drag reduction, and atomization (McKinley and Sridhar, 2002). Extensional rheology is usually studied on instruments such as the **Ca**pillary **B**reakup **E**xtensional **R**heometer (CaBER, (Rodd et al., 2005) or the **Fi**lament **S**tretching **E**xtensional **R**heometer (FiSER, (McKinley and Sridhar, 2002)). In the CaBER, the fluid is loaded between two plates separated by a small distance and the liquid bridge thus formed is elongated by instantaneously pulling the plates apart to a known final separation. The time evolution of the liquid bridge, which thins with time eventually leading to break-up, gives us an estimate of the relaxation time of the liquid in uniaxial extension flow. The FiSER works in a very similar manner, except that the plates are pulled apart exponentially, so as to maintain an exponentially decreasing liquid bridge diameter until the point of breakup. Extensional rheology is a broad and vast field, arguably with more challenges than shear rheology and will not be commented upon in any great detail in this thesis. The works by Petrie (Petrie, 1979, 2006) are good resources for a more detailed coverage of the field.

### 2.1.3 Interfacial Rheology

By analogy to the existence of a bulk shear viscosity and a bulk extensional viscosity, there also exists for the interfacial case an interfacial shear viscosity $\eta_s$ and an interfacial dilatational viscosity $\kappa_s$. These and other concepts pertaining to interfacial rheology are discussed in the following subsections.

#### Interfacial Shear Rheology

Interfacial shear rheology involves shearing an interface and measuring the resulting stress due to the imposed deformation. A schematic diagram of this deformation shown in Figure 1.0.2. A remarkable amount of information about the nature of the interface and its microstructure can be extracted from interfacial shear rheology and

this information is useful in understanding a multitude of technical applications, such as mass transfer, monolayers, foaming and foam stability, emulsification oil recovery or high speed coating processes (Krägel et al., 2008). The success of a particular rheometric technique depends on its ability to selectively measure stress contributions from the interface in the presence of additional stress contributions from the subphase. The relative magnitudes of these contributions are often described in terms of the Boussinesq number (Edwards et al., 1991, pp. 134):

$$Bo_s = \frac{\text{Surface drag}}{\text{Subphase drag}} = \frac{\text{Interfacial viscosity}}{\text{Bulk viscosity} \times \text{length scale}} = \frac{\eta_s}{\eta l_s} \tag{2.1.9}$$

Interfacial effects are significant only if $Bo_s \gg 1$. The Boussinesq number captures the extent of coupling between the interfacial flow and the subphase flow. The higher the Boussinesq number for a given rheometric instrument, the more sensitive is the measurement technique to interfacial stresses. It was often assumed, in the early interfacial experiments, that one could deduce the interfacial viscosity simply by the difference between the interfacial stresses measured in surface-adsorbed interfaces and those measured in 'clean' interfaces (Edwards et al., 1991). This has since been shown to be incorrect due to the hydrodynamic coupling between the interface and the subphase.

One of the earlier instruments used to measure interfacial shear rheology was the deep-channel surface viscometer, developed by Mannheimer and Schechter (1970). It consists of two concentric cylinders immersed in a liquid which is contained in a brass dish (see Figure 2.1.3). The concentric cylinders are immersed to a depth such that the bottom of the cylinders nearly touch the surface of the dish. While making measurements, the dish is rotated while holding the immersed cylinders stationary. Tracer particles (100-200 $\mu$m) are added to the surface of the liquid between the two concentric cylinders, and the centerline surface velocity of the interface between the cylinders is monitored. The interfacial viscosity can then be deduced from this centerline surface velocity. One of the drawbacks of this technique is that the tracer particles tend to migrate towards the walls of the immersed cylinders (Edwards et al.,

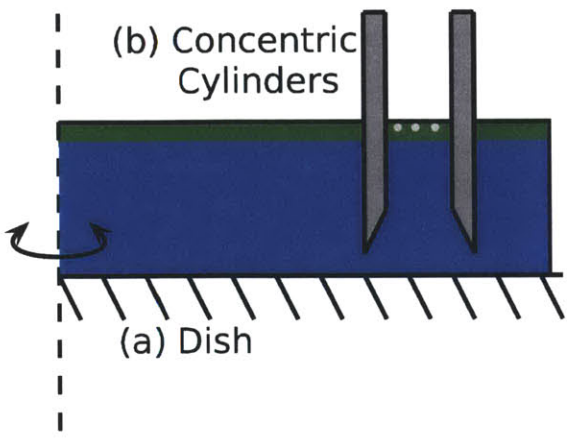


**Figure 2.1.3:** Schematic of the deep-channel surface viscometer. The gray circles represent the tracer particles.

1991).

Yet another class of interfacial viscometers utilize torque measurements to deduce the interfacial shear viscosity. One such example is the disk surface viscometer (Oh and Slattery, 1978; Goodrich, 1970). A schematic diagram of the disk surface viscometer is shown in Figure 2.1.4a. A flat circular disk is connected to a torsion wire (or in more recent instruments to the torque transducer of a stress-controlled rheometer) and is placed on the surface of a liquid-filled trough so that the disk just touches the interface. The trough is then rotated (or conversely the disk rotated in the case of the disk being attached to a stress-controlled rheometer) and the torque experienced by the disk is measured. The total torque measured by the disk is a sum of two contributions, one coming from a 'ring of contact' on the outer edge of the disk, and the other from the bulk flow established by the surface of the disk in contact with the bulk fluid. This measured torque can then be related to the viscosity using simple geometric factors. Oh and Slattery (1978) also showed how the formulations for a disk can be extended to a biconical bob placed at the interface such that the edge of the cone lies exactly at the interface, as shown in Figure 2.1.4b.

One of the limitations of the two torsional viscometers discussed above is the relatively low Boussinesq number values due to the large area of contact between the fixture and the bulk fluid. The additional torque from the bulk is unavoidable due to the coupling between the interface and the subphase, and merely serves to

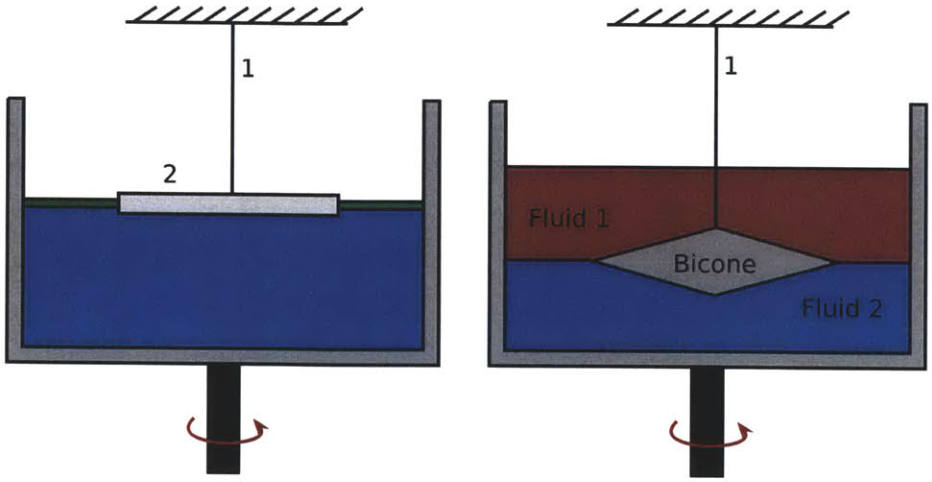


(a) Disk surface viscometer.

(b) Biconical viscometer.

**Figure 2.1.4:** Two examples of torsional surface viscometers. 1-torsion wire and 2-circular disk.

decrease the sensitivity to interfacial torque contributions. One can imagine that a fixture that simply has a circular line of contact will have increased sensitivity due to the decreased coupling with the bulk. One such viscometer is the knife-edge surface viscometer first outlined by Brown et al. (1959) shown in Figure 2.1.5. It works on the same principle as the other torsional viscometers—the measured torque is related to the interfacial viscosity through a geometric factor, although this factor, derived by Mannheimer and Schechter (1970), is significantly more complicated than those for the disk surface viscometer or the biconical surface viscometer due to the sensitivity to the specific wetting characteristics of the material of the knife-edge.

More recently, Vandebril et al. (2010) have designed a new geometry, called the double wall ring[5] which attaches onto a stress-controlled rheometer. A schematic diagram as well as a rendering of the DWR is shown in Figures 2.1.6a and 2.1.6b respectively.

The DWR is particularly sensitive to the interfacial rheology of a surface on account of its relatively higher Boussinesq number as compared to the geometries discussed above. Vandebril et al. (2010) have calculated the flow induced in the subphase

[5]The abbreviation DWR will be used often in this thesis while referring to the double wall ring geometry

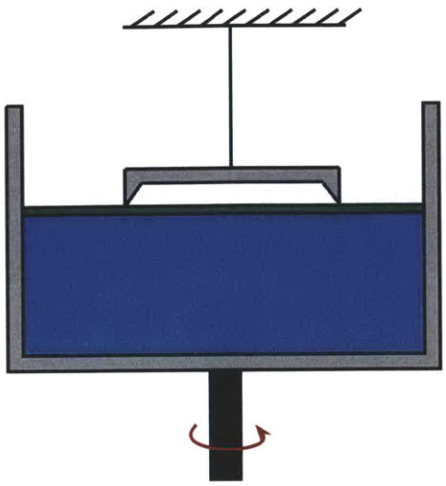

**Figure 2.1.5:** The knife-edge viscometer (Edwards et al., 1991).

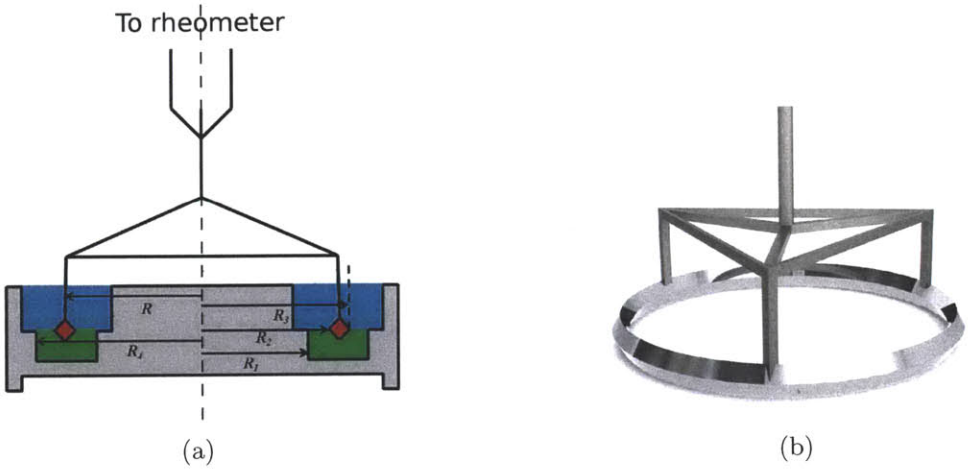


(a) (b)

**Figure 2.1.6:** The double wall ring (DWR) fixture used for the interfacial rheology measurements in this thesis. (a) The blue and green colors refer to the two different fluid phases and the ring (red-diamond) is placed so that the edge just touches the interface between the two liquids. An air-water interface configuration can also be used. (b) A 3-D rendering of the ring (Image courtesy Simon Haward).

using an iterative numerical scheme at different Boussinesq numbers. One such flow profile from their study is shown in Figure 2.1.7a. The amplitude function $a_j(r,z)$ (units: m) for the phase $j$ is defined as $a_j(r,z) = v_j/\Omega$ where $v_j$ is the velocity in the phase $j$ ($j = s$ for the interface, $j = 1$ for the bulk) and $\Omega$ is the angular velocity of the ring. The figure shows the amplitude function at the interface $a_s(r,z)$ and in the bulk $a_1(r,z)$ as a function of position $(r,z)$ under steady shear. Some amount of diffusion of the interface flow into the bulk is visible. The black diamond represents the ring. Figure 2.1.7b shows the surface amplitude function $a_s(r,z)$ for an air/water interface as a function of radius at different values of the Boussinesq number. The shear rate $\dot{\gamma} = \partial v_x/\partial y$ is a constant only if the velocity profile varies linearly with the depth $y$. Deviations from the expected linear profile are seen only for $Bo_s \leq 14.3$. For all values of $Bo_s$ higher than this, the effect of the surface-bulk coupling can be safely ignored, which is true for all measurements performed in this study (see Figure 3.6.3, pp. 69). The Boussinesq number is commented upon in more detail later in this and the following chapters.

The double wall ring has been used extensively in the experiments described in the following chapters of this thesis so a detailed explanation of the DWR is warranted at this juncture. The double wall ring used in this study—the same as that used by Vandebril et al. (2010)—is made out of a platinum-iridium alloy. This enables easy and thorough cleaning of the ring between experiments through the burning off of any residue with a hand-held blow torch. The dimensions of the ring are (Figure 2.1.6a), trough inner radius $R_1 = 31$ mm, ring inner radius $R_2 = 34.5$ mm, ring outer radius $R_3 = 35.5$ mm, trough outer radius $R_4 = 39.5$ mm, and the thickness of the ring is $a = 1$ mm (AR-G2 Interfacial Accessories Manual, TA Instruments). The ring has a diamond cross-section which enables it to support a flat interface between the two fluid phases. The sharp edge of the diamond pins the meniscus and eliminates any curvature associated with it.

The DWR is especially sensitive to interfacial stresses acting on the ring at the pinned line of contact, and this can be better understood based on the Boussinesq number. The DWR aims to maximize the length of contact between the geometry

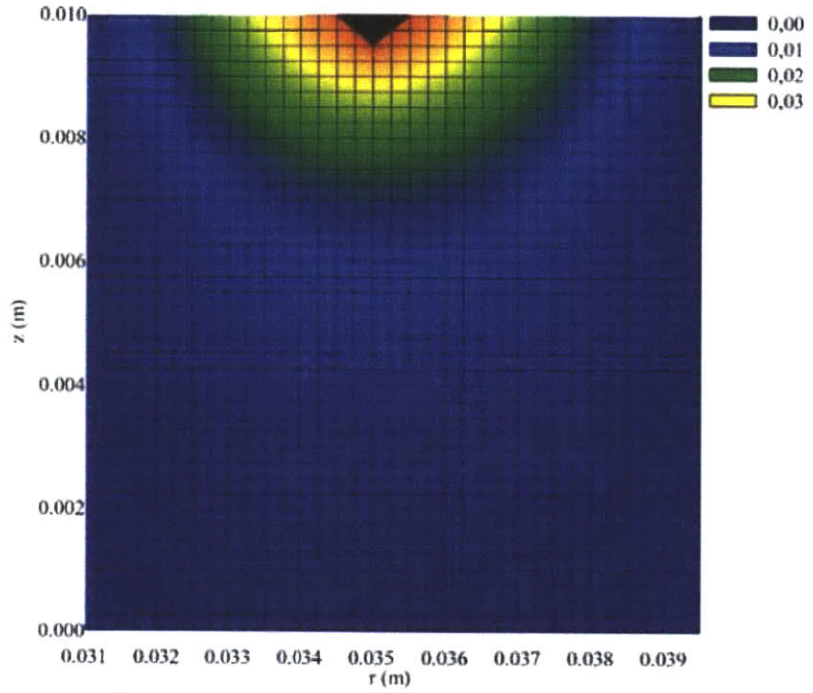


(a)

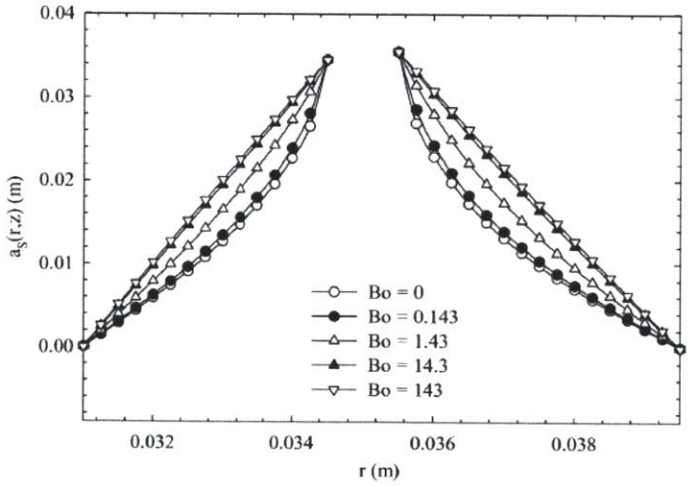


(b)

**Figure 2.1.7:** The flow field for the DWR geometry reproduced from Vandebril et al. (2010). (a) The surface amplitude function $a_s(r, z)$ and the bulk amplitude function $a_1(r, z)$ as a function of position $(r, z)$ in steady shear. The surface is an air-water interface with $\eta_s = 10^{-5}$ Pa s m. The angular velocity is 1 rad $s^{-1}$. (b) Amplitude function corresponding to a steady shear flow, $a_s(r, z = 0)$ for an air/water interface as a function of the position $r$ in the inner and outer gap for different $Bo$ numbers in rotational mode. Surface viscosities $\eta_s$ range from 0 ($Bo = 0$) to $10^4$ Pa s m ($Bo = 143$) (Vandebril et al., 2010).

| Geometry | Length scale (mm) |
|---|---|
| Double wall ring | $l_s = A_B/P_s = 0.7$ |
| Cone-and-plate (40 mm dia.) | $l_s = \pi R^2/2\pi R = 10$ |
| Double gap Couette | $l_s = 2\pi RH/2\pi R = 59.5$ |
| Bicone (68 mm dia.) | $l_s = 2\pi R^2/2\pi R = 34$ |
| Disk Viscometer (40 mm dia.) | $l_s = \pi R^2/2\pi R = 10$ |

**Table 2.1.2:** Table showing the length scale of the DWR in comparison to some of the common geometries used with the rheometer. The relatively small length scale of the ring makes it a better candidate than the other geometries for interfacial measurements.

and the interface for a given area of contact. The rationale for this can be seen upon a closer inspection of the Boussinesq number $Bo_s$ given in Equation (2.1.9), which can be written as

$$Bo_s = \frac{(\eta_s V/L_s)P_s}{(\eta V/L_B)A_B} = \frac{\eta_s}{\eta l_s} \tag{2.1.10}$$

where $\eta_s$ is the interfacial viscosity (units: Pa m), $V = R\Omega$ is a characteristic velocity (units: m/s), $L_s$ and $L_B$ are the characteristic length scales for shear flow in the interface and bulk subphase respectively, $P_s$ is the contact perimeter between the interface and the geometry, (units: m) and $A_B$ is the contact area between the geometry and the subphase. For interfacial effects to be dominant, we require $Bo_s \gg 1$, and hence for any given test fluid, which has fixed values of interfacial and bulk viscosities, we will need to minimize $l_s$. For the DWR, the length scale $l_s$ in Equation (2.1.9) equals $l_s^{DWR} = 0.7$ mm. Table 2.1.2 lists the values of the length scale for a number of typical geometries, including the interfacial bicone and double wall ring fixtures. The superiority of the DWR for interfacial measurements compared to the other geometries is immediately evident from these values of $l_s$.

For the DWR, the values of the stress factor $F_\tau$ and the strain factor $F_\gamma$ are given by (AR-G2 Operator's Manual, TA Instruments)

$$F_\tau = \frac{1}{2\pi(R_2^2 + R_3^2)} \tag{2.1.11}$$

and

$$F_\gamma = \frac{R_4^2}{(R_4^2 - R_3^2)} + \frac{R_1^2}{(R_2^2 - R_1^2)} \tag{2.1.12}$$

respectively, where $R_1$ is the inner radius of the trough channel, $R_2$ is the inner radius of the ring, $R_3$ is the outer radius of the ring, and $R_4$ is the outer radius of the trough channel. The specific values of $F_\tau$ and $F_\gamma$ for the DWR are $F_\tau = 64.94$ m$^{-2}$ and $F_\gamma = 9.3927$. The shear stress and the shear rate is then calculated using $\tau_s = F_\tau T$ and $\dot{\gamma} = F_\gamma \Omega$ as discussed previously in section 2.1.2.

The rheometer has a certain minimum *resolvable* torque, which is determined by the sensitivity of the transducer used to measure the torque. The minimum torque that is *measurable*, however, depends on the noise floor of the instrument. By Equation (2.1.6), the minimum stress that is measurable is directly proportional to the minimum measurable torque. Also, since $\eta_{\min} = \tau_{\min}/\dot{\gamma}$, the minimum measurable viscosity is a line of slope -1 on a log-log plot. This implies that our ability to measure low shear viscosities at low shear rates is compromised. For the DWR set up used in this thesis, $\eta_{s,\min} \approx 5 \times 10^{-6}$ Pa s m. For a more detailed discussion of minimum measurable and resolvable torques, see the discussion on page 90.

For even lower values of interfacial viscosity, a magnetic needle rheometer (Reynaert et al., 2008), or 2D microrheology can be used. Whereas the magnetic needle rheometer uses a rod of several hundred microns in length (Brooks et al., 1999), 2D microrheology relies on video-tracking of the thermal motion (2D Brownian motion) of passive tracer particles that are only a few microns in diameter. The magnetic rod rheometer requires a range of rod sizes to achieve the dynamic range easily achieved using the DWR ring. Two-dimensional microrheology works best for viscous and weakly viscoelastic interfaces in which the mean square displacement (MSD) of the particles is linear in time, and the diffusion coefficient can then be related to the viscosity of the medium using the Stokes-Einstein equation (Ortega et al., 2010) because the flow is a viscously dominated low Reynolds number flow. For heterogeneous interfaces, more accurate results require two-particle tracking (Chen et al., 2003; Prasad et al., 2006),and for complex interfaces, where the mean square displacement has a

sub-linear dependence on time, a generalized version of the Stokes-Einstein (GSE) equation must be used (Ortega et al., 2010; Levine and Lubensky, 2000). In such cases the interpretation of the mean square displacement data requires use of hydrodynamic models and additional assumptions (as summarized by Ortega et al., 2010) and connections with bulk measurements are relatively difficult to make. For the stiff viscoelastic interfaces described in this thesis, the use of the DWR geometry provides an easy and accurate measurement technique over a wide dynamic range that is not easily achieved with 2D microrheology.

## 2.2 Materials

Serum albumins were identified as important constituents of blood as early as 1839 (Ancell, 1839). The word albumin comes from the Latin *albus*, meaning white, the color of most protein precipitates upon denaturation (Carter and Ho, 1994). Albumin was at the forefront of protein research during World War II, when a substitute for blood plasma was very sought after on the battlefield. Bovine serum albumin (BSA) was tried as a substitute on account of its ease of availability as a by-product of the cattle industry. However it was quickly realized that humans were incompatible with BSA, causing serum sickness in many subjects, and techniques to manufacture human serum albumin (HSA) were developed (Peters, 1996).

BSA has a molecular weight of $66,700 \pm 400$ Da and is a 'heart-shaped' molecule in the pH range 4.5-8.0 (Carter and Ho, 1994). However it is usually modeled hydrodynamically as being a prolate ellipsoid with a major axis of 140 Å and a minor axis of 40 Å (Squire et al., 1968; Wright and Thompson, 1975). Figures 2.2.1a and 2.2.1b show a stereo view of the HSA molecules (adopted from He and Carter (1992)) and a schematic diagram of the hydrodynamic representation of BSA and respectively. HSA has 80% homology with BSA and is also a heart-shaped molecule (Carter and Ho, 1994).

Bovine Serum Albumin, extracted by agarose gel electrophoresis, was obtained from Sigma-Aldrich Corp, St. Louis, MO USA, in the form of a lypophilized powder.

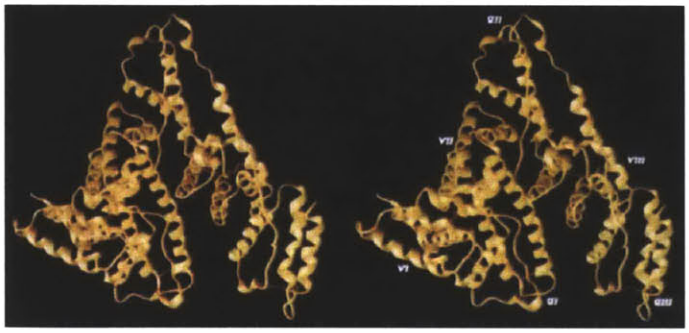

(a) The 'Heart-shaped' HSA molecule between pH 4.5-8.0—HSA can 80% homology with BSA (Carter and Ho, 1994). Image reproduced from He and Carter (1992).

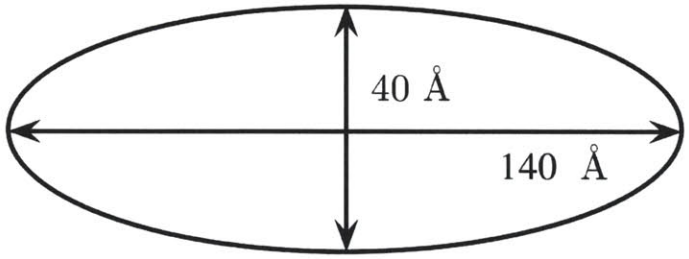


(b) Hydrodynamic representation of BSA. Major axis = 140Å, Minor axis = 40Å

**Figure 2.2.1:** The stereo view of the HSA molecule shown in (a) has been reproduced from He and Carter (1992). (b) shows a schematic diagram of the hydrodynamic representation of BSA.

0.01 M Phosphate Buffered Saline (PBS) Solution (NaCl - 0.138 M; KCl - 0.0027 M; pH 7.4, at 25°C.), was prepared by dissolving dry PBS powder obtained from Sigma-Aldrich Corp. A weighed quantity of BSA was dissolved in the PBS and the solution was brought up to the required volume in a volumetric flask to finally obtain solutions with a BSA concentration of 50 mg/ml. The prepared solutions were stored under refrigeration at 4°C and were allowed to warm up to room temperature before being used for experiments. All BSA solutions used in this study had a concentration of 50 mg/ml, unless otherwise specified.

We chose a non-ionic surfactant because additional complications can arise due to complex formation between BSA and ionic surfactant molecules. If there is a favorable interaction between the protein and surfactant, the protein can adopt a very different conformational state as compared to the native protein (Miller and Liggieri, 2009; Mobius and Miller, 1998; Goddard and Ananthapadmanabhan, 1993). The surfactant used in this study was Polysorbate 80 (Tween 80$^{TM}$, P1754, Sigma-Aldrich Corp.), the structure of which is shown in Figure 2.2.2. To prepare the protein-surfactant mixtures, a known amount of polysorbate 80 was weighed and dissolved in PBS. This was then dissolved into a weighed amount of BSA solution to achieve the required concentration. To increase accuracy, solutions with $c_{surf} \leq 10^{-2}$ wt% were prepared by successive dilution.

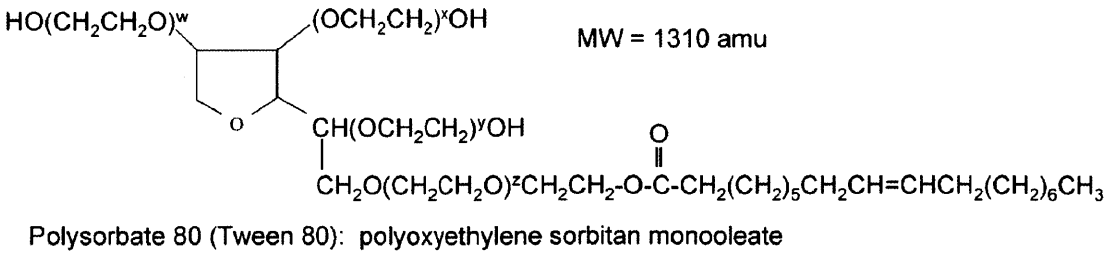


**Figure 2.2.2:** The molecular structure of Polysorbate 80, adopted from Kerwin (2008).

The Newtonian calibration oil used for the peak hold tests described in the next Chapter was the Cannon Instruments N1000 calibration oil, with a viscosity $\eta = 2.008$ Pa s at 25°C.

## 2.3 Methods

### 2.3.1 Bulk Shear Rheometry

Torsional rheometry was used to measure the bulk viscosity $\eta(\dot{\gamma})$ using the equations defined in Equations (2.1.6) and (2.1.7). This involves steady shearing of a fluid in a rheometer and measuring the torque $T$ required to maintain this shearing motion at a given shear rate $\dot{\gamma}$. Measurement of the required torque at steady state enables us to find the steady shear viscosity $\eta$ using

$$\eta = \frac{\tau}{\dot{\gamma}} = \frac{F_\tau T}{F_\gamma \Omega} \tag{2.3.1}$$

One can also measure the viscoelastic storage modulus $G'(\omega)$ and viscoelastic loss modulus $G''(\omega)$ using a rheometer, by applying a sinusoidally varying strain. If the imposed strain field is $\gamma(t) = \gamma_0 \sin(\omega t)$, then $G'(\omega)$ and $G''(\omega)$ can be calculated from the in phase and out of phase components of the measured shear stress using the expression

$$\tau = \gamma_0[G'(\omega)\sin(\omega t) + G''(\omega)\cos(\omega t)] \tag{2.3.2}$$

Two bulk geometries—a 40 mm diameter, 2° cone and a double gap Couette fixture (rotor inner radius $R_1 = 20.38$ mm, rotor outer radius $R_2 = 21.96$ mm, rotor height $H = 59.5$ mm, cup inner radius $R = 20$ mm)—were attached to the TA instruments ARG2 stress controlled torsional rheometer. Figure 2.1.2 shows schematic diagrams of these geometries, while the stress factor $F_\tau$ and strain factor $F_\gamma$ for these geometries is given in Table 2.1.1.

Various kinds of bulk measurements were performed in this work, including steady shear rate sweeps, small amplitude oscillatory shear (SAOS) frequency sweeps and small amplitude oscillatory shear (SAOS) strain amplitude sweeps. These experiments are discussed in more detail in the following chapters.

### 2.3.2 Interfacial Shear Rheology

The interfacial double wall ring (Vandebril et al., 2010), introduced in section 2.1.3 [pp. 28], was used to perform the interfacial rheology measurements, on account of its superior selective sensitivity to interfacial torque contributions and compatibility with the ARG2 stress-controlled rheometer (see Table 2.1.2, pp. 35). A variety of steady-shear as well as oscillatory experiments were performed to probe and extract information about the interfacial viscoelastic layer.

Steady shear rate sweep experiments were employed to measure the interfacial steady shear viscosity $\eta_s(\dot{\gamma})$ as a function of the shear rate $\dot{\gamma}$. Peak-hold experiments—tests in which the shear rate is held constant and the viscosity is measured as a function of time—enabled us to study short time transient responses as well the irreversible nature of the adsorption of protein at the interface. Analogous to the bulk measurements, interfacial SAOS frequency and strain amplitude sweeps were performed to study the viscoelastic nature of the protein layer adsorbed at the interface.

For the steady shear case, the interfacial steady shear viscosity (units: Pa s m) can be calculated from the measured torque $T$ and the stress and shear rate factors defined in Equations (2.1.11) and (2.1.12) and we have

$$\eta_s = \frac{\tau_s}{\dot{\gamma}} = \frac{F_\tau T}{F_\gamma \Omega} = \frac{\dfrac{1}{2\pi(R_2^2+R_3^2)}T}{\left(\dfrac{R_4^2}{(R_4^2-R_3^2)}+\dfrac{R_1^2}{(R_2^2-R_1^2)}\right)\Omega} \tag{2.3.3}$$

Interfacial viscoelastic storage and loss moduli $G'(\omega)$ and $G''(\omega)$ (units: Pa m) can also be measured using the DWR geometry using Equation (2.3.2). These experiments are discussed in detail in Chapters 3 and 4.

### 2.3.3 Viscometer-Rheometer-on-a-Chip (VROC)

To measure the shear rheology of the BSA solutions in the absence of a fluid-air interface, a microfluidic slit rheometer referred to as VROC (Viscometer-Rheometer-on-Chip, Rheosense Inc, CA) was employed. This enables the measurement of the

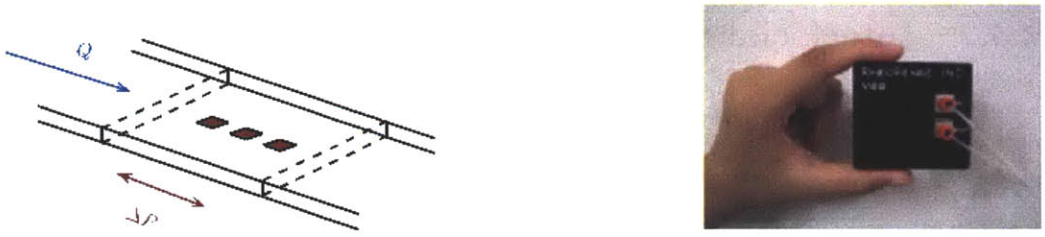


(a) (b)

**Figure 2.3.1:** The Viscometer-Rheometer-on-a-chip (VROC), Rheosense Inc., San Ramon, CA

steady shear viscosity of the solutions at high shear rates, and is shown in Figure 2.3.1. The specific microfluidic device used in this study, the mVROC Type A05 chipset, consists of a rectangular cross-section channel ($w$ = 3.02 mm; $d$ = 50 $\mu$m) made out of Pyrex mounted on a gold-coated silicon base containing three flush mounted pressure sensors (Pipe et al., 2008).

The pressure drop $\Delta P$ required to drive the flow with rate $Q$ is related to the wall shear stress $\tau_w$ by the expression $wd\Delta P = 2L(w+d)\tau_w$ whereas the nominal wall shear rate $\dot{\gamma}_w$ associated with fully developed laminar flow of a Newtonian fluid is $\dot{\gamma}_w = 6Q/wd^2$. The fluid is injected into the microfluidic channel using 2.5 ml Hamilton Gastight glass syringes (Reno, NV, USA) and the flow rate $Q$ is varied using a Harvard Apparatus syringe pump. The VROC device outputs the pressure drop as a function of flow rate $\Delta P(Q)$ and the data can then be used to determine the nominal or apparent viscosity using the equation

$$\eta(\dot{\gamma}_w) = \tau_w/\dot{\gamma}_w \tag{2.3.4}$$

For a non-Newtonian, shear thinning fluid, the velocity profile in the channel will not be parabolic and the plot of $\Delta P$ *vs.* $Q$ is nonlinear. In this case, the true wall shear rate $\dot{\gamma}_{w,true}$ can be computed using the Weissenberg-Rabinowitsch-Mooney (WRM) equation (Pipe et al., 2008; Macosko, 1994):

$$\dot{\gamma}_{w,true} = \frac{\dot{\gamma}_a}{3}\left[2 + \frac{d(\ln \dot{\gamma}_a)}{d(\ln \tau_w)}\right] \tag{2.3.5}$$

where $\dot{\gamma}_a = 6Q/wd^2$ is the apparent wall shear rate calculated assuming a parabolic flow profile and $\tau_w$ is the wall shear stress. For a given channel, the range of wall shear rates $\dot{\gamma}_w$ accessible is determined by the viscosity and shear thinning behavior of the fluid and the range of shear stresses, $\tau_w$, is set by the choice of pressure sensors. The maximum pressure $P_{\max}$ attainable in the mVROC Type A05 chip used in the measurements conducted during this study at MIT is $P_{\max} = 10$ kPa. Since the measurable pressure range is nominally 1-100% of $P_{\max}$, the minimum shear rate is $\dot{\gamma}_{w,\min} \approx 300$ s$^{-1}$ for a viscosity of $\eta = 1$ mPa s. A parallel set of measurements were performed at Rheosense Inc, using an mVROC Type A02 ($d = 20$ $\mu$m, as opposed to $d = 50$ $\mu$m for mVROC Type A05; same pressure range), this extended the measurable shear rate range to lower shear rates of $\dot{\gamma}_{w,\min} \approx 100$ s$^{-1}$ for a viscosity of $\eta = 1$ mPa s. The measurement envelope (i.e) the accessible range of shear rates and viscosities for the A02 and A05 chips are shown in Figure 2.3.2, which is calculated using

$$\eta_{\max} = \frac{wd\Delta P_{\max}}{2L(w+d)\dot{\gamma}_w} \tag{2.3.6}$$

$$\eta_{\min} = \frac{wd\Delta P_{\min}}{2L(w+d)\dot{\gamma}_w} \tag{2.3.7}$$

The temperature of the fluid in the syringe as well as in the VROC channel and all interconnects was maintained at 25°C using thermal jackets with a liquid circulation system.

Using the background on interfacial rheology, techniques employed and materials used presented in this and the previous chapter, we are now ready to explore the interfacial rheology of globular proteins and protein surfactant mixtures, and this is discussed in detail in Chapters 3 and 4.

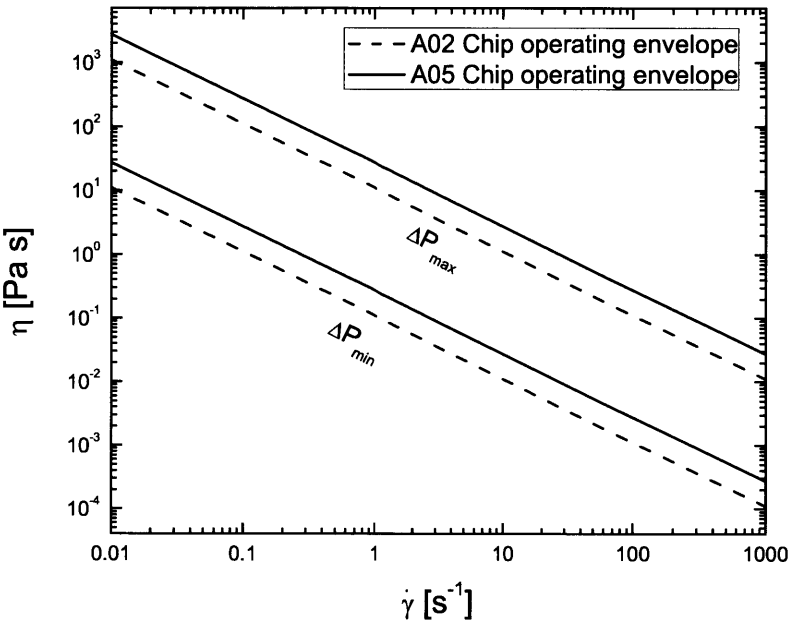


**Figure 2.3.2:** The measurement envelopes for the two microfluidic chips, mVROC A02 and A05 (100 Pa $\leq \Delta P \leq$ 10 kPa) used in this study. The A02 chip enables us to make measurements at lower shear rates even thought the pressure range is identical to that of the A05 chip because of the smaller value of $d$.

# Chapter 3

# Surfactant-Free Interfacial Rheology of Protein Solutions

## 3.1 Introduction

Serum albumins are the most abundant among the constituent proteins in mammalian blood (Peters, 1996). Serum albumins participate in various biological functions, including maintaining blood pH and osmotic pressure (Carter and Ho, 1994), as well as transporting ligands, metabolites, lipophilic compounds, hormones and drugs, including anesthetics and anti-coagulants (Peters, 1996; Carter and Ho, 1994). Since albumins transport all kinds of cargo, Peters refers to them as the "tramp steamers" of blood circulation (Peters, 1996). The concentration of human serum albumin (HSA) in blood plasma is $\sim$ 40 mg/ml ($\sim$ 0.6 mM), (Peters, 1996). Bovine serum albumin (BSA) is quite similar to human serum albumin (HSA) (80% homology), pointed out by Peters (1996). Interestingly, when BSA solutions are tested on a torsional rheometer, the solutions exhibit a yield-like behavior for a relatively wide range of concentrations, spanning from 0.03 wt% to 10 wt% (Matsumoto and Inoue, 1993; Inoue and Matsumoto, 1994; Ikeda and Nishinari, 2000), with the apparent viscosity dropping by several orders of magnitude as the imposed shear rate is raised from 0.01 to 100 $s^{-1}$. Similar responses have been observed for other globular proteins (Matsumoto and Inoue, 1996; Inoue and Matsumoto, 1996; Ikeda and Nishinari, 2001a).

It is argued that the presence of a yield stress is a consequence of strong long-range repulsive forces that are present even at concentrations as low as 0.03 wt% (or 3 $mg/ml^{-1}$), and the concentration of added salts is reported to have little or no effect on the observed response (Ikeda and Nishinari, 2000). Several recent studies invoke this apparent yield stress of solutions of bovine serum albumin and other proteins in the context of applications ranging from electrospinning (Regev et al., 2010) to synovial lubrication (Oates et al., 2006), and in the discussion of glassy behavior exhibited by BSA solutions at high concentration (Brownsey et al., 2003). Since the interactions of these proteins affect osmotic properties, functioning and flow of blood and also play a critical role in various physiological processes, clinical medicine and pharmacology (Peters, 1996), the origin of this solid-like response, especially at relatively low concentrations of the globular protein solutes, needs to be examined and evaluated carefully and rigorously.

In this study, we characterize the bulk rheological behavior of BSA solutions by imposing steady shearing deformations on a stress-controlled rotational rheometer using both cone-and-plate (CP) and double-gap (DG) Couette geometries. Since many proteins are known to adsorb preferentially at the solution-air interface that is ubiquitous in these geometries, we also use microfluidic rheometry to study the response of protein solutions in a device where no solution-air interface is present. Interestingly, we measure an apparent yield-like response for BSA solutions with the two torsional fixtures, but not in the microfluidic chip, implying that interfacial rheological effects may be important. It is well known that measurements of material properties such as surface tension on a static fluid interface do not provide a quantitative understanding of the dynamical response of the interface (Adamson and Gast, 1997; Edwards et al., 1991; Miller and Liggieri, 2009). Therefore, we also probed the rate-dependent interfacial viscosity and strain-dependent interfacial viscoelasticity of the BSA solutions using a novel double wall ring (DWR) geometry (Vandebril et al., 2010) This detailed study of interfacial rheology is necessary to distinguish the contribution from globular proteins in solution from that of proteins adsorbed at the interface.

In general, the viscoelasticity of a protein or colloidal solution is a manifestation of

both the increased resistance to flow that originates from the friction experienced by the dispersed moieties, and from the strength of interactions that must be overcome to cause any deformation from an undisturbed state. The interparticle interactions and microstructure deduced from the response to an imposed stress must also influence the hydrodynamic and thermodynamic properties measured in diffusion, osmotic pressure and scattering experiments (Russel et al., 1989; Larson, 1999) therefore we also compare and contrast the range of interaction potentials obtained with different techniques (see section 3.5). Finally, we derive a simple but quantitative model to show how typical bulk viscosity measurements made on a torsional rheometer in the presence of a free surface can be systematically interpreted in terms of a rate-independent bulk contribution (measured with microfluidic rheometry at high shear rates) and a non-linear, rate-dependent interfacial contribution. We hope that our measurements, theoretical insights and discussion will provide the context and methodology for deconvolving the complex rheological behavior of other biofluids where such interfacial effects play a role.

The characterization and understanding of interfacial rheological properties of proteins, surfactants, macromolecules and particles are important for many applications including food (van Vliet et al., 2002; Dickinson, 1999; Murray, 2002), foam and emulsion stability (Murray, 2007), medicine and biology (Miller and Liggieri, 2009; Zasadzinski et al., 2001; Proctor et al., 2005), oil recovery, high speed coating (Edwards et al., 1991; Krägel et al., 2008), etc. Many researchers have studied and described the orientational and conformational changes of proteins in interfacial environments and these changes markedly influence the viscoelastic nature of the interface (Song and Damodaran, 1987; Wang et al., 2003; Freer et al., 2004a,b). Typical biofluids encountered in nature and in industry are multicomponent mixtures, and the structure and the rheology of the complex mixed interface depend upon the concentrations and interactions of the different surface-active components (Miller and Liggieri, 2009; Zasadzinski et al., 2001; Krägel et al., 2008; Murray, 2010; Langevin and Monroy, 2010). In this study, we focus specifically on the rheology of surfactant-free protein solutions to understand, in a quantitative way, why dilute solutions of globular pro-

teins (such as bovine serum albumin solutions) display a yield-like behavior in bulk viscosity measurements on a torsional rheometer. Similar apparent solid-like behavior has been observed in bulk rheology measurements on physiological fluids in biomedical applications, for example, whole saliva (Waterman et al., 1988; Park et al., 2007), pharmaceuticals like monoclonal antibody solutions[1] (He et al., 2010; Liu et al., 2005; Patapoff and Esue, 2009) and, most commonly, in the food and consumer product industries (e.g. acacia gum solutions as discussed by Sanchez et al. (2002)), among others. The non-Newtonian bulk rheological response as measured with a cone-and-plate geometry was attributed to the formation of an interfacial viscoelastic film by Waterman et al. (1988) for saliva solutions and similar qualitative arguments are put forward by Sanchez et al. (2002) for acacia gum solutions. By making distinct independent measurements of the interfacial viscosity and the interface-free bulk response of the protein solutions, in the present work we are able to isolate and quantify the effect of the interfacial viscoelastic film. Using a simple additive model, we show how the presence of a viscoelastic solid-like film will systematically corrupt the measured bulk viscosity on conventional torsional rheometers for most biofluids and solutions containing surface-active groups. Further, we show how the effective contribution of the interfacial film to the apparent measured viscosity changes with the choice of geometry on a torsional rheometer, and we provide an analytical method for estimating both the interfacial viscosity and true zero shear viscosity from bulk viscosity measurements.

## 3.2 Bulk Rheology and High Shear Rheometry

In stress sweep experiments, the steady shear viscosity $\eta(\dot{\gamma})$ of bovine serum albumin (BSA) solutions, measured using the double-gap (DG) geometry on the controlled-stress rheometer, exhibits a highly shear thinning response, as seen in Figure 3.2.1. The data exhibit characteristics of a yield stress fluid because $\eta(\dot{\gamma}) \sim \tau_y/\dot{\gamma} \sim \dot{\gamma}^{-1}$ (Larson, 1999). We also repeated the measurements using a cone-and-plate (CP)

[1] See the discussion in section 3.5

geometry as previous workers (Matsumoto and Inoue, 1993; Inoue and Matsumoto, 1994; Ikeda and Nishinari, 2000; Regev et al., 2010) have reported yield stress in BSA solutions primarily the from CP device and obtained similar results (Matsumoto and Inoue, 1993; Inoue and Matsumoto, 1994; Ikeda and Nishinari, 2000; Matsumoto and Inoue, 1996; Inoue and Matsumoto, 1996; Ikeda and Nishinari, 2001a,b). We find that the viscosity measured with the DG is consistently lower than the CP measurements at all shear rates, as shown by the inset in Figure 3.2.1a. Further, the relative viscosity of all the samples is nearly the same in the low shear rate regime, indicating that the characteristic concentration dependence expected for colloidal dispersions (discussed later) is not observed here (Russel et al., 1989; Larson, 1999). We hypothesize that the high values of this nearly concentration-independent shear viscosity measured at low deformation rates must be related to the formation of an interfacial layer of adsorbed protein at the sample interface. The rheometric data suggest that the measured values of bulk viscosity obtained with either geometry have substantial contributions from a surface-adsorbed protein layer, and the relative contributions of interfacial effects depend upon the geometry. But to verify this hypothesis, we need to characterize the response of BSA solutions in a geometry that does not have any solution-gas interface.

For this purpose, we used the microfluidic capillary viscometer, VROC. The corresponding measurements indicate a Newtonian-like response, as shown in Figure 3.2.1a, with the rate-independent viscosity values increasing steadily with concentration $c$ of the BSA in solution. The VROC data agree quite well with the high shear rate viscosity measured in the DG, and both approach a rate-independent value $\eta_\infty(c)$. The viscosity values measured in the VROC and the DG are consistently lower than the viscosity measured in the CP geometry, especially at the lower shear rates where $\dot{\gamma} \ll 10^3$. The difference between the cone-and-plate and VROC measurements is even clearer when a different (more sensitive) microfluidic chip is used (these experiments were conducted at Rheosense Inc, San Ramon, CA using mVROC chip Type A02), which allows us to measure viscosity at lower shear rates than those possible with the chip Type A05 (used in MIT), as shown in Figure 3.2.1b. The viscosities measured

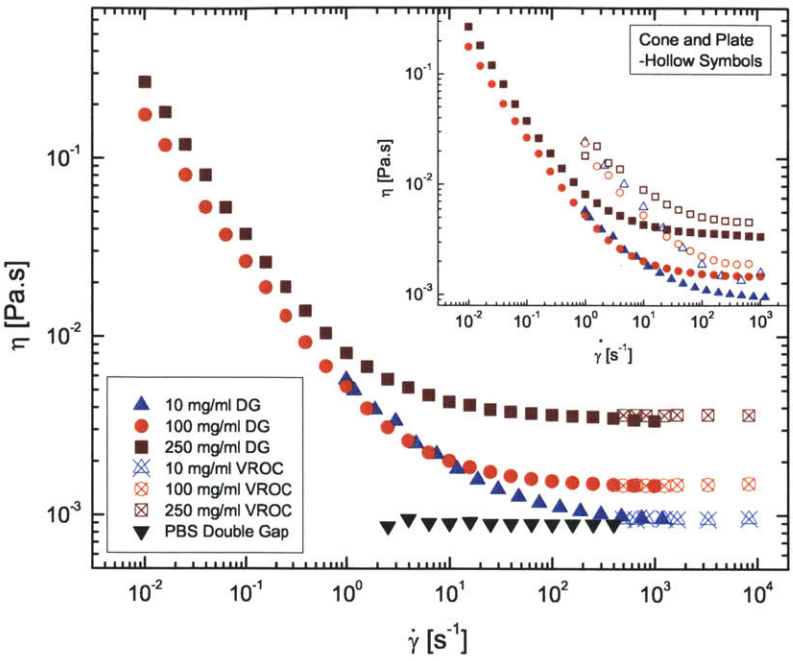


(a) Double gap Couette and mVROC measurements.

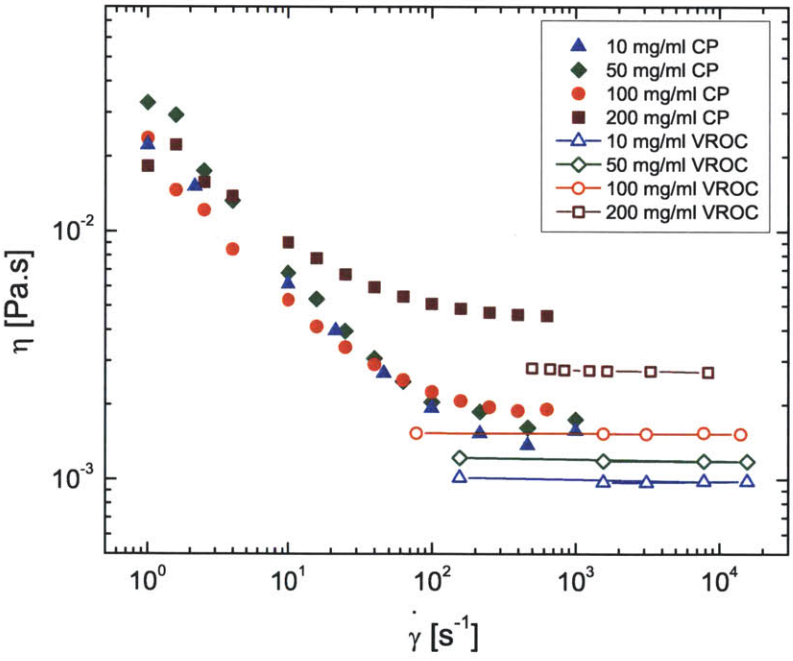


(b) Cone-and-plate and mVROC measurements.

**Figure 3.2.1:** Bulk steady shear viscosity of BSA solutions. (a) Comparison of the shear viscosity of BSA solutions measured using the double gap geometry on a stress controlled rheometer (ARG2) (filled symbols), and a microfluidic rheometer (mVROC Type 05) (checked). The inset shows the bulk viscosity measured on ARG2 using the double gap Couette (DG) geometry as contrasted with the 40 mm cone-and-plate geometry (CP) (hollow symbols). (b) Comparison of shear viscosity of BSA solutions measured using the cone-and-plate fixture on a stress controlled rheometer (ARG2) (filled symbols), and a microfluidic rheometer (mVROC Type 02) (hollow symbols).

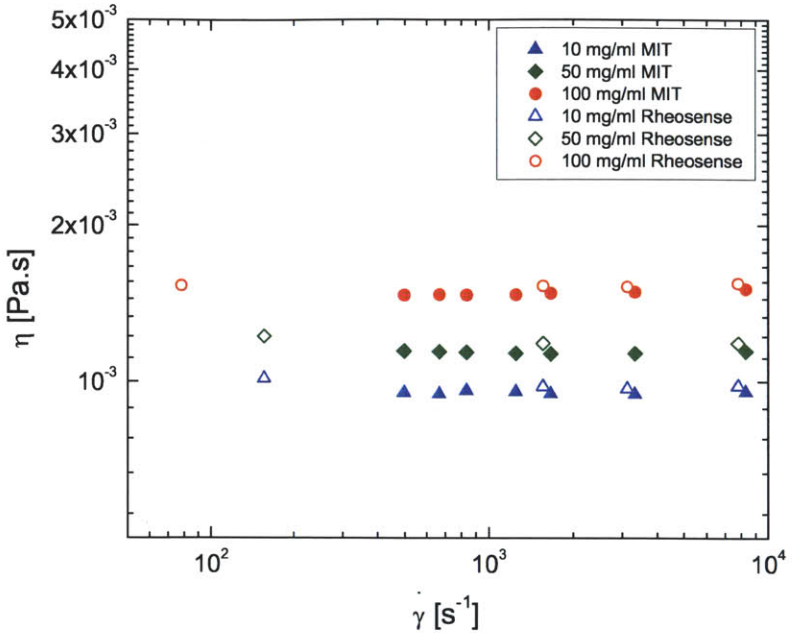


**Figure 3.2.2:** Comparison of the bulk viscosity measured as a function of shear rate as measured by separate VROC devices in two laboratories—the non-Newtonian Fluids research group at MIT, and Rheosense Inc., San Ramon, CA.

with different chips agrees quite well, as shown in Figure 3.2.2, which confirms the fact that there is no shear-thinning. The range of shear rates that can be probed could also be extended with these parallel measurements. Measurements using different geometries on a torsional rheometer show a geometry-dependent response, though, as shown in the inset of Figure 3.2.1a. Figure 3.2.3a and 3.2.3b also show the flow profiles in the VROC instrument. As expected for a Newtonian fluid, the gradient in pressure along the channel is a constant for a given flow rate (Figure 3.2.3a). Furthermore, the pressure drop across the channel is proportional to the flow rate and increases with increasing viscosity (Figure 3.2.3b). Both these point to the fact that the liquid is Newtonian for our purposes and that any viscoelastic effects are absent.

It is clear that the protein-rich interface provides a much higher contribution to the overall response of BSA solutions measured in rotational rheometers than the homogeneous solution examined in the interface-free flow generated in the microfluidic chip rheometer. The formation of a protein-rich interface and its deformation-rate-dependent viscosity and viscoelastic behavior are described in the next section.

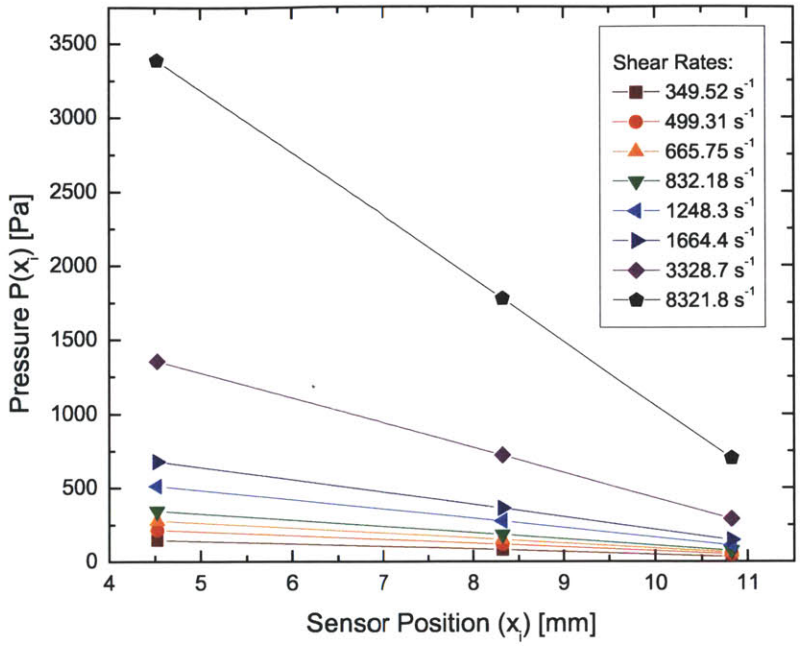


(a) Pressure as a function of sensor location along the channel at different shear rates.

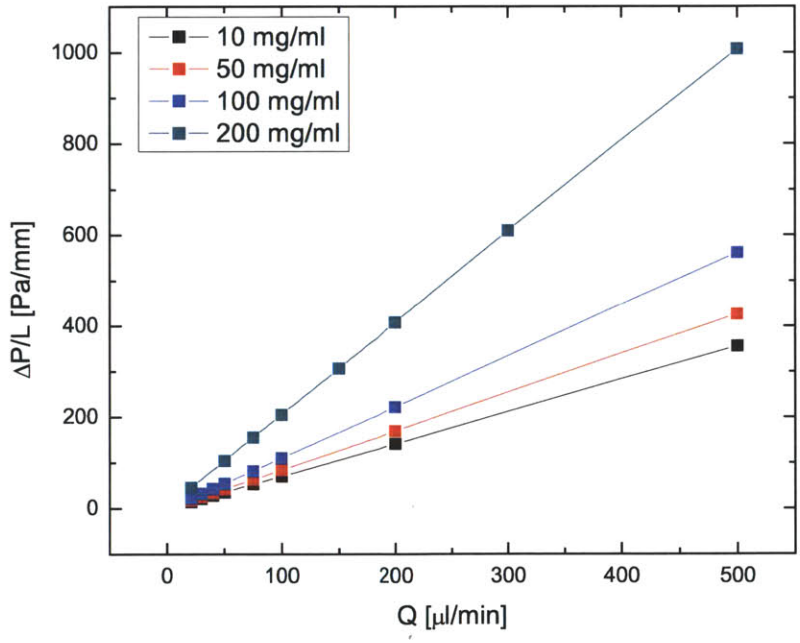


(b) Pressure drop as a function of flow rate for different concentrations of BSA solutions.

**Figure 3.2.3:** The linear profiles indicate that the fluid is indeed Newtonian, and the WRM correction (Equation (2.3.5)) is not required in this case.

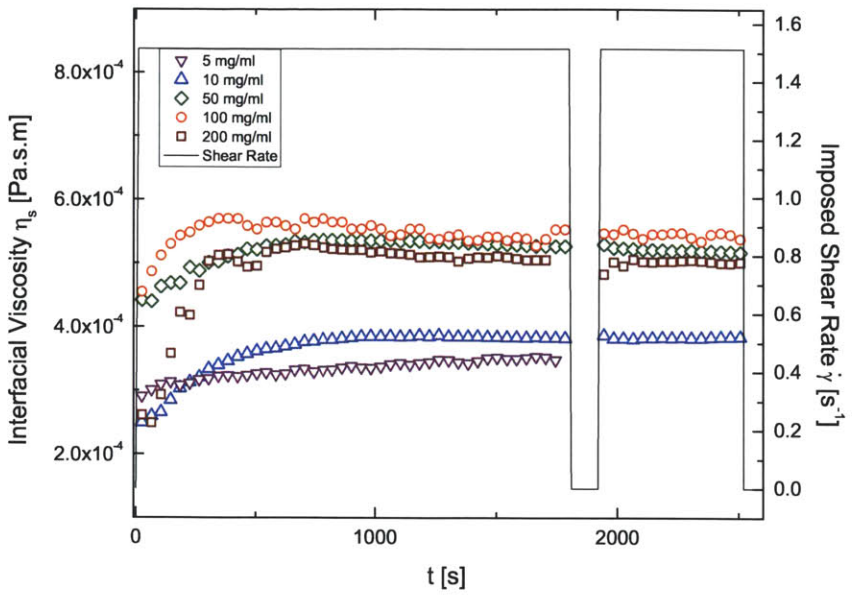


**Figure 3.3.1:** Peak hold test characterizing the evolution of the interfacial viscosity for BSA samples tested using the DWR geometry, at a shear rate of 1.5 $s^{-1}$ for 1800 s; after holding the sample at rest for 120 s, the viscosity measurement is repeated at the same shear rate.

## 3.3 Peak Hold Test and Adsorption at the Interface

After a fresh solution of BSA is placed in the DWR geometry, we can examine the change in the interfacial viscosity by using a 'peak hold' test as shown in Figure 3.3.1. The resistive torque exerted on the DWR fixture is measured as a function of time at a constant shear rate of $\dot{\gamma} = 1.5\ s^{-1}$. The resulting interfacial viscosity $\eta_s$ increases steadily with time, and reaches a nearly constant value after 300 s. While the experimental protocol associated with filling the trough does not allow us to start the experiment immediately after the interface is created, the relative values of the rise in interfacial viscosity and the plateau viscosity are qualitative measures of adsorption rate and concentration of adsorbed protein, and the measured time scales are in good agreement with the literature values (Dhar et al., 2010).

The driving force for adsorption of BSA at the surface can be understood by considering the thermodynamics of liquid interfaces (Adamson and Gast, 1997). The excess surface Gibbs free energy at an interface $G_I$ (units: J $m^{-2}$), can be related

to the solute concentration by Gibbs equation, $G_I = \sigma + \sum_i \mu_i \Gamma_i$, where $\mu_i$ is the chemical potential. The superficial density $\Gamma_i$ is the two-dimensional concentration of surfactants in the interfacial region. Thus it follows from the Gibbs equation that if the surface tension of a liquid is lowered by the addition of a solute, the solute will be preferentially adsorbed at the interface. Like surfactants, BSA adsorbs at liquid/air interface; the kinetics of adsorption, and the stability of the adsorbed film have been studied by a host of different techniques, including neutron reflectivity and spectroscopy (Lu et al., 1999), ellipsometry and radiolabel technique (Graham and Phillips, 1979), fluorescence, surface tensiometry, microrheology (Dhar et al., 2010), surface pressure, as well as interfacial shear and dilational rheology (Dickinson, 1999; Cascão Pereira et al., 2003; Graham and Phillips, 1980). It is well known that a saturated monolayer coverage develops as a result of nearly irreversible adsorption (Graham and Phillips, 1979; Svitova et al., 2003) and the kinetics of adsorption is diffusive only for low concentration of BSA (implying that the adsorbed amount increases with $t^{0.5}$) (Graham and Phillips, 1979). For the relatively high bulk concentrations used in our experiments, a surface coverage of $\Gamma_i = 2 - 3$ mg m$^{-2}$ of BSA is reported in the literature (Lu et al., 1999; Graham and Phillips, 1979), and this value of $\Gamma_i$ is close to the maximum fractional coverage $\Gamma_{\max}$ expected for a configuration when ellipsoidal globular proteins lie sideways or with their long axis parallel to the interface (Lu et al., 1999; Graham and Phillips, 1979). Hence the interfacial viscosities measured in peak-hold experiments with the DWR geometry approach nearly identical, concentration-independent plateau values as shown in Figure 3.3.1. The irreversible nature of the adsorption is demonstrated by the essentially unchanged value of the interfacial viscosity measured in each case when the shearing deformation is restarted after cessation for two minutes. While it is clear that protein adsorption leads to a significant interfacial viscosity contribution, the shear rate dependence of this adsorbed layer also needs to be studied, and is described in the next section.

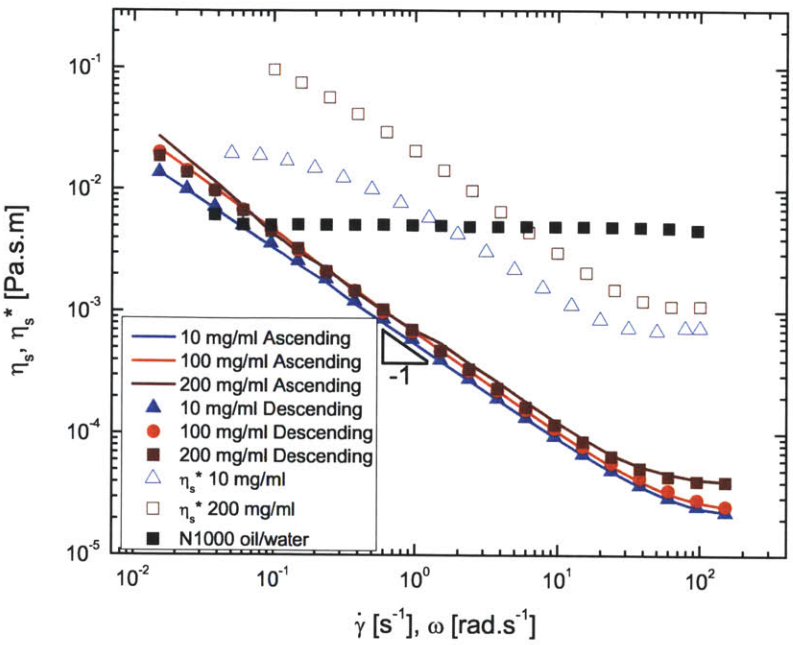


**Figure 3.4.1:** Interfacial viscosity of BSA solutions measured using ascending (symbols) and descending (lines) shear rate sweeps using the DWR geometry. The complex interfacial viscosity data (hollow symbols) measured in oscillatory shear with DWR show that the empirical Cox-Merz rule is not followed. A shear rate independent, Newtonian response is shown by a thin layer of calibration oil (N1000) on DI water (black squares).

## 3.4 Interfacial Viscosity and Viscoelasticity

The resistive torque exerted by the interface does not increase linearly with increasing rotational rate of the DWR, leading to a marked shear-thinning behavior in the measured value of interfacial viscosity as shown in Figure 3.4.1. The data exhibit characteristics of a yield stress fluid as $\eta_s(\dot{\gamma}) \sim \tau_s/\dot{\gamma} \sim \dot{\gamma}^{-1}$ This is strongly reminiscent of the bulk shear-thinning behavior reported in Figure 3.2.1. In addition, there is no hysteresis seen in the measurement of $\eta_s$—values measured in ascending and descending shear-rate sweeps coincide in every case.

We estimate the diffusion timescale $t_D$ for BSA to diffuse a distance equal to its size $a_{\text{eff}}$ to be $t_D \approx a_{\text{eff}}^2/D \approx 0.2$ ms where $a_{\text{eff}} \approx 3.5$ nm, and $D$ is determined using the Stokes-Einstein equation $D = kT/6\pi\eta_0 a_{\text{eff}}$, where $kT$ is the thermal energy and $\eta_0$ is the solvent viscosity. The estimated value agrees with the measured value (Gaigalas et al., 1992) and tells us that once the layer is established, in the absence of any other gradients, the superficial concentration of the macromolecules does not change

due to diffusive transfer (Graham and Phillips, 1979). Additionally this explains why no hysteresis is observed in Figure 3.4.1, as the interfacial layer reforms almost instantaneously after the cessation of steady shear. To confirm whether this shear-thinning response is indeed from a non-Newtonian interfacial viscosity, we carried out calibration checks by mimicking the method of Vandebril et al. (2010). Measurement with a film of viscous calibration oil with thickness $\delta = 5.8$ mm formed over DI water is shown by black squares in Figure 3.4.1. The measured Newtonian-like interfacial viscosity $\eta_s = 0.59 \times 10^{-2}$ Pa s m is greater the simple estimate obtained by $\eta\delta = 0.14 \times 10^{-2}$ Pa s m, since additional dissipation occurs in both oil and water phases.

To demonstrate the viscoelastic character of the interface, we compare the interfacial shear viscosity $\eta_s$ (filled symbols in Figure 3.4.1) from steady shear experiments with the corresponding values of interfacial complex viscosity $\eta_s^*$ from small amplitude oscillatory shear measurements (hollow symbols). We find that the empirical Cox-Merz rule (Larson, 1999) stating $|\eta_s^*(\omega)| \cong |\eta_s(\dot{\gamma})|_{\dot{\gamma}=\omega}$ is not obeyed. The lower values of $\eta_s(\dot{\gamma})$ imply that the interfacial microstructure of the adsorbed BSA film is disrupted by the larger shear deformations imposed during steady shear measurements. The strain-dependent values of interfacial storage and loss modulus measured in strain sweep experiments performed at a constant imposed frequency of $\omega = 1$ rad $s^{-1}$ for various concentrations can be used to construct a viscoelastic master curve for this BSA interface as shown in Figure 3.4.2. Here $a(c)$ and $b(c)$ are the shift factors required to overlay moduli data on the reference values measured at $c = 50$ mg $ml^{-1}$. For small strains and for the chosen frequency, the storage modulus is greater than the loss modulus, or $G_s'(\omega = 1 \text{ rad s}^{-1}) > G_s''(\omega = 1 \text{ rad s}^{-1})$, implying that the interface is rigid or solid-like. Increasing the concentration of BSA in solution is accompanied by increases in both the moduli. The measured interfacial elasticity falls rapidly beyond a yield strain of $\gamma_Y \approx 0.01$ and therefore the nominal interfacial tension required to break the interfacial structure, or cause yielding of interfacial layer, is of the order of $\tau_{sY} = G_s'\gamma_Y \approx 2.3 \times 10^{-4}$ Pa m. It is worth noting that this value is close to the interfacial tension measured in steady shear and $\tau_{sY} = \eta_s\dot{\gamma} \approx 10^{-4}$ Pa m at the lowest imposed shear rates ($\dot{\gamma} = 10^{-2}$ $s^{-1}$) presented in Figure 3.4.1.

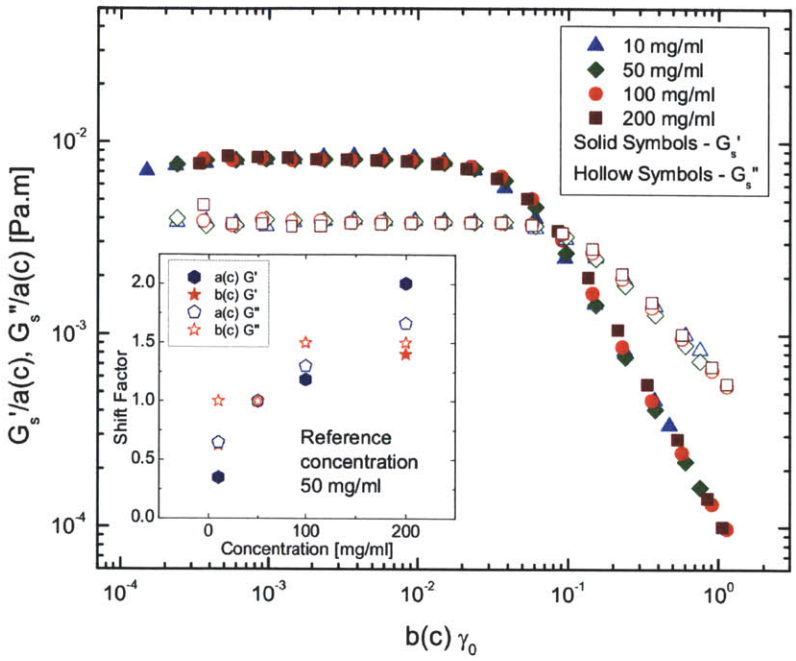


**Figure 3.4.2:** Master-curve showing the reduced interfacial storage and loss modulus of BSA solutions measured as a function of reduced oscillatory strain amplitude at a fixed frequency using the DWR fixture on the ARG2. Shift factors construct the master curve as shown in the inset. All curves are overlaid on 50 mg $ml^{-1}$ data.

The viscoelastic characteristics of the interface are further demonstrated by the frequency sweep measurements shown in Figure 3.4.3. The elastic and viscous contributions to the interfacial shear modulus are shown by filled and hollow symbols respectively. At low frequencies, the interface response is dominated by viscous effects and $G_s''(\omega) > G_s'(\omega)$. The crossover frequency $\omega^*$ decreases, and the corresponding moduli values increase with increasing concentration. The oscillatory shear measurements show that the interfacial microstructure becomes more gel-like with an increase in the bulk concentration of the protein. It is well known (Freer et al., 2004a; Lu et al., 1999) that the adsorption-induced conformation changes and subsequent protein aggregation at the liquid/air interface produce a viscoelastic film at the interface. The size and microstructure of protein aggregates as well as the presence of a secondary layer underneath the primary interfacial layer are reported to depend upon the concentration of protein in the bulk (Lu et al., 1999). The lower crossover frequency observed at higher bulk concentrations corresponds to a longer relaxation time, im-

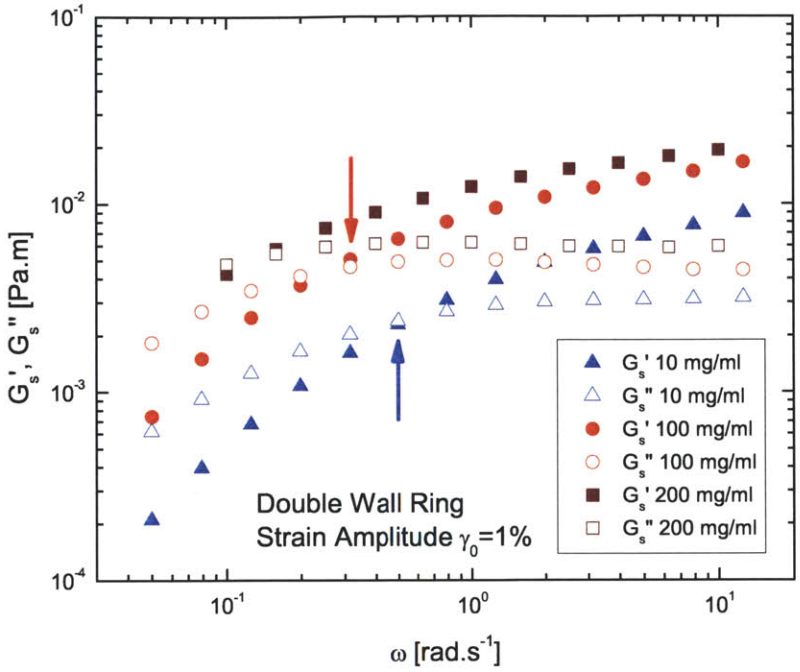


**Figure 3.4.3:** Interfacial storage and loss modulus of BSA solutions measured as a function of oscillatory frequency for different values of BSA concentration (using DWR fixture). The arrows show the crossover frequency for the 10 mg ml$^{-1}$ and 100 mg ml$^{-1}$ concentrations respectively.

plying that the interface has larger aggregates or more compactly packed protein in this case. The measurements at higher frequencies, i.e. for $\omega > 10$ rad s$^{-1}$, show significant inertial effects, where the raw phase angle approaches 180 degrees. The raw phase angle for the data shown in Figure 3.4.3 is always less than 90 degrees, implying inertial contributions are properly accounted for. The importance of the inertial contribution can be evaluated using an appropriate Reynolds number $\mathrm{Re} = \rho\omega d^2/h$, defined for the present geometry, where $d = 1$ mm is the characteristic dimension of the fluid geometry. For the BSA solutions, we find $Re > 1$ for $\omega > 1$ rad s$^{-1}$. The inertial contributions to the measured torque become prominent at high frequencies as was demonstrated and discussed by Reynaert et al. (2008) for the magnetic rod rheometer and by Vandebril et al. (2010) for the DWR geometry.

## 3.5 Intrinsic viscosity, charged suspensions and interaction potentials

The zero shear rate viscosity for colloidal suspensions is known to increase with concentration as described by the Krieger-Dougherty equation:

$$\frac{\eta(\phi)}{\eta_0} = \left(1 - \frac{\phi}{\phi_m}\right)^{[\eta]_s \phi_m} \tag{3.5.1}$$

where $\phi_m$ is the maximum packing fraction,$[\eta]_s = \lim_{c\to 0}(\eta - \eta_0)/\phi\eta_0$ is the intrinsic viscosity, $\phi$ is the volume fraction of the colloidal particles and $\eta_0$ is the solvent viscosity. As the particle aspect ratio is increased, the intrinsic viscosity increases, and $\phi_m$ decreases, but the product of these two is usually in the range of $1.4 < [\eta]_s\phi_m < 3$ (Larson, 1999) The intrinsic viscosity of suspensions $[\eta]_s$ as formulated in Equation (3.5.1) is dimensionless, as it is defined in terms of volume fraction, and for an ideal dilute suspension of spherical particles, $[\eta]_s = 2.5$. If we examine the bulk viscosity data shown in Figure 3.2.1, it is clear that the asymptotic plateau in the viscosity expected at low shear rates is not observed—the measured viscosity values at low deformation rates are significantly higher than anticipated for a protein of the size and shape of BSA, and this has led to the extensive discussion in the literature regarding the formation of colloidal crystals by relatively small concentrations of globular proteins (Matsumoto and Inoue, 1993; Inoue and Matsumoto, 1994; Ikeda and Nishinari, 2000; Matsumoto and Inoue, 1996; Inoue and Matsumoto, 1996; Ikeda and Nishinari, 2001a,b; Regev et al., 2010; Oates et al., 2006; Brownsey et al., 2003). The concentration dependence observed in the high shear rate viscosity ($\eta_\infty$) measurements performed in the microfluidic capillary rheometer follow the trend anticipated by the Krieger-Dougherty equation for a spherically shaped dispersed phase up to a concentration of 100 mg $ml^{-1}$, as shown in Figure 3.5.1.

In protein and polymer solution rheology, the intrinsic viscosity is defined in terms of concentration $c$(mg $ml^{-1}$) and is computed using $[\eta_P] = \lim_{c\to 0}(\eta - \eta_0)/c\eta_0$. The intrinsic viscosity computed from the data in Figure 3.5.1 is $[\eta]_P \approx 0.004$ ml $mg^{-1}$ and

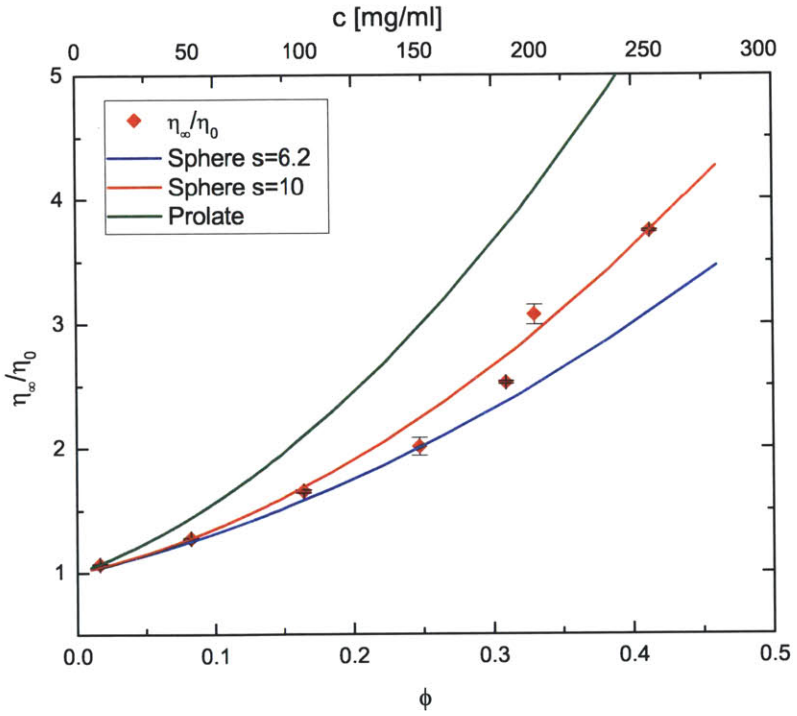


**Figure 3.5.1:** Concentration dependence of the high shear rate viscosity of BSA (red symbols; measured in VROC) is fit by charged colloid theory, (Equation (3.5.2), red line). Also shown are the bounds for uncharged prolate hard ellipsoids (green) and hard spheres (Equation (3.5.1), blue line).

this agrees well with the typical reported value of $[\eta]_P = 4.1 \pm 0.3$ ml g$^{-1}$ (Tanford and Buzzell, 1956; Lefebvre, 1982; Richards, 1993; McMillan, 1974; Harding, 1997). Note that the intrinsic viscosity now has units of reciprocal concentration (ml g$^{-1}$). BSA is a globular protein with a molecular weight of 66 kDa and at neutral pH, fatty-acid-free BSA exists as a heart-shaped molecule, though the dispersed protein is conventionally modeled as an ellipsoid (Peters, 1996; Ferrer et al., 2001). While anisotropy in shape affects both the dynamics and the self-assembly of colloidal particles (Larson, 1999; Sharma et al., 2009), the reported aspect ratio of BSA is $L/d = 3.5$, and is thus rather small to expect the formation of a liquid crystalline phase in the bulk or at the interface. In any case, we see that the fit of Equation (3.5.1) for a prolate ellipsoid with $L/d = 3.5$ (green line in Figure (3.5.1)), estimated using Simhas formula Richards (1993)), over-predicts the viscosity.

If we use the diffusive time scales estimated earlier on the basis of solvent viscosity to be $t_D \approx 0.2$ ms, then even for an applied shear rate of $\dot{\gamma} = 10^4$ s$^{-1}$, the Peclet number (ratio of the diffusive time-scale to the flow time-scale) is of the order of $Pe = \dot{\gamma} t_D \approx 0.002$. The Peclet number provides the measure of the perturbative effects due to the flow compared to the restoring effect of Brownian motion (Russel et al., 1989) and low values of Pe imply that non-equilibrium effects often seen for colloidal suspensions with larger particles ($> 1$ $\mu$m) are not present even in the microfluidic measurements. In other words, the concentration-dependent viscosity values $\eta_\infty(c)$ measured on the VROC are in fact representative of the true zero shear viscosity for these protein solutions, and therefore we are justified in using these values in Figure 3.5.1. We note, however, that for the protein concentrations studied here, the measurements in the microfluidic rheometer or VROC are shear-rate independent (or display Newtonian behavior), and therefore the extrapolation to lower shear rates will give the same viscosity value as measured, say, at a shear rate of 1000 s$^{-1}$. In the case of bulk viscosity measured by the cone-and-plate (CP) or the double-gap (DG) geometry, a similar extrapolation is not advisable and an inspection of Figure 3.2.1b shows that the CP extrapolation will always give higher viscosity values than obtained by extrapolating DG data. For example, in studies on monoclonal antibody solutions

(He et al., 2010; Liu et al., 2005; Patapoff and Esue, 2009), where an apparent yield-like response is observed in bulk viscosity measurements, He et al. (2010) choose to extrapolate the shear thinning viscosity data (measured at high shear rates) in order to estimate zero-shear viscosity, without incorporating the yield-like response that is evident at low shear rates (see Fig. S1 in the supplementary information of He et al. (2010)). It is possible that this yield-like response also arises due to interfacial effects of the kind documented in this thesis and this deviation could also be studied using the methodology described in this thesis. The interfacial viscoelasticity—as well as the apparent bulk viscosity reported from torsional rheometers—will also be affected by the presence of surfactants and other surface-active groups, and in the particular case of monoclonal antibody solution, the interfacial viscoelastic effects are commonly suppressed by the addition of a non-ionic surfactant (Patapoff and Esue, 2009), which is dealt with in more detail in the succeeding chapter.

The classic data by Tanford and Buzzell (1956) that include measurements up to 40 mg $ml^{-1}$ using capillary viscometers for BSA solutions are often discussed as a textbook example of the concentration dependence of viscosity expected for charged colloids (Russel et al., 1989; Larson, 1999). The presence of surface charge increases the effective particle diameter, and concomitantly increases the viscosity observed at any volume fraction $\phi$ (Russel et al., 1989; Larson, 1999). The analysis by Russel et al. (1989) allows us to relate the viscosity of a suspension to the volume fraction using the equation

$$\frac{\eta(\phi)}{\eta_0} = 1 + 2.5\phi + \left[2.5 + \frac{3}{40}\left(\frac{d_{\text{eff}}}{a}\right)^5\right]\phi^2 + O(\phi^3) = 1 + 2.5\phi + s\phi^2 + O(\phi^3) \quad (3.5.2)$$

The magnitude of $s$ (the coefficient of quadratic term), which is determined by the value of $d_{\text{eff}}$, is dictated by the hydrodynamic contributions and interaction potential relevant to the specific dispersion being considered and a higher charge implies larger $d_{\text{eff}}$ and larger $s$, for example (Russel et al., 1989; Larson, 1999). In general, the value of $s$ depends upon specific interactions and the model used, and for a system where only hard sphere repulsion applies ($d_{\text{eff}} = 2a$), Batchelor showed that $s =$

6.2. In Russel's formulation for the charged sphere case, the value of $s$ is related to electrostatics, and usually $d_{\text{eff}} > 2a$. The concentration dependence of viscosity of BSA solution can be described by using Equation (3.5.2). The best fit value, $s = 10$, corresponds to an interaction potential of $O(kT)$ as calculated theoretically for BSA solutions (Wajnryb and Dahler, 1999) using the classical Derjaguin-Landau-Verwey-Overbeek (DLVO) theory that describes the response of charge-stabilized colloidal particles in terms of electrostatic and dispersion interactions (Russel et al., 1989; Larson, 1999).

It has been suggested (Matsumoto and Inoue, 1993; Inoue and Matsumoto, 1994; Ikeda and Nishinari, 2000; Matsumoto and Inoue, 1996; Inoue and Matsumoto, 1996) that the yield-like behavior observed in viscosity measurements on torsional rheometers arises from colloidal crystals formed by globular proteins that display long range interaction potentials with strengths up to $O(15kT)$ (Ikeda and Nishinari, 2000). But these same researchers (Matsumoto and Inoue, 1993; Inoue and Matsumoto, 1994; Ikeda and Nishinari, 2000; Matsumoto and Inoue, 1996; Inoue and Matsumoto, 1996) also noticed the lack of any solid-like structure in scattering data and observed that neither the concentration of proteins nor addition of salts changes the magnitude of the measured viscoelastic response. A recent study recognized that the small angle neutron scattering (SANS) data indicate absence of crystal structure (Oates et al., 2006) and another recent study (Regev et al., 2010) went as far as measuring interfacial rheology for BSA solutions, but both studies cite the presence of colloidal crystals invoked by Ikeda and Nishinari (2000). Our interface-free bulk viscosity measurements demonstrate that the yield stress and high interaction potentials of $O(15kT)$ result from systematic errors associated with fitting models to bulk rheology data that have a substantial interfacial contribution. Further, the value of $s$ obtained from the fit as described above implies that the effective inter-particle separation $d_{\text{eff}} = 2.5a$. Since a hard sphere suspension can form a colloidal lattice within the bulk (or subphase) only when $\phi_{\text{eff}} = \phi(d_{\text{eff}}/2a)^3 > 0.55$, a colloidal lattice can be expected only at $\phi > 0.3$ or for $c > 200$ mg ml$^{-1}$. This implies that the bulk rheological properties of these proteins can be well described by existing models, provided the

data are not corrupted by interfacial contributions. This comparison highlights the fact that apparent viscosity measured by rotational rheometers needs to be evaluated most carefully whenever surface-active molecules or dispersants are involved.

More broadly speaking, we note that since the same thermodynamic interactions determine the absolute value of osmotic pressure and therefore of viscosity, diffusion coefficient and scattering intensity, among other properties (Russel et al., 1989; Minton and Edelhoch, 1982), the response from different measurements should be consistent with each other so long as the microstructure is the same. The concentration-dependent osmotic pressure $\Pi(c)$ of dispersed colloidal particles or proteins (Russel et al., 1989; Larson, 1999) is given by $\Pi(c) = ckT[A_1 + A_2c + \ldots]$, where $A_1$ is related to size and $A_2$ is related to the interaction potential. For the pH and ionic content relevant to this study, the osmotic pressure of BSA solutions (Brownsey et al., 2003; Vilker et al., 1981; Wu and Prausnitz, 1999) corresponds to an interaction potential of $O(kT)$. Likewise, Minton and Edelhoch (1982) were able to fit light scattering data of BSA solutions from Edsall et al. (1950) with a model for charged colloidal suspension that describes the osmotic pressure $\Pi(c)$ for BSA. Countless other studies on hydrodynamic properties of well-dispersed BSA that report intrinsic viscosity, sedimentation equilibrium and diffusion measurements (Russel et al., 1989; Larson, 1999; Lefebvre, 1982; Richards, 1993; McMillan, 1974; Harding, 1997) find interaction potentials of $O(kT)$ and no evidence of any solid-like, long range structure in BSA solutions. Hence we conclude that the observed yield-like behavior observed in measurements on rotational rheometers arises in fact from the interfacial viscoelasticity of the adsorbed layer of proteins.

In colloidal dispersions, the yield stress presents a measure of interactions between the colloidal particles; these interactions are responsible for formation of a three-dimensional ordered macro-lattice structure. Therefore for colloidal dispersions, a simple first order estimate for yield stress can be made from the interaction potential (Larson, 1999; Quemada and Berli, 2002) by using $\sigma_Y \approx \phi U/Kd_{\text{eff}}^3$, where $K$ is an adjustable parameter—we use a typical value of $K = 0.33$, given in Larson (1999) and Quemada and Berli (2002). If we select an interaction energy of $U = 15k_BT$

for the BSA solutions and use the value of bulk yield stress measured as $10^{-2}$ Pa (from our data and representative of values reported by Ikeda and Nishinari (2000) and Regev et al. (2010)), the effective interparticle separation, $d_{\text{eff}}$ turns out to be $O(1\text{ mm})$ which is two orders of magnitude larger than the protein size. On the other hand, if we use the actual measured interfacial yield stress $\sigma_{Ys} \approx 2 \times 10^{-4}$ Pa m, and an interaction energy $U = k_B T$, the effective interparticle distance estimated using the corresponding interfacial expression $\sigma_{Ys} = \phi_s U / K d_{\text{eff}}^2$ turns out to be $d_{\text{eff}} = 6$ nm, which is close to the estimate obtained independently from the concentration dependence of viscosity. The high concentration of protein at the interface thus creates the apparent yield-like response. This yielding can be observed in both interfacial measurements and in the bulk rheology measurements whenever formation of a viscoelastic film can take place—for example when using a cone-and-plate geometry on a torsional rheometer.

## 3.6 Extracting interfacial viscosity contribution from bulk viscosity

In this section, we wish to show a simple but quantitative connection between the interfacial viscosity contribution $\eta_s(\dot{\gamma})$ (which is measured by the DWR) and the apparent bulk viscosity $\eta(\dot{\gamma})$ of the protein solution measured by a torsional rheometer for the double-gap (DG) and cone-and-plate geometries. We assume that the thickness of the interfacial film is small compared to the characteristic dimension of the chosen geometry and that the measured torque $M^x(\dot{\gamma})$ (where $M^x$ is a geometry identifier, and $x = DG$ for the double gap Couette geometry and $x = CP$ for the cone-and-plate geometry)from the rheometer is related to the shear stress contributed by the sub-phase fluid, $\tau_B = \eta_B(\dot{\gamma})\dot{\gamma}$ as well as to the interfacial contribution $\tau_s(\dot{\gamma}) = \eta_s(\dot{\gamma})\dot{\gamma}$ (units: Pa m), so that

$$M^{DG}(\dot{\gamma}) = 2[2\pi R(L-\delta)\tau_B + 2\pi R\tau_s]R \tag{3.6.1}$$

$$M^{CP}(\dot{\gamma}) = \int_0^{R-\delta} r\tau_B 2\pi r \, \mathrm{d}r + \int_{R-\delta}^{R} \frac{\tau_s}{\delta} 2\pi r \, r\mathrm{d}r \tag{3.6.2}$$

The interfacial deformations are localized over a length scale $\delta$. The bulk viscosity of the BSA solutions at high shear-rates $\eta_\infty$ (measured in the VROC) approaches the true zero shear rate viscosity as $\eta_\infty \approx \eta(\phi, \dot{\gamma} \to 0)$, implying that $\tau_B \approx \eta_\infty \dot{\gamma}$. Further, the interfacial contribution shown in Figure 3.4.1 can be modeled simply as a purely plastic or yielding event implying that the second term is given by $\tau_s = \tau_{sY} = G'_s \gamma_Y$, where the yield stress $\tau_{sY}$ obtained from oscillatory strain sweep measurements described earlier. Figure 3.6.1 shows the stress as a function of strain amplitude measured in a interfacial SAOS strain sweep test. The curves have been shifted using 50 mg ml$^{-1}$ as the reference concentration. The peak in the $G'_s\gamma_0$ curve (filled symbols in Figure 3.6.1) gives us the value of the yield stress $\tau_{sY}$. The corresponding interfacial viscosity is then $\eta_s(\dot{\gamma}) \equiv \tau_{sY}/\dot{\gamma}$, and is strongly shear thinning. The total shear rate viscosity $\eta(\dot{\gamma})$ reported by rheometer is then computed using

$$\eta^{DG}(\dot{\gamma}) \equiv \frac{M^{DG}(\dot{\gamma})}{4\pi R_i^2 L \dot{\gamma}} \approx \eta_B + l_G^{-1}\eta_s(\dot{\gamma}) \approx \eta_\infty + l_G^{-1}(\tau_{sY}/\dot{\gamma}) \tag{3.6.3}$$

$$\eta^{CP}(\dot{\gamma}) \equiv \frac{M^{CP}(\dot{\gamma})}{(2\pi R^3/3)\dot{\gamma}} \approx \eta_\infty + l_G^{-1}\eta_s(\dot{\gamma}) \approx \eta_\infty + l_G^{-1}(\tau_{sY}/\dot{\gamma}) \tag{3.6.4}$$

Here $R_i$ and $R$ are the radii of the double gap Couette and the cone respectively. The effective length scale $l_G$ appearing in Equations (3.6.3) and (3.6.4) accounts for the different dimensionality of the interfacial and bulk viscosity contribution, and is derived from the torque expressions to be $l_G = L$ for the DG geometry and $l_G = R/3$ for the CP. The close agreement between the measured value (symbols in Figure 3.6.2) and computed values for each geometry (solid line) shows that this simple Bingham-like model of a Newtonian-like bulk stress and a plastic/yielding interfacial contribution provides a good *a priori* estimate of the actual viscometric data measured with a bulk rheometer. Finally we note that Equation (3.6.3) can also be written $\eta(\dot{\gamma})/\eta_\infty \approx 1 + Bo_s^x$ where $Bo_s^x = \tau_{sY}/L(\eta_\infty\dot{\gamma})$ is the relevant Boussinesq number for the DG geometry. The interfacial contribution is dominant only when

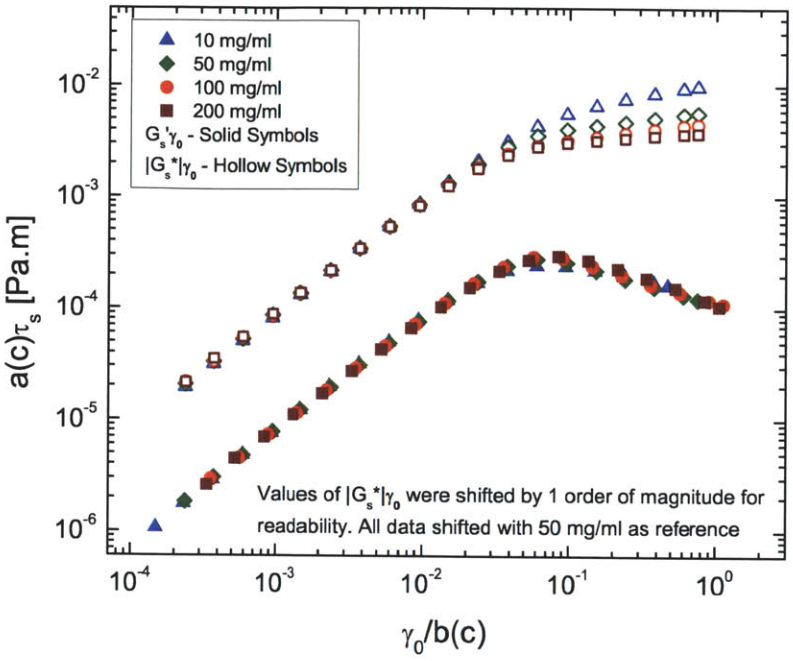


**Figure 3.6.1:** Mastercurve of shifted interfacial stress as a function of shifted shear strain for different concentration of BSA, shifted to a reference concentration of 50 mg ml$^{-1}$. The peak in $G_s'\gamma_0$ shows that the material yields plastically beyond of a critical strain of $\gamma_0 \approx 1\%$.

$Bo_s > 10$, and this is indeed the case for these BSA solutions as seen if Figure 3.6.3. It can be seen that the Boussinesq number decreases with increasing shear rate for all the geometries, although the requirement $Bo_s \gg 1$ holds even for the highest shear rates probed in this study. Furthermore, at the highest shear rates, the Boussinesq number $Bo_s$ reaches its lowest values, implying the interfacial contribution is weakest, and therefore the measurements from the DG geometry agree quite well with the interface-free microfluidic rheometer, as seen in Figure 3.2.1a. Similarly, the reason for the discrepancy between the bulk data measured with the DG fixture and that measured with the CP fixture can be understood by a similar argument based on the Boussinesq number. The ratio of the wetted area to the perimeter in a cone-and-plate device is $l_s^{CP} \approx \pi R^2/2\pi R = R/2 (\approx 10$ mm) compared to $l_s^{DG} = 2\pi RL/2\pi R = L(59.5$ mm) in the double gap fixture. The Boussinesq number is thus smaller in the DG fixture (which is also seen in Figure 3.6.3) for any surface active complex fluid and the interfacial effects are correspondingly less important in the measured torque.

Alternatively, measurements of the apparent bulk viscosity $\eta(\dot{\gamma})$ (measured with DG

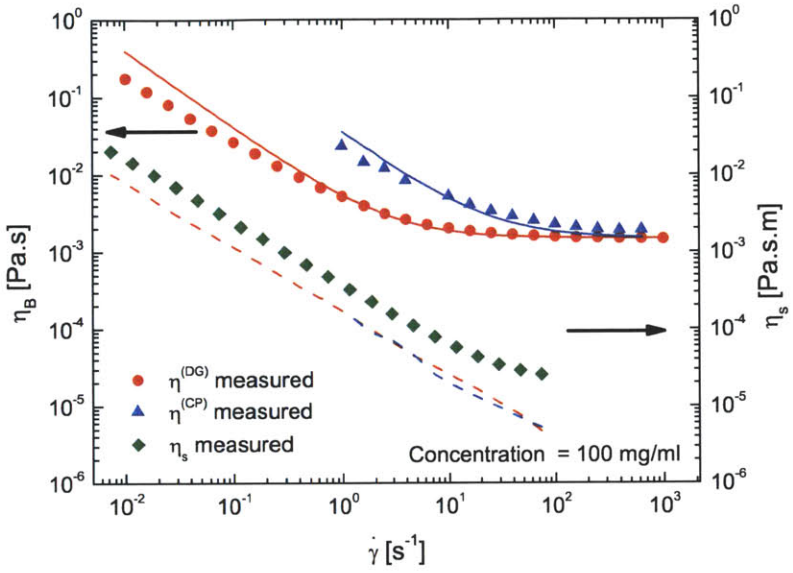


**Figure 3.6.2:** Comparison of the measured shear-rate-dependent viscosity response (blue and red symbols) to the model behavior (solid lines) computed by using the effective Bingham model (Equation (3.6.3)) for a 100mg $ml^{-1}$ BSA solution as a function of shear rate. The model response has two contributions: the bulk contribution is calculated using the high shear rate viscosity measured using a microfluidic rheometer and the interfacial contribution is computed using the apparent yield stress obtained from oscillatory strain sweep measurements (solid lines). Also shown is a comparison of measured interfacial viscosity $\eta_s$ (DWR)(diamonds) with the estimates (dashed lines) extracted using Equation (3.6.5)

.

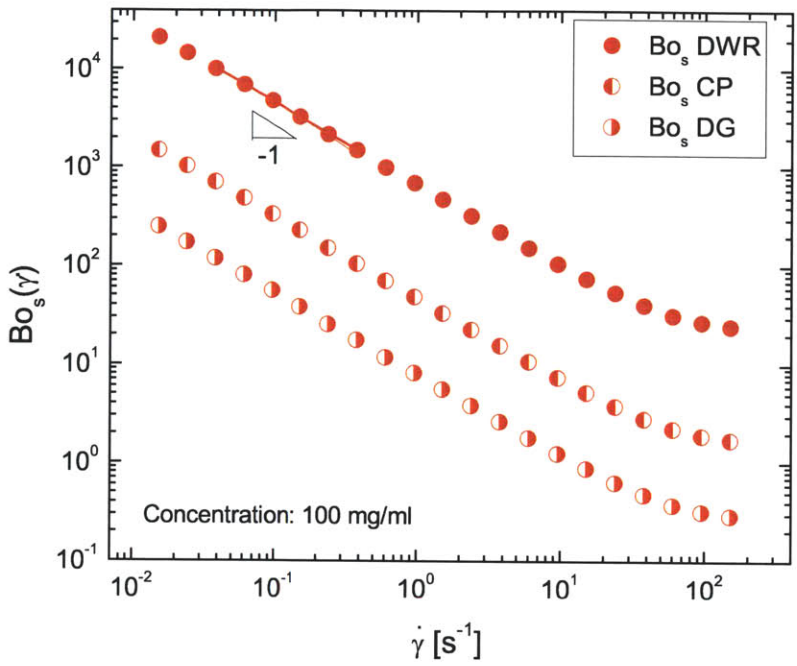


**Figure 3.6.3:** The values of the Boussinesq numbers for the different geometries used in this study as a function of shear rate for a 100 mg ml$^{-1}$ BSA sample. Even at the highest shear rates probed in this study, the requirement of $Bo_s \gg 1$ holds.

or CP), and the Newtonian viscosity $\eta_\infty$ measured in a microfluidic device (VROC) can be combined to estimate the rate-dependent interfacial viscosity contribution, by rearranging Equation (3.6.3) to give:

$$\eta_s(\dot{\gamma}) \approx l_G(\eta(\dot{\gamma}) - \eta_\infty) \tag{3.6.5}$$

Again the agreement between the estimates given by Equation (3.6.5) (dashed lines in Figure 3.6.2) and data measured independently using DWR (symbols) shows that the simple additive model captures the general trends quite well. The quantitative discrepancy arises because of the larger coupling between the interfacial and sub-phase deformation in a torsional rheometer which is not reflected in the simple linear decomposition of Equations (3.6.3) and (3.6.5). A similar discrepancy arises if we use two separate bulk viscosity measurements and solve for sub-phase viscosity and interfacial contribution using $\eta(\dot{\gamma}) \approx \eta_B + l_G^{-1}\eta_s(\dot{\gamma})$, where the geometry-dependent length scale $l_G$ is computed as described before. Thus, the accurate determination

of the interfacial contribution requires the use of a device like DWR with a high Boussinesq number, though a combination of bulk measurements can provide a qualitative measure of the interfacial viscosity. Interestingly, the estimate of the interfacial contribution also explains why the apparent bulk viscosity measured in the cone-and-plate geometry is higher than the double-gap geometry at all shear rates, as seen in Figure 3.2.1a. However, the internal consistency between this simple Bingham-like additive model and these distinct measurement techniques is quite encouraging, and could prove useful for deconvolving interfacial effects in other complex biofluids.

## 3.7 Conclusion

The kinetics of layer formation, the viscoelasticity and stability of the interface under applied deformation, and the intimate coupling between the interfacial and bulk viscosity behavior with shear rate tells us unambiguously that surfactant-free solutions of BSA (and possibly other globular proteins) form an interfacial film with a rich viscoelastic behavior at the solution/gas interface. The DWR geometry attached to a torsional rheometer provides the resolution and sensitivity required to effectively isolate the contribution of the interfacial layer whereas the microfluidic capillary rheometer (VROC) eliminates any free surface effects and measures the correct value of steady shear viscosity ($\eta_\infty$) at high shear rates. By contrast the measured or apparent viscosity $\eta(\dot{\gamma})$ obtained from rotational rheometers is superficially high due to the adsorbed, interfacial protein film and the relative bulk and interfacial contributions depend upon the specific test fixture selected. We have investigated in this thesis the interfacial and bulk properties independently, and shown that the osmotic pressure, diffusion coefficient, scattering and intrinsic viscosity measurements of BSA solutions can all be described self-consistently, and we do not need to invoke any special long-range interactions or colloidal microstructures. We provide a simple model that provides an understanding of the connection between the interfacial viscosity and bulk viscosity measurements.

It must be remarked here that serum albumins are important constituents of blood.

Blood is a multi-component complex fluid that displays a highly non-Newtonian response to deformation amplitude and rate in bulk rheometry (Picart et al., 1998).The apparent yield-like behavior provides blood with the necessary rheological properties required for the physiological function: it makes stopping blood flow easier, while providing low resistance (and a low pumping cost) to deformation at high flow rates (Merrill, 1969). In fact, the contribution of serum albumins to overall blood rheology has been of long standing interest, and the early hemorheology literature (Merrill, 1969; Bingham, 1945; Scott Blair, 1959) is dominated by the pioneering studies of Bingham (1945); Scott Blair (1959); Merrill (1969), Copley and Ferry. We refer specifically to a review, where Merrill (1969) notes that

> ...serum usually presents some form of experimental artifact in viscometry, attributable to a tendency toward rigid or semirigid surface films.

As we have noted already, this seems to be neglected in many recent studies (Matsumoto and Inoue, 1993; Inoue and Matsumoto, 1994; Ikeda and Nishinari, 2000; Matsumoto and Inoue, 1996; Inoue and Matsumoto, 1996; Ikeda and Nishinari, 2001a,b; Regev et al., 2010; Oates et al., 2006; Brownsey et al., 2003). Further, Merrill notes presciently that

> ...when the rotational viscometer is operated with a guard ring (which eliminates the interface) or when a capillary viscometer is operated such that flow rate is the imposed parameter and pressure gradient (measured by transducer in a gas free circuit) is the observed response, plasma and serum are Newtonian, down to zero strain rate and up to at least several inverse seconds of strain rate.

Our results with the microfluidic rheometer show that the Newtonian regime in fact extends out to $\dot{\gamma} \geq 10^4\ \mathrm{s}^{-1}$ for BSA solutions. While Merrill refers to studies in the 1960s that identified interfacial effects as the cause for apparent yield stress, Newtonian response of serum was observed earlier by several researchers including Scott Blair (1959) and Tanford and Buzzell (1956). Apparently, more recent rheological studies on globular proteins (Matsumoto and Inoue, 1993; Inoue and Matsumoto,

1994; Ikeda and Nishinari, 2000; Matsumoto and Inoue, 1996; Inoue and Matsumoto, 1996; Ikeda and Nishinari, 2001a,b; Regev et al., 2010; Oates et al., 2006; Brownsey et al., 2003) seem to be unaware of these historical studies, and their assertion that the apparent yield stress of globular proteins arises from an underlying colloidal crystal microstructure has started to propagate in the literature a somewhat erroneous idea that globular proteins have long range interactions that are markedly stronger than electrostatic repulsions. Indeed, the interaction potential of $O(kT)$ computed by using DLVO theory agrees very well with the interaction energy estimated by using concentration-dependence of bulk viscosity as measured in the interface-free rheometer and independently from the interfacial yield stress measured using the double wall ring geometry.

While the current study focused on surfactant-free protein solutions, the experimental protocol, and simple additive rheological model described herein can be adopted for the complex mixed interfaces expected for multicomponent biological and industrial fluids and mixtures of protein and surfactant are discussed in the next chapter. Although the interfacial viscosity of lung surfactants is known to play an important role in their functioning (Zasadzinski et al., 2001), the physiological importance of interfacial viscosity and viscoelasticity of serum albumins, globular proteins, monoclonal antibodies and saliva remains to be elucidated. It is evident, however, that in designing synthetic biofluid replacements or pharmaceutical formulations containing surface active molecules, the formation, structure and rheological properties of interfaces must be taken into account, especially where the formation of a viscoelastic film at the liquid-air interface is known to occur.

# Chapter 4

# Interfacial Rheology of Protein-Surfactant Mixtures

## 4.1 Introduction

Surface-active materials like proteins, low molecular weight surfactants and polymeric surfactants adsorb to fluid interfaces, effectively reducing the interfacial tension, and endowing the interface with additional independent material properties such as surface elasticity and viscosity (Edwards et al., 1991; Miller and Liggieri, 2009). The dynamic interfacial properties of these adsorbed interfacial layers are important for a number of technological applications including foam and emulsion formation and stabilization in food processing (Murray, 2010; Murray and Dickinson, 1996), cosmetics and pharmaceutical industry (Murray and Dickinson, 1996; Dickinson, 1992b). The interfacial viscoelasticity also plays an important role in spray coating, Langmuir-Blodgett deposition, liquid-liquid deposition, two phase flows and mass transfer (Edwards et al., 1991; Miller and Liggieri, 2009). Multicomponent mixtures of proteins and surfactants are used in many of these applications, and the addition of surfactants to protein solutions can substantially modify the physiochemical properties of the resulting interface (Miller and Liggieri, 2009; Bos and Van Vliet, 2001; Krägel et al., 1999; Mobius and Miller, 1998; Kotsmar et al., 2009). For example, the interfacial shear viscosity (which characterizes resistance to changes in shape at constant

area on a two-dimensional interface), is affected by the structure, composition and conformation of the interfacial components of these mixed systems (Murray, 2010; Bos and Van Vliet, 2001; Krägel et al., 1999; Mobius and Miller, 1998; Maldonado-Valderrama et al., 2007). In this study, we focus on the interfacial and bulk rheology of a protein-surfactant mixture, using solutions of a model globular protein, Bovine Serum Albumin, mixed with a non-ionic surfactant—polysorbate 80 (or Tween 80$^{TM}$).

When the rheological properties of globular protein solutions such as Bovine Serum Albumin (BSA) are tested in a torsional rheometer, they exhibit yield-like behaviour at surprisingly low concentrations of 0.03%-10% (Matsumoto and Chiba, 1990; Matsumoto and Inoue, 1993; Ikeda and Nishinari, 2000; Regev et al., 2010) and show pronounced shear thinning at low shear rates, as discussed in detail in the previous chapter. Every surface-active material that forms a viscoelastic film at the liquid/air interface can lead to a measurable apparent yielding behavior, as long as the interfacial yield stress (the last term in Equation (3.6.3)) is significant. The presence of an apparent yield stress in the bulk rheological measurement is also reported for solutions of ovalbumin (Ikeda and Nishinari, 2001a), saliva (Waterman et al., 1988), monoclonal antibodies (Patapoff and Esue, 2009) and acacia gum (Sanchez et al., 2002). In practice, the interfacial contribution from surface-active components in multicomponent fluids can be suppressed by the addition of a low molecular-weight mobile surfactant, which competes with the protein for adsorption onto the interface. In this chapter, we examine the bulk and interfacial rheological response of protein-surfactant mixtures, specifically to evaluate how addition of a surfactant to a protein solution changes the dynamical properties of the interface.

Protein-surfactant mixtures are commonly found in many biological systems (Mobius and Miller, 1998; Biswas and Haydon, 1963; Ariola et al., 2006), and indeed, blood itself is a mixture of serum albumins along with various other surface-active components (Mobius and Miller, 1998; Ariola et al., 2006). In fact, serum albumins are one of the most widely encountered proteins in mammalian blood and are vitally important in diverse biological functions, such as maintaining blood pH and osmotic pressure as well as transporting ligands, metabolites, lipophilic compounds, hormones

and drugs, including anesthetics and anti-coagulants (Peters, 1996; Carter and Ho, 1994). The concentration of Human Serum Albumin (HSA) in human blood is about 50 mg/ml and contributes about 80% of the total colloidal osmotic blood pressure (Carter and Ho, 1994). Due to their ubiquity and the important role they play in various biological processes, serum albumins are important model systems for understanding the bulk and interfacial rheology of globular proteins. We specifically choose Bovine serum albumin (BSA) for our study because its physical properties are similar to Human serum albumin (Peters, 1996), and is widely used as a model protein in many globular protein studies. The quantitative study of mixed protein-surfactant systems is necessary for understanding the rheological response of multicomponent fluids where surfactants are invariably present.

While the possibility that interfacial tension can be used as an indicator for certain diseases was first studied almost a century ago (Morgan and Woodward, 1913), measurement of the interfacial rheology of these protein mixtures presents considerable challenges. Non-ionic surfactants compete with the protein molecules for adsorption at the interface giving rise to complex dynamics. The extent of competition is dependent on the molar ratio of surfactant to protein (Dickinson and Hong, 1994). The irreversibility of the adsorption, the presence of heterogeneous domains, significant interfacial phase separation at the interface and the sensitivity of the structure of the interfacial layer to the adsorption history make accurate measurements a challenging task Murray (2010); Murray and Dickinson (1996); Dominique Langevin (2009). Dickinson, amongst others (Miller and Liggieri, 2009; Kotsmar et al., 2009; Grigoriev et al., 2006), has co-authored a series of papers that discuss this competitive adsorption between proteins and low molecular weight surfactants (Dickinson and Hong, 1994; Courthaudon et al., 1991a,b; Chen and Dickinson, 1995). Given these challenges, a simple experimental protocol that provides a check for the presence of surface viscoelasticity and an estimate of its magnitude in protein-surfactant mixtures will be of utility to the community at large.

In this paper we first review the concept of creep ringing or "free-oscillations" in creep experiments under constant stress. We then show how this inertio-elastic

effect impacts interfacial creep measurements performed with a new interfacial experimental fixture, the DWR fixture, and how it can be exploited to make quick and accurate measurements of viscoelastic moduli for Bovine Serum Albumin (BSA) solutions. We compare these measurements with interfacial small amplitude oscillatory strain experiments (SAOS) and then study the effect of adding a non-ionic surfactant (Polysorbate 80) to the BSA solutions using the creep-ringing technique. Finally, we re-emphasize the importance of correctly accounting for interfacial effects in the bulk of protein solution rheometry and elucidate the effect of added surfactants on bulk rheological measurements.

## 4.2 Creep Ringing

Inertial effects are almost always unavoidable in controlled-stress rheometry, especially in step-stress and impulse-response experiments (Walters, 1975). The angular acceleration of the fixture is retarded by the moment of inertia of the spindle of the torsional rheometer, and the attached geometry. The coupling between this moment of inertia and the fluid viscoelasticity is seen in the general equation of motion of the fluid in step-stress experiments (Ewoldt and McKinley, 2007)

$$\frac{I}{b}\ddot{\gamma}(t) = H(t)\tau_0 - \tau(t) \tag{4.2.1}$$

Where $I$ is the sum of the moment of inertia contributions from the rheometer and the attached geometry (units: kg m$^2$), $\gamma$ is the strain in the sample, $H(t)$ is the Heaviside step function, $\tau_0$ is the magnitude of the step in the applied stress and $\tau(t)$ is the retarding stress exerted by the sample on the fixture. The double over-dot indicates the second derivative with respect to time. The parameter $b$ is a combination of geometric factors (units: m$^3$) and is determined by the specific instrument and geometry used. The factors $F_\gamma = \dot{\gamma}/\omega$ (dimensionless) and $F_\sigma = \tau/T$ (units: m$^{-3}$) are geometric parameters that convert the measured variables of angular velocity $\omega$ and torque $T$ to shear rate $\dot{\gamma}$ and shear stress $\tau$ respectively. It can instantly be seen

from Equation (4.2.1) that due to the non-zero inertia of the system, $\tau(t) \neq H(t)\tau_0$.

For a Newtonian fluid, $\tau(t) = \eta\dot{\gamma}(t)$, and in the absence of inertia, the solution to Equation (4.2.1) gives the expected linear response $\gamma(t) = (\tau_0/\eta)t$. However, for non-zero inertia, the strain $\gamma(t)$ is given by

$$\gamma(t) = \frac{\tau_0}{\eta}\left[t - \frac{I}{b\eta}\left(1 - \exp\left(-\frac{b\eta}{I}t\right)\right)\right] \tag{4.2.2}$$

The characteristic time constant for this exponential response is $t_c = I/b\eta$. At long times $t > 3I/b\eta$, the expected linear system response is recovered but the strain is retarded by a factor and $\gamma(t) = (\tau_0/\eta)(t - t_c)$. For $t \ll I/b\eta$, the exponential term in Equation (4.2.2) can be expanded to obtain

$$\gamma(t) = (\tau_0 b/2I)t^2 + O(t^3) \tag{4.2.3}$$

and hence the short time response is quadratic as expected from Newtons second law, (i. e), at very early times,

$$\frac{I}{b}\ddot{\gamma} = H(t)\tau_0 \Rightarrow \gamma(t) = (\tau_0 b/2I)t^2 \tag{4.2.4}$$

It should be noted that this short-time creep response is independent of the fluid rheology and is valid for all test fluids at sufficiently early times.

When the equation of motion (Equation (4.2.1)) is coupled with a viscoelastic constitutive model, the presence of the inertial term leads to a damped oscillatory response during creep experiments. (See Ewoldt and McKinley (2007); Baravian and Quemada (1998) and the Results section for the exact form of this strain response). These oscillatory dynamics often cloud the short time creep response and are generally considered undesirable. However, Struik (1967) and others (for example Baravian and Quemada (1998)) have described procedures from which one can extract bulk viscoelastic storage and loss moduli using this creep-ringing or free oscillation. In this chapter, we show how this analysis can also be adapted in order to use creep ringing measurements with the DWR fixture to extract the interfacial viscoelastic

properties of an adsorbed protein film.

## 4.3 Interfacial Creep Ringing Theory

In this chapter, the bulk creep ringing formulation outlined above is adapted for the extraction of interfacial moduli, which, to the best of the author's knowledge, has not been discussed in the literature to date. The equation of motion for the DWR fixture and associated spindle is first considered:

$$I\frac{d\Omega}{dt} = T^a - T^b \tag{4.3.1}$$

where $\Omega$ is the angular velocity of the shaft to which the DWR is attached, $T^a$ is the applied torque and $T^b$ is the resisting torque acting on the ring. The interfacial stress $\tau_s$ is related to the torque through the interfacial stress factor $F_\sigma$ (which now has units of $\mathrm{m}^{-2}$ instead of $\mathrm{m}^{-3}$ in the bulk case) and hence $\tau_s^a = F_\sigma T^a$ and $\tau_s^b = F_\sigma T^b$. Because the strain rate factor $F_\gamma$ is dimensionless, its units are unchanged from the bulk to interfacial transformation and $\dot{\gamma} = F_\gamma \Sigma$ as before. Equation (4.3.1) then reduces to

$$\frac{I}{b_s}\ddot{\gamma} = \tau_s^a - \tau_s^b \tag{4.3.2}$$

The subscript $s$ denotes a surface or interfacial quantity. For a step-stress or creep experiment, the applied interfacial stress $\tau_s^a = H(t)\tau_0^s$ and it can be seen that Equation (4.3.2) is the interfacial counterpart of Equation (4.2.1). We note that the measurement system factor $b_s$ now has units of $\mathrm{m}^2$, since the interfacial stress $\tau_s$ is a force per unit length and has units of N $\mathrm{m}^{-1}$ or Pa m.

To solve this equation of motion for the DWR fixture, an appropriate rheological constitutive equation for the interface must be selected. Following the corresponding bulk formulations of Baravian and Quemada (1998) and Ewoldt and McKinley (2007) the interfacial layer of globular protein is modeled using a three-parameter linear viscoelastic Jeffreys model. The model consists of a Voigt element (a spring and dashpot in parallel) in series with a dashpot, with an added element to model the

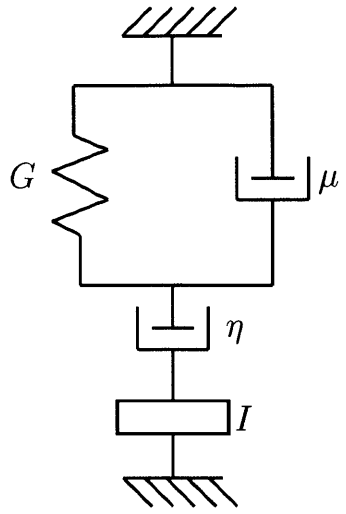


**Figure 4.3.1:** A schematic of the linear viscoelastic Jeffreys model, which consists of a spring and a dashpot in parallel (Kelvin-Voigt element) in series with a dashpot. Note the addition of the fourth element $I$ which represents the instrument inertia and is the source for creep ringing.

inertia. A schematic of this model is shown in Figure 4.3.1. At long times, the Voigt element attains a steady deformation when loaded under controlled stress conditions and hence the remaining dashpot ($\eta$) leads to a fluid-like response of the adsorbed protein interface ($\gamma(t) = (\tau_0/\eta)t$). Conversely, taking the Kelvin-Voigt model alone, for example, would give a constant strain at long times and hence a solid-like interfacial response. Since a steady-state flow is observed at long times during interfacial creep experiments (see the next section), the Jeffreys model is used to fit the data. Tschoegl (1989) provides a detailed discussion on these simple two- and three-parameter models as well as more complicated models, and the reader is referred there for more information. For the Jeffreys model, the constitutive equation is,

$$\left(1 + \frac{\mu}{\eta}\right)\dot{\tau}_s + \frac{G_s}{\eta}\tau_s = G_s\dot{\gamma} + \mu\ddot{\gamma} \tag{4.3.3}$$

where $G_s$ (units: Pa m), $\mu$ and $\eta$ (units: Pa s m) are the three parameters in the model. Equation (4.3.3) is then coupled with Equation (6) to obtain the full equation

of motion for the DWR fixture

$$\left(1+\frac{\mu}{\eta}\right)\ddot{\gamma}+\left[G_s/\eta+\frac{\mu}{I/b_s}\right]\dot{\gamma}+\frac{G_s}{I/b_s}\gamma=\frac{G_s}{\eta(I/b_s)}\tau_0 t+\frac{(1+\mu/\eta)}{I/b_s}\tau_0 H(t) \quad (4.3.4)$$

Here, the imposed stress is $\tau_s^a = H(t)\tau_0$ for a creep experiment. This second order differential equation can be solved explicitly as a function of time (Ewoldt and McKinley, 2007):

$$\gamma(t)=\frac{\tau_0}{\eta}t-B+e^{-At}\left[B\cos(\omega t)+\frac{A}{\omega}\left(B-\frac{\tau_0}{\eta A}\right)\sin(\omega t)\right] \quad (4.3.5)$$

where

$$\omega=\sqrt{\frac{G_s}{\alpha_s}\frac{\eta}{\mu+\eta}-A^2}$$

$$A=\frac{G_s/\eta+\mu/\alpha_s}{2(1+\mu/\eta)}$$

$$B=\frac{\tau_0}{G_s}\frac{(\mu+\eta)}{\eta}\left(\frac{2A\alpha_s}{\eta}-1\right)$$

Here, the factor $\alpha_s = I/b_s$ is introduced for compactness. The viscoelastic storage and loss moduli for the Jeffreys model are given respectively by the following expressions (Ewoldt and McKinley, 2007)

$$G_s'=G_s\frac{(\lambda_2\omega)^2}{1+(\lambda_1\omega)^2} \quad (4.3.6)$$

$$G_s''=G_s\frac{(\lambda_2\omega)\left[1+(\lambda_1^2-\lambda_1\lambda_2)\omega^2\right]}{1+(\lambda_1\omega)^2} \quad (4.3.7)$$

where $\lambda_1 = (\mu+\eta)/G_s$ and $\lambda_2 = \eta/G_s$ are the relaxation time and retardation time respectively. For creep ringing to be observed, the system response to Equation (4.3.4) needs to be under-damped, and hence we require $G_s > G_{critical} = A^2\alpha_s(1+\mu/\eta)$. Under these conditions, data from creep experiments can then be fitted with Equation (4.3.5) and the interfacial storage and loss modulus of the interface can be cal-

culated using Equations (4.3.6) and (4.3.7) after a least square fit over $G_s$, $\mu$ and $\eta$ is carried out. Alternatively, Struik (1967) has demonstrated that, under certain conditions (given below), the linear viscoelastic moduli can be approximated directly by using the logarithmic decrement and the frequency of the creep ringing. Because Equation (4.3.2) is identical to the equation of motion for free oscillations of a standard torsional device, one can readily adapt Struik's formulae to obtain the following expressions for the interfacial viscoelastic moduli:

$$G_s' \approx \alpha_s \omega_*^2 \left[1 + \left(\frac{\Delta}{2\pi}\right)^2\right] \tag{4.3.8}$$

$$G_s'' \approx \alpha_s \omega_*^2 \left(\frac{\Delta}{\pi}\right) \tag{4.3.9}$$

$$\tan\delta \approx \frac{\Delta/\pi}{\left[1 + \left(\frac{\Delta}{2\pi}\right)^2\right]} \tag{4.3.10}$$

where $G_s'$ and $G_s''$ are the interfacial viscoelastic storage and loss moduli respectively (units: Pa.m), $\tan\delta$ is the tangent of the phase angle $\delta$, $\omega_*$ is the ringing frequency (units: rad $s^{-1}$), $\Delta = \ln(A_{n+1}/A_n)$ is the logarithmic decrement (where $A_n$ is the amplitude of the $n^{th}$ peak or trough). These expressions provide estimates for the linear viscoelastic moduli without the assumption of an underlying model provided the logarithmic decrement $\Delta$ is small, and the instrument compliance and fluid inertia are negligible.

## 4.4 Interfacial Creep Ringing of BSA solutions

To extract the viscoelastic storage and loss moduli for the BSA solutions, the interfacial creep ringing procedure outlined above is used. Using the Double Wall Ring (DWR) fixture, the strain response is measured as a function of time for different values of interfacial stress $\tau_0$ in creep experiments, as shown in Figure 4.4.1. The coupling between surface elasticity and instrument inertia leads to the periodic and

exponentially decaying oscillations seen for $t \leq 2$ s, expected from Equation (4.3.5). Although the amplitude of the oscillations increases with the magnitude of the imposed stress $\tau_0$ , the frequency of ringing is determined only by the surface elasticity and the geometry of the DWR (see Equations (4.3.8), (4.3.9) and (4.3.10)). The inset to Figure 4.4.1 shows the short tine response for a creep experiment performed at $\tau_0 = 3 \times 10^{-6}$ Pa m. Using a Taylor series expansion of Equation (4.3.5), and neglecting cubic and higher order terms, it can be shown that for short times that $\gamma(t) \approx (\tau_0/2\alpha_s)t^2$ and the short-time response is quadratic in time, as anticipated in Equation (4.2.2). Fitting a pure quadratic polynomial to the measured short time creep response (red line in the inset of Figure 4.4.1), we find $\alpha_s^{(m)} = 1.85 \times 10^{-4}$. The parameter $\alpha_s = I/b_s$ is a characteristic parameter of the instrumentation, since the total moment of inertia of the system $I$ can be calibrated independently, and the factor $b_s$ is determined by the geometry being used (for the DWR used in this study, $F_\gamma = 9.393$ and $F_\sigma = 64.94$ m$^{-2}$ giving $b_s = 0.144$ m$^2$). For the experimental configuration used here, $\alpha_s$ was calculated to be $\alpha_s^{(c)} = 1.72 \times 10^{-4}$ kg. Using this value of $\alpha_s$, Equations (4.3.8) and (4.3.9) were used to estimate the interfacial viscoelastic moduli from the logarithmic decrement method and give $G_s' \approx 0.021$ Pa m and $G_s'' \approx 3.8 \times 10^{-3}$ Pa m respectively. Hence, from a single creep experiment, both the inertia of the measurement system as well as the viscoelasticity of the adsorbed interfacial protein layer can be determined.

A fit of the linear viscoelastic Jeffreys model (Equation (4.3.5)) to the interfacial creep ringing experiment with was carried out with MATLAB and is shown in Figure 4.4.2. From the fit parameters, the interfacial storage and loss moduli can be calculated using Equations (4.3.6) and (4.3.7) respectively to give $G_s' \approx 0.018$ Pa m and $G_s'' \approx 4.4 \times 10^{-3}$ Pa m. It can be seen that the fit to the Jeffreys model is good at short times, but progressive deviations from linearity are seen for $t > 3$ s as the total strain accumulated by the interface increases.

To investigate the onset of nonlinearity, small amplitude oscillatory strain sweeps and frequency sweeps with the DWR fixture were also performed and are presented in Figures 4.4.3a and 4.4.3b. In Figure 4.4.3a, the onset of nonlinear response in the

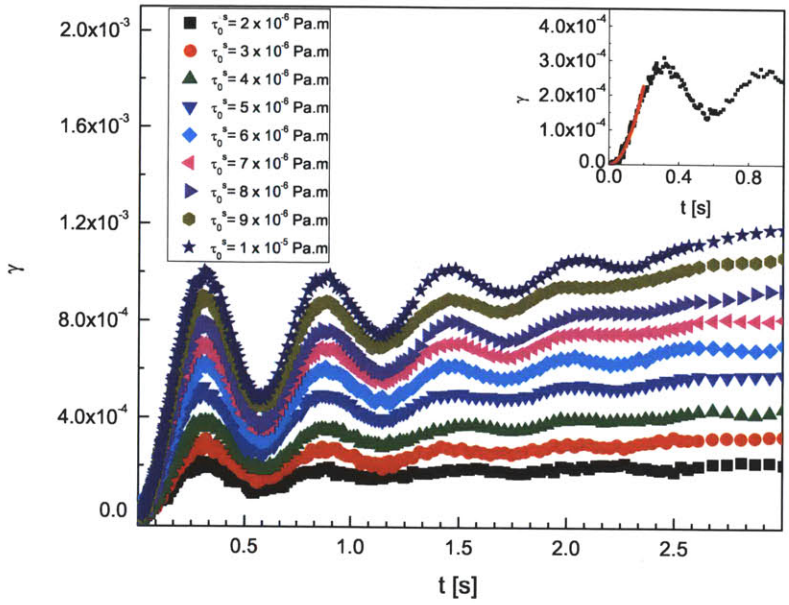


**Figure 4.4.1:** Interfacial creep ringing experiments performed on 50 mg/ml BSA using the DWR geometry attached to a stress controlled rheometer (ARG2) for different values of applied stress $\tau_0$. While the amplitude of ringing increases with increasing stress, the ringing frequency remains the same. The inset shows the short time response for $\tau_0 = 3 \times 10^{-6}$ Pa m. The red line is a quadratic fit to the short time response. The measured value of $\alpha_s^{(m)} = 1.85 \times 10^{-4}$ kg extracted from the fit is in close agreement with the calculated value of $\alpha_s^{(c)} = 1.72 \times 10^{-4}$ kg.

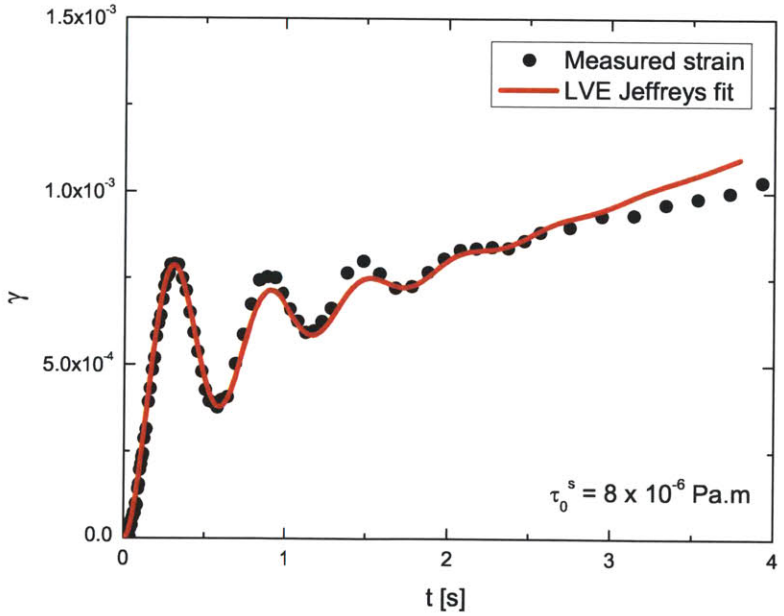


**Figure 4.4.2:** Fit of a linear viscoelastic Jeffreys model to the short time response of an interfacial creep experiment. While the short time ringing response is fit well by this model, the beginning of deviations from linearity can be seen for $t > 3$ s.

| Quantity | Estimation method | | |
|---|---|---|---|
| | Log Decrement | Jeffreys fit | SAOS |
| $G_s'$ [Pa m] | 0.021 | 0.018 | 0.023 |
| $G_s''$ [Pa m] | $3.8 \times 10^{-3}$ | $4.4 \times 10^{-3}$ | $4.6 \times 10^{-3}$ |

**Table 4.4.1:** Values of the interfacial viscoelastic moduli for 50 mg/ml BSA solutions obtained by the three independent methods described in the text; namely a fit to the linear Jeffreys model (Equations (4.3.6) and (4.3.7)), evaluation of the logarithmic decrement (Equations (4.3.8) and (4.3.9)), and small amplitude oscillatory interfacial shear flow (SAOS).

viscoelastic interfacial layer can be seen to occur at a strain amplitude of $\gamma_0 \approx 4\%$. For $\gamma_0 \leq 4\%$, the interfacial elastic modulus $G_s'$ is larger than the interfacial loss modulus $G_s''$, indicating that the interfacial layer exhibits viscoelastic solid-like properties at small/moderate strains. The rapid collapse in the magnitude of $G_s'$ and the dominance of the viscous response $G_s''$ for strains beyond $\gamma_0 \approx 5\%$ is indicative of a yielding process in the interfacial film. We note that the values of $G_s'$ and $G_s''$ obtained from the damped free-oscillation measurements during creep ringing and the value extracted from the fit to the Jeffreys model (Equation 4.4.1) agree well with the corresponding SAOS measurements at the appropriate frequency $\omega_*$. These values are summarized in Table 4.4.1. From the crossover frequency in Figure 4.4.3b, the relaxation time of the viscoelastic BSA interface was estimated to be $\lambda = 6.5$ s.

A strong case for using creep ringing observations to estimate the viscoelastic properties of the interfacial film is made from the inertial effects seen for $\gamma_0 > 2\%$ in Figure 4.4.3a and for $\omega > 10$ rad s$^{-1}$ in Figure 4.4.3b. These inertial effects can corrupt the experimental data and limit the range of measurable frequencies or strains in a small amplitude oscillatory measurement. Baravian and Quemada (1998) have pointed out that creep ringing extends the range of measurable frequencies in a frequency sweep test. The raw phase angles for the high frequency and large strain data presented in Figures 4.4.3a and 4.4.3b (not shown here) were also greater than 90°, indicating the importance of inertial effects. Because interfacial creep ringing accounts for, and in fact exploits, the finite moment of inertia of the measurement system, the range of measurable frequencies is extended beyond what is possible in a

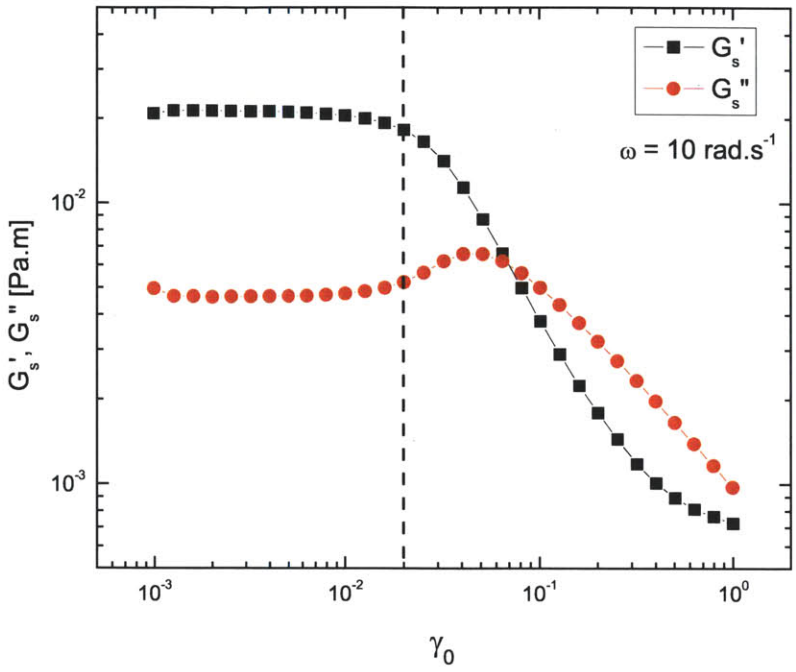


(a) Interfacial small amplitude strain sweep

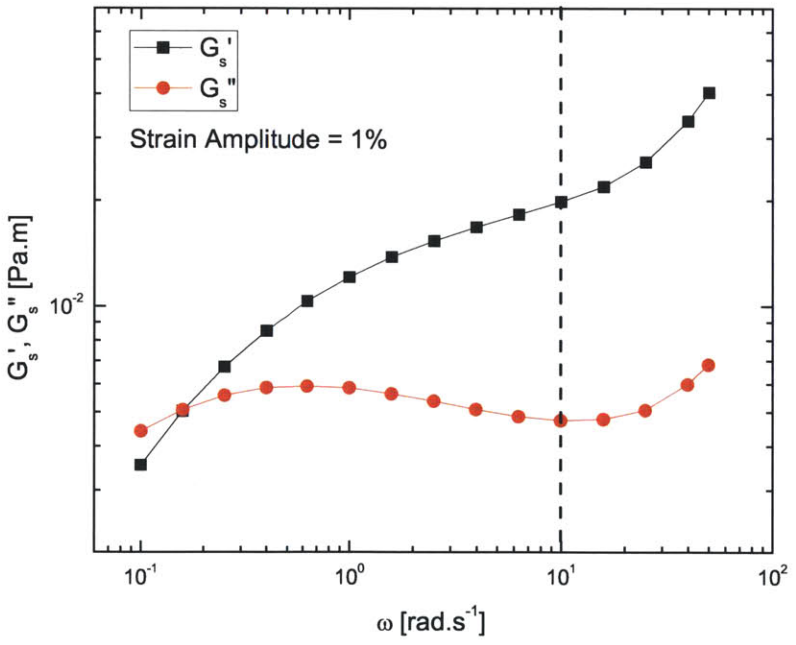


(b)

**Figure 4.4.3:** (a) Interfacial small amplitude oscillatory strain sweep for 50 mg/ml BSA performed at angular frequency $\omega = 10$ rad s$^{-1}$. Beyond a strain amplitude of $\gamma_0 = 2 \times 10^{-2}$ (2%), the interfacial film yields plastically. In the linear viscoelastic region, $G'_s = 0.022$ Pa m. (b) Interfacial small amplitude oscillatory frequency sweep for 50 mg/ml BSA solution. At $\omega = 10$ rad s$^{-1}$, $G'_s = 0.021$ Pa m. Inertial effects are visible in the region to the right of the dashed line. From the crossover frequency, the relaxation time $\lambda$ is estimated to be $\lambda \approx 6.5$ s. Inertial effects are visible for $\omega > 11$ rad s$^{-1}$.

standard frequency sweep. From Equation (4.3.5), we see that $\omega_*$ varies inversely with $\alpha_s$, which in turn depends on the geometric factor $b_s$ and hence designing appropriate interfacial geometries with smaller values of $\alpha_s$ enables one to probe progressively higher frequencies without inertial distortions like those seen in Figure 4.4.3.

To show this, we assume the logarithmic decrement is small, and we have from Equation (4.3.8)

$$G'_s = \frac{I\omega^2}{b_s} \tag{4.4.1}$$

$$\Rightarrow \omega_* = \sqrt{\frac{G'_s F_\gamma}{I F_\tau}} \tag{4.4.2}$$

$$= \sqrt{\frac{G'_s\left(\dfrac{R_4^2}{R_4^2 - R^2} + \dfrac{R_1^2}{R^2 - R_1^2}\right)}{(I_r + \rho\pi a^2 R^3)[1/2\pi(R_2^2 + R_3^2)]}} \tag{4.4.3}$$

where $a$ is the thickness of the ring, $\rho$ is the density of the material of the ring and $I_r$ is the moment of inertia of the spindle, so that $I_r + \rho\pi a^2 R = I_{\text{total}}$, is the total moment of inertia of the rotating system. The values of the shear stress factor $F_\tau$ and the shear rate factor $F_\gamma$ have been substituted from Equations (2.1.11) and (2.1.12) respectively. We now make the assumption that $R_3 \approx R_4 = R$. We also know that $(R_4 - R) = (R - R_1) = \Delta R$ (see pp. 32 for dimensions). Under these assumptions we can show that Equation (4.4.3) simplifies to

$$\omega_* = 4R^2\sqrt{\frac{G'_s\pi R}{\Delta R(4R^2 - \Delta R^2)(I_r + \rho\pi a^2 R^3)}} \tag{4.4.4}$$

$$= 4R\sqrt{\frac{G'_s\pi}{(I_r + \rho\pi a^2 R^3)\lambda(4 - \lambda^2)}} \tag{4.4.5}$$

where $\lambda = \Delta R/R$. For the ring used in this study, the dimensions of the ring (given in Chapter 2, pp. 32) show that $\Delta R/R = (39.5 - 35)/35 \approx 0.1$ and hence we have $4 - \lambda^2 \approx 4$. Using this result in Equation (4.4.5), we obtain

$$\omega \approx 2R\sqrt{\frac{G'_s\pi}{\lambda(I_r + \rho\pi a^2 R^3)}} \tag{4.4.6}$$

For the experimental set up used here, $I_r = 17.97 \times 10^{-6}$ kg m$^2$ and $\rho\pi a^2 R^3 \approx 8 \times 10^{-6}$ kg m$^2$, which is almost 50% of $I_r$, and hence we cannot ignore the inertial contribution of one or the other.

We see that for a given value of the elastic modulus $G'_s$, the ringing frequency $\omega$ be tuned using a number of different of parameters—the radius $R$ of the ring used, the spacing between the ring and the trough $\Delta R$ and the density of the material of the ring $\rho$. We note that the relationship between the ringing frequency and ring dimensions is complicated, and the frequency doesn't scale with a simple power law of the radius $R$ of the ring.

The interfacial creep compliance $J_s(t) = \gamma(t)/\tau_0$ for different values of interfacial stress $\tau_0$ is shown in Figure 4.4.4. For an ideal linear viscoelastic material, the compliance curves will all collapse onto each other. Moreover, for the linear Jeffreys model, the third term in Equation (4.3.5) is negligible at long times, and the strain (or compliance) will increase linearly with time. Inspection of Figure 4.4.4 shows that neither of these conditions is satisfied for the BSA interface at large strains. While the compliance curves all collapse at short times (in the region where creep ringing is present), they deviate progressively from each other for $t \geq 5$ s. Figure 4.4.5 shows the strains measured during creep experiments performed at two different stress values on a log-log scale. At long times, the strain response of each curve deviates from linearity to different extents, with interfacial creep compliances given by $J_s(t)|_{\tau_0^s = 1\times10^{-5}} \sim t^{0.452}$ and $J_s(t)|_{\tau_0^s = 2\times10^{-6}} \sim t^{0.284}$ respectively. This power-law creep response in time cannot be described by any simple linear viscoelastic model. The Voigt element shown in Figure 4.3.1 approaches a steady deformation at long times, and hence the interfacial stress arises solely from the second dashpot (with viscosity $\eta$) that is in series with the Voigt element. A similar asymptotic response can be deduced for any other, more complex arrangement of linear springs and dashpots in parallel. To describe a power-law creep response, a more complex constitutive model containing springpot mechanical elements and incorporating fractional derivatives (Craiem and Magin, 2010) is required.

A detailed examination of the parameter fits obtained from the measured creep

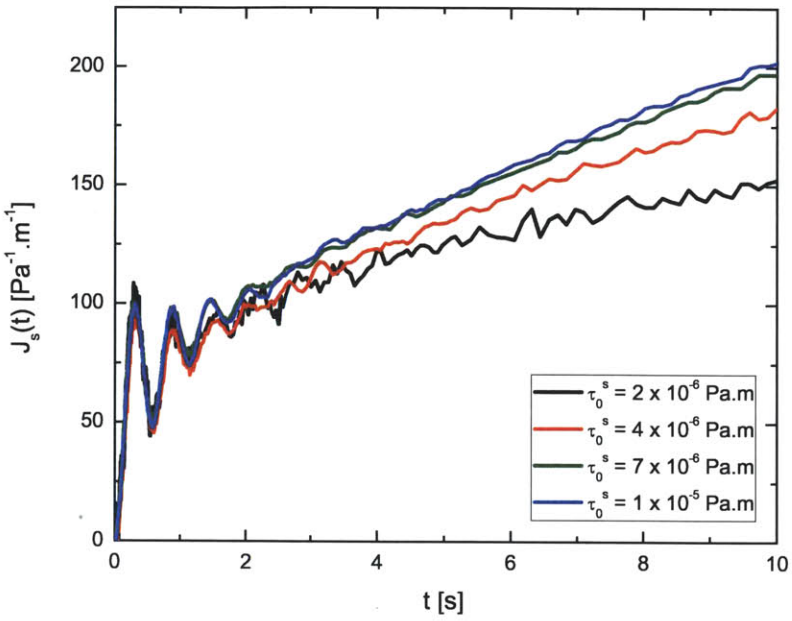


**Figure 4.4.4:** Comparison of interfacial creep compliance $J_s(t) = \gamma(t)/\tau_0$ for different values of interfacial stress $\tau_0$ performed on 50 mg/ml BSA solutions. For an ideal linear material, all curves collapse onto each other. Although the short time creep compliances collapse, deviations can be seen at long times, indicating onset of non-linear behavior.

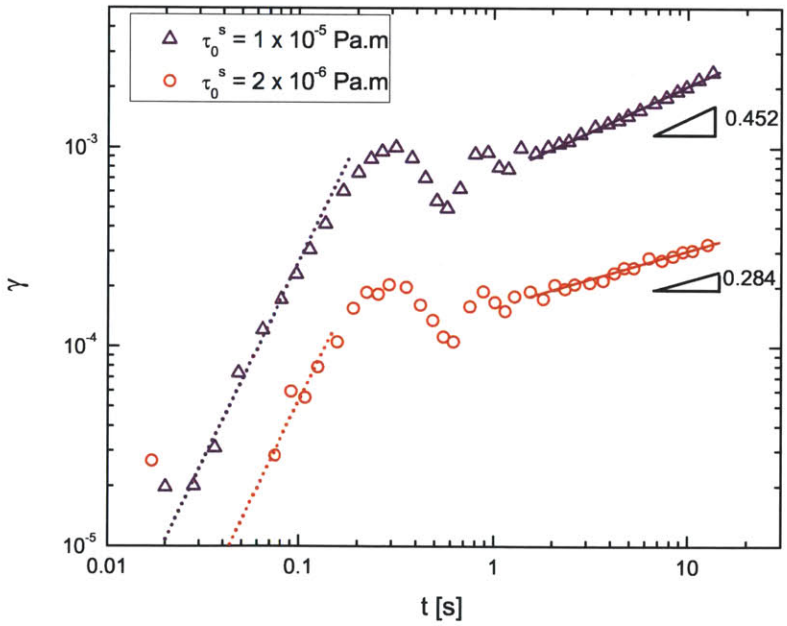


**Figure 4.4.5:** Strain $\gamma(t)$ measured in an interfacial creep experiment on 50 mg/ml BSA solutions at different applied stresses $2 \times 10^{-6} \leq \tau_0 \leq 1 \times 10^{-5}$ Pa m. The solid show a power law fit to the creep data for $2 < t < 10$ s for both experiments. The nonlinearity in the material response at large strains is clearly visible, with both slopes deviating from a slope of unity. The dotted lines show the quadratic response given by $\gamma_0 = [\tau_0/2(I/b_s)]t^2$ short times $t < 0.1$ s .

response in Figures 4.4.3 and 4.4.4 shows that $\mu \ll \eta$. In this limit, the material description of the interface reduces to a linear Maxwell model ($\mu \rightarrow 0$ in Figure 4.3.1 and Equations (4.3.3)- (4.3.7)). This considerably simplifies the evaluation of the linear viscoelastic interfacial moduli and shows that for small strains at least, the interfacial protein layer is modeled well by the simplest linear viscoelastic model.

## 4.5 Protein-Surfactant Mixtures

The bulk shear viscosity of protein-surfactant (BSA-Polysorbate 80) solutions measured using the microfluidic rheometer is shown in Figure 4.5.1a for 50 mg/ml BSA solutions with different concentrations of added surfactant. The behaviour of the protein-surfactant mixtures is Newtonian to shear rates as high as $\dot{\gamma} = 10^4$ s$^{-1}$. Further, for the dilute concentrations of the non-ionic surfactant used in this study, the measured shear viscosity of the mixtures is nearly indistinguishable from surfactant-free BSA. The previous chapter describes how surfactant-free BSA solutions can show yield-like behavior in measurements carried out on standard torsional rheometers due to the formation of a viscoelastic film at the air-water interface. The microfluidic rheometer, on the other hand, measures the true shear viscosity of these solutions in the absence of any air-liquid interfaces. Consequently, the apparent shear thinning measured in the double gap Couette geometry (Figure 3.2.1) is not observed in the results presented in Figure 4.4.3. The range of accessible shear rates in the microfluidic channel is dependent on the geometry of the channel as well as the dynamic range of the pressure transducers. The black lines in Figure 4.5.1a show the operating window of the VROC device, and are determined by the minimum and maximum values of the measurable pressure. A detailed description of the principle and working of the microfluidic viscometer can be found in Pipe et al. (2008). The dependence of the bulk viscosity on concentration for these dilute protein-surfactant solutions is governed by Einstein's expression for suspension viscosity (Harding, 1997; Larson, 1999), and for the dilute concentrations of surfactant used here, the mixed solution viscosity is only slightly higher than the surfactant-free solution. This concentration-dependent vis-

cosity can be modeled using a charged suspension model as discussed in the previous chapter.

On the other hand, the interfacial viscosity measured using the DWR fixture for different surfactant/protein mixtures is so low that it is indistinguishable from the instrument noise floor, as shown in Figure 4.5.1b. The black dashed line shows the minimum shear stress that can be measured by the instrument for the particular case of the DWR fixture. We find this minimum measurable stress value to be approximately a factor of ten greater than the minimum resolvable torque increment $T_{\text{stated}}$ stated by the manufacturer.($T_{\text{stated}} = 10^{-8}$ N m) It is clear from Figure 4.5.1b that for $\dot{\gamma} \leq 3$ s$^{-1}$, the measured interfacial stress of the BSA-surfactant mixtures is in the range of the noise floor of the instrument, indicating that the addition of surfactant markedly decreases the viscosity of interfacial viscoelastic layer.

Grigoriev et al. (2006) report that for the surfactant concentration ranges used in this study, the interfacial viscosity of Tween 80$^{\text{TM}}$ is $\eta_s \approx 10^{-5}$ Pa s m. Computing the stress from this value of viscosity and comparing it with the minimum stress limit shown in Figure 4.5.1b, it is clear that this viscosity is too small to be measured by the DWR used in this study for $\dot{\gamma} < 1$ s$^{-1}$. At higher shear rates, an interfacial torque contribution from the polysorbate surfactant should be measurable, but additional contributions from inertial effects in the subphase become increasingly dominant. It can be seen from Figure 4.5.1b that at higher shear rates the measured shear stress for all of the surfactant-BSA mixtures superpose and all follow a power law of the form $\tau_s \sim \dot{\gamma}^{1.5}$. The fact that the curves remain unchanged by the relatively large variation in surfactant concentration (0.01-2 wt.%) strongly suggests that this pronounced power law response arises from an inertially-induced secondary flow of Taylor-Dean type in the sub-phase (similar power-law corrections for fluid inertia are observed in cylindrical geometries on conventional bulk rheometers, see for example the discussion in Macosko (1994)). An appropriate Reynolds number can be defined for the flow induced by the DWR fixture to be $Re_s = \rho R\dot{\gamma}a/F_\gamma\mu_{\text{sub}}$ where $\rho$ is the density of the sub-phase, $R$ is the radius of the ring, $\dot{\gamma}$ is the applied shear rate, $a$ is the thickness of the ring, and $\mu_{\text{sub}}$ is the dynamic viscosity of the (Newtonian)

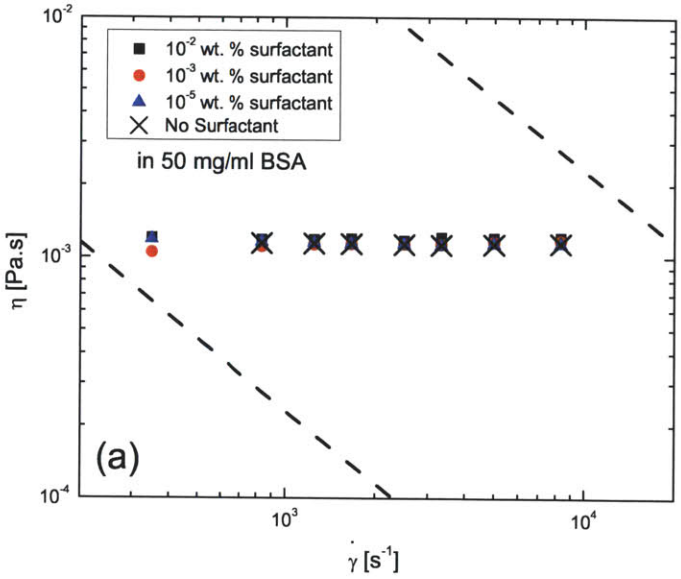


(a) Interface-free VROC measurements.

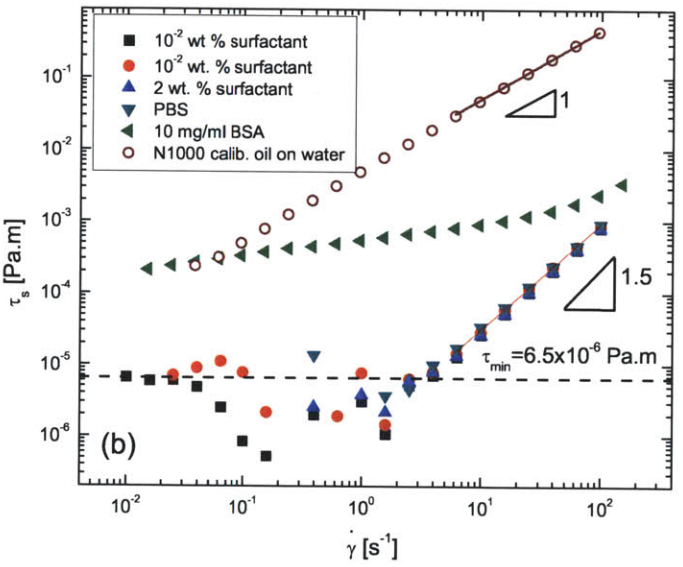


(b) Steady shear experiments using the DWR.

**Figure 4.5.1:** (a) Steady shear viscosity of 50 mg/ml BSA solutions with different concentrations of added surfactant measured in the interface-free microfluidic rheometer. The addition of surfactant at these concentrations makes no noticeable difference to the shear rheology of the BSA solutions in the absence of interfacial effects. (b) Interfacial steady shear viscosity measurements on 50 mg/ml BSA solutions containing different concentrations of added surfactants. The black dashed line shows the measurement limit of the instrument, and anything below this limit is indistinguishable from the noise floor. All solutions exhibit a power-law dependence of interfacial viscosity $\eta_s$ on strain rate $\dot{\gamma}$, with $\eta_s \sim \dot{\gamma}^{1.5}$. This power law arises from an inertial artifact. Also shown, in hollow symbols, is the interfacial viscosity of a thin layer of N1000 Newtonian calibration oil on water. As expected for Newtonian liquids, $\tau_s \sim \dot{\gamma}$

sub-phase. Using this definition for the Reynolds number, it is found that for all the protein-surfactant mixtures, as well as the pure buffer (PBS), $Re_s$ is greater than unity and secondary flows are not entirely unexpected. A detailed computation of the resulting toroidal flow in the sub-phase is beyond the scope of this thesis, but the resulting inertial contribution to the interfacial stress can be extracted from the data in Figure 4.4.3b and is described by the empirical relationship $\tau_s = 1.04 \times 10^{-6}\dot{\gamma}^{1.5}$ (with stress in Pa m and shear rate in $s^{-1}$). Also shown for comparison in this figure (hollow circles) is the interfacial shear stress as a function of shear rate for an ideal Newtonian viscous interface—which can be realized by floating a thin layer of Newtonian calibration oil (N1000, Cannon Instrument Company) carefully atop the PBS subphase. For this viscous interface, the desired condition of $Bo_s \gg 1$ is achieved and the inertial contribution from the sub-phase to the torque is now negligible so that the measured stress increases linearly with imposed shear rate, as expected for a viscous Newtonian interface in the absence of inertial corrections.

Baravian and Quemada (1998) have emphasized the significance of the periodic oscillations seen at short times in creep experiments. The presence of oscillations in creep experiments performed on a controlled-stress rheometer necessarily implies the presence of elasticity whereas purely viscous materials do not give rise to creep ringing. We emphasize that the same holds true for interfacial creep-ringing experiments as well and oscillations are visible if, and only if, interfacial elasticity is present and the system is under-damped, as described in the previous section.

This observation is underscored by the data presented in Figure 4.5.2, which shows creep experiments performed on 50 mg/ml BSA with different concentrations of added surfactant. For the two highest concentrations of surfactant ($10^{-2}$ wt.% and $10^{-3}$ wt.%), creep ringing is completely suppressed indicating that the interface between the air and the aqueous subphase does not exhibit any measurable elasticity. The strain response is exactly that of a purely viscous interface and is described by the expression $\gamma(t) = (\tau_0 b_s/2I)t^2 + O(t^3)$. The quadratic fit to the short time response of surfactant-free 50 mg/ml BSA shown earlier in Figure 4.4.1 is re-plotted here as a blue dashed line. Since the strain at short times is independent of the interfacial

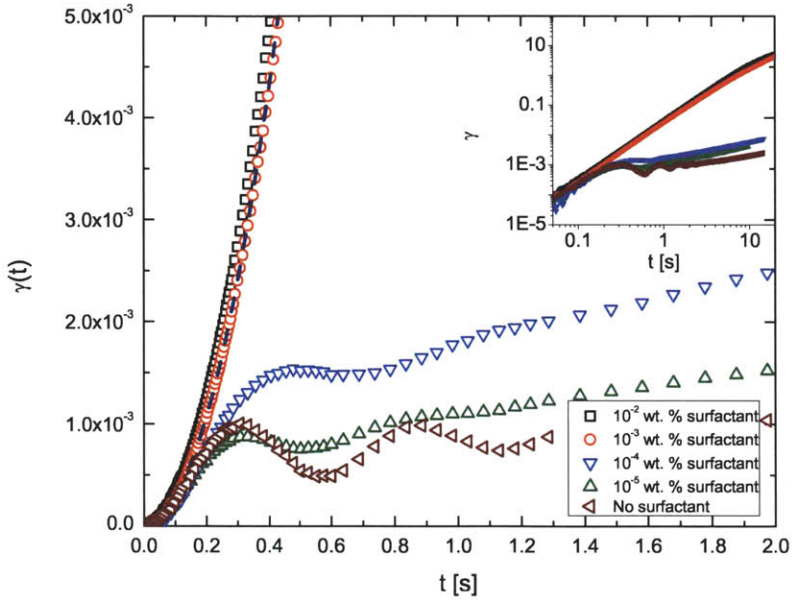


**Figure 4.5.2:** Comparison of interfacial creep ringing experiments performed on 50 mg/ml BSA solutions with different concentrations of added surfactant. Creep ringing is absent for surfactant concentrations $c = 10^{-2}$ wt.% and $c = 10^{-3}$ wt.%. The black dashed line is the expression given by the short time response equation, $\gamma(t) = (\tau_0 b/2I)t^2$ which is also the quadratic fit from the inset of Figure 4.4.1. The short time response is independent of surface elasticity and the same for all samples.

rheology, the quadratic fit from Figure 4.4.1 is unchanged, and accurately describes the data shown in Figure 4.5.2 for $c_{\text{surf}} = 10^{-2}$ wt.% and $c_{\text{surf}} = 10^{-3}$ wt.%.

Creep ringing is visible for the lower surfactant concentrations of $c_{\text{surf}} = 10^{-4}$ wt.% and $c_{\text{surf}} = 10^{-5}$ wt.%. It is evident that the change in surface viscoelastic properties happens very rapidly over a narrow surfactant concentration range ($10^{-4} < c_{\text{surf}} < 10^{-5}$ wt.%). As before, the values of the interfacial storage and loss moduli for the different mixtures can be estimated using Equation (4.3.8). From this we determine values of $G_s'(c_{\text{surf}} = 10^{-4}\text{ wt.\%}) = 0.015$ Pa m and $G_s'(c_{\text{surf}} = 10^{-4}\text{ wt.\%}) = 0.021$ Pa m respectively.

To independently check these values extracted from creep ringing, small amplitude oscillatory time sweeps with the strain amplitude held fixed at $\gamma_0 = 1\%$ for $c_{\text{surf}} = 10^{-4}$ wt.% and surfactant-free BSA were also performed and are shown in Figure 4.5.3. Care must be taken in performing such measurements due to the temporal dynamics that arise from the competitive adsorption of the two surface-active

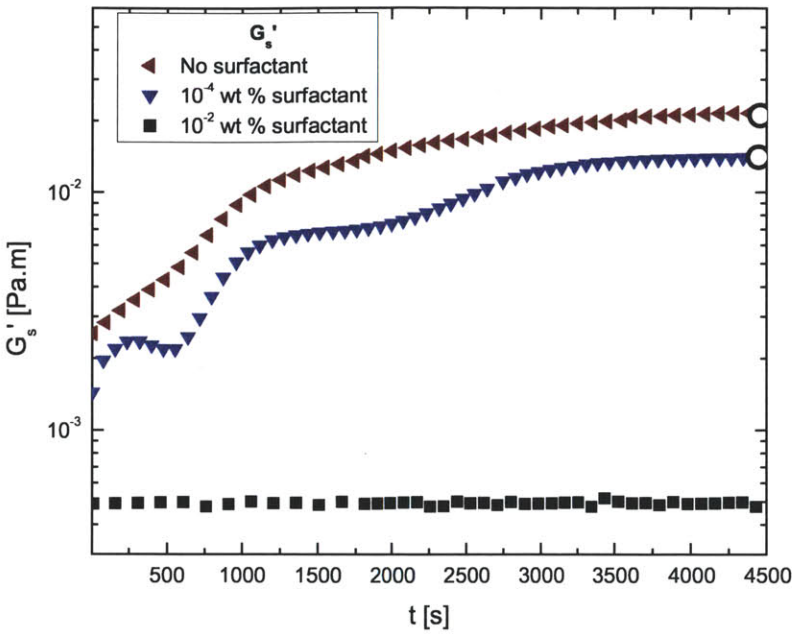


**Figure 4.5.3:** Time sweep of the interfacial storage of 50 mg/ml BSA solutions with different amounts of added surfactants. The circles mark the corresponding value of $G'_s$ obtained from the creep ringing analysis. The values of $G'_s(c_{\text{surf}} = 10^{-4}\ \text{wt.\%}) = 0.015$ Pa m s and $G'_s(\text{no surf})\% = 0.023$ match very well with those obtained from the creep ringing analysis. The mixture with $c_{\text{surf}} = 10^{-2}$ wt.% showed no visible creep ringing, signifying no surface elasticity.

species. The elapsed time between the loading of the sample and the initiation of the interfacial SAOS tests shown in Figure 4.5.3 is less than a minute in each case. For the protein/surfactant mixtures, similar steady state values were reached in successive measurements, but the transient approach to the steady state shows substantial variation in each test. Nonetheless, the value of the storage modulus estimated from the creep ringing in Figure 4.5.2, ($G''_s(c_{\text{surf}} = 10^{-4}\ \text{wt.\%}) = 0.015$ Pa m) is in close agreement with the steady state value of the time sweep, shown in Figure 4.5.3 ($G'_s = 0.014$ Pa m).

Proteins are macromolecular organic molecules consisting of amino acids and contain both hydrophobic and hydrophilic moieties randomly distributed within their primary structure (Mobius and Miller, 1998; Kotsmar et al., 2009). The surface topography and location of the hydrophobic and hydrophilic moieties determine the amphiphilic character of a protein and consequently its surface activity. When proteins adsorb at the air/water interface, in addition to conformational intra-molecular

changes within the proteins (Kotsmar et al., 2009; Cascão Pereira et al., 2003; Song and Damodaran, 1987), the intermolecular protein-protein interactions result in a two-dimensional network structure formation beyond a certain critical concentration (Mobius and Miller, 1998). The viscoelasticity of the interfacial layers manifested in creep ringing and SAOS experiments discussed earlier in Figures 4.4.1- 4.4.5 is a measure of the response of the microstructure thus formed to imposed deformations.

Due to conformational constraints and improper packing, optimal orientation of these hydrophobic and hydrophilic groups at the interface is sometimes prevented and proteins do not reduce the interfacial tension as dramatically as low molecular weight surfactants which can align and organize themselves at the interface more rapidly and optimally (Krägel et al., 1999; Mobius and Miller, 1998; Kotsmar et al., 2009; Morris and Gunning, 2008). It should be noted, however, that the presence of proteins imparts a substantially higher interfacial elasticity and viscosity than the corresponding low molecular weight surfactants. The higher interfacial viscoelasticity of the surfactant-free BSA solutions is seen in both interfacial measurements as well as in the apparent yielding behavior observed in bulk measurements, as discussed previously, due to the extra contribution to the measured torque from the solid-like interfacial films formed at the liquid/air interface.

The addition of surfactants can modify the microstructure, equilibrium and dynamic adsorption values, and the rheological characteristics of the interfacial layers (Murray, 2010; Krägel et al., 1999; Kotsmar et al., 2009; Maldonado-Valderrama and Patino, 2010). The absence of creep ringing and markedly diminished interfacial viscoelasticity of the BSA/Polysorbate 80 mixtures shows that the addition of surfactant disrupts the structure formed by this globular protein at the interface.

Specific interactions between individual proteins and surfactants, their surface and bulk concentrations as well as protein hydrophobicity and conformation are some of the factors that influence the structure and rheology of interfacial layers (Krägel et al., 1999; Kotsmar et al., 2009; Maldonado-Valderrama and Patino, 2010). The adsorption characteristics and dynamical properties of the mixed-interface are quite different from those of the individual components, and are understood only on a phenomeno-

logical level. Furthermore, the interactions, conformational changes and structure induced in the mixed protein/surfactant system at the interface are also quite different from those in the bulk. Studies of the microstructure at the interface using Brewster Angle Microscopy or Fluorescence microscopy (Rodríguez Patino et al., 2008; Lipp et al., 1997; Rampon et al., 2003) or by evaluating local dynamics using micro-rheology reveal the presence of considerable interfacial phase separation with localized surfactant-rich and protein-rich regions (Murray, 2010; Murray and Dickinson, 1996; Pugnaloni et al., 2004). Several studies show that the interconnected network formed by globular proteins can be disrupted by the addition of surfactants through *orogenic displacement* as discussed in a recent review by Morris and Gunning (2008). The surfactant molecules that adsorb at the pre-existing protein interface begin to self-assemble into small domains, that grow in size with time and eventually disrupt the protein network. The two-dimensional microstructure created at the air/liquid interface evolves as phase separation or orogenic displacement occurs and additional conformational changes slowly take place within the protein. Therefore, the temporal evolution of the physical properties of such an interface—such as the measurements presented in Figure 4.5.3—provides a very rich and diverse range of observations. Additional time–dependent studies of transient surface microstructure and protein structure are required to understand and correlate these observations with the changes that occur at the scale of the individual domains in the interfacial layer.

The variability and complexity in the transient interfacial rheological properties of the mixed interface that arise due to heterogeneity at the interface are caused by the thermodynamics and adsorption kinetics of the constituent surfactants and proteins. The equation of state of surfactant-protein mixtures that relates excess surface pressure at the interface to protein and surfactant concentrations, and effective interactions between them (Miller and Liggieri, 2009; Kotsmar et al., 2009; Miller et al., 2000b) looks qualitatively similar to the Flory-Huggins equation of state used to model polymer solutions and blends (Flory, 1953; Rubinstein and Colby, 2003). Non-ionic surfactants like Tween 20$^{TM}$ or Tween 80$^{TM}$ are probably more amenable

for treatment by this simplified model, because ionic surfactants can interact strongly with the protein forming supramolecular complexes (Krägel et al., 2008). Even if the bulk concentrations of the surfactants and proteins are quite low, the species at the interface are close-packed, and an independent measure of interfacial concentrations is required to correlate the reported experimental response to theoretical models, and would be necessary for going beyond the phenomenological description of interfacial rheology of mixed systems.

The apparent bulk yield stress of the BSA solutions is also influenced by the addition of low molecular weight surfactants. The bulk viscosity of 50 mg/ml BSA solutions with different concentrations of added surfactant, is shown in Figure 4.5.4. The dashed line estimates the minimum measurable viscosity for the combination of the double gap Couette geometry and the controlled stress rheometer used in this study. The relationship between the minimum measurable viscosity and minimum shear rate is calculated in the same way as outlined previously, with the same value of $T_{\min}$.

With the addition of even a relatively small amount of Polysorbate 80 ($10^{-5}$ wt.%), to the 50 mg/ml BSA solution, the apparent bulk yield stress is lowered considerably and, for higher concentrations of surfactant, the shear thinning and the apparent yielding are nearly eliminated entirely. Again, this indicates that the mobile surfactant molecules compete with the BSA molecules for adsorption at the interface. Essentially, the last term in Equation (3.6.3) becomes negligible in comparison with the bulk viscosity term, and therefore the reported viscosity is simply the rate-independent sub-phase viscosity.

Grigoriev et al. (2006) have characterized the surface tension, thickness, refractive index and interfacial viscosity of mixed adsorbed layers of BSA/Tween 80$^{\text{TM}}$, for $10^{-7}$ M BSA ($\approx 6.7 \times 10^{-3}$ mg/ml or $\approx 0.67 \times 10^{-3}$ wt.%) and varying surfactant concentrations. They determined that above a surfactant concentration of $5 \times 10^{-6}$ M Tween 80$^{\text{TM}}$ ($\approx 6.6 \times 10^{-3}$ mg/ml), the network structure formed by BSA at the interface is completely disrupted, and the resulting interfacial properties are quite similar to the properties of an interface comprising of pure Tween 80$^{\text{TM}}$. It must be

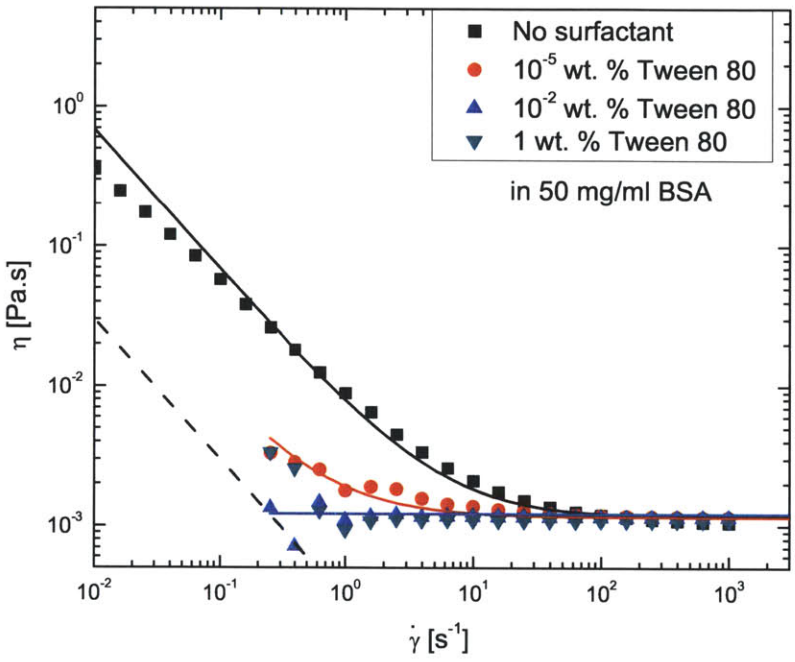


**Figure 4.5.4:** Bulk steady shear viscosity measurements performed on 50 mg/ml BSA solutions with different concentrations of added surfactants. The black line shows the minimum viscosity that is distinguishable from the noise floor for the double gap Couette geometry used in this study on the ARG2. It can be seen that the addition of surfactant dramatically reduces apparent shear thinning and yield-like behavior in the interfacial viscosity, even for relatively small quantities of surfactant ($10^{-5}$ wt.%).

noted that the average value of critical micelle concentration (CMC) estimated by Grigoriev et al. (2006), based on their measurements and literature values, is $2 \times 10^{-5}$ M. A wide range of surfactant properties like viscosity, conductivity, surface tension, osmotic pressure, etc. show a clear transition above the CMC, and similarly for concentrations above the CMC, the effect of added surfactant dominates the interfacial properties (Goddard and Ananthapadmanabhan, 1993). It is found that the steep drop in interfacial elasticity as a function of surfactant concentration as documented through the creep ringing experiments pursued in the present study, (*cf.* Figure 4.4.1) corresponds to a surfactant concentration ($c_{\text{surf}} \sim 10^{-3}$ wt.%) that is close to the CMC values reported for Tween 80$^{\text{TM}}$ by Grigoriev et al. (2006). However it is also noted that due to the interaction with other surface-active species, both in the bulk and at the surface, the critical concentration above which surfactant properties dominate the interfacial behavior of the mixture can be above or below the CMC.

The reduction in the apparent yield-like behavior on adding surfactant to the bovine serum albumin solutions indicates that the network structure formed by BSA molecules adsorbed at the liquid/air interface is progressively disrupted by the addition of the surfactant. A similar reduction in bulk viscosity has been observed by Patapoff and Esue (2009). Surfactants, due to their simpler structure and smaller size, are effectively more surface active than proteins, as described earlier, and this is revealed in the studies of adsorption isotherms as well as adsorption kinetics of surfactants in the mixed systems (Mobius and Miller, 1998; Goddard and Ananthapadmanabhan, 1993).

## 4.6 Conclusion

In this chapter, it has first been demonstrated using the DWR fixture how the viscoelasticity of an adsorbed protein interface, coupled with the finite instrument inertia of a controlled-stress instrument, can result in a damped sinusoidal strain response during interfacial creep experiments. Interfacial creep-ringing in two dimensions is shown to be analogous to its bulk counterpart, and analysis of the data presented

here indicates that this free oscillatory motion can provide a quick and accurate measurement of the interfacial viscoelastic moduli. Moreover, this technique is especially useful in extending the range of frequencies at which measurements can be performed, and measurement points where inertial effects would ordinarily overwhelm the oscillatory viscous flow in regular frequency/strain sweeps can be accessed.

Because interfacial creep-ringing is inherently connected with the presence of an interfacial viscoelastic layer, the creep-ringing technique provides an easy way of assessing the effect of adding different concentrations of surfactants to a globular protein solution such as BSA. For concentrations of $c_{\text{surf}} = 10^{-2}$ wt.% and $c_{\text{surf}} = 10^{-3}$ wt.%, all visible creep ringing was found to be completely eliminated (see Figure 4.5.2). This over-damped response indicates that the mobile surfactant molecules compete with the protein molecules for adsorption at the interface and are preferentially adsorbed. Since the low molecular weight surfactant is purely viscous and lacks measurable elasticity, no interfacial ringing is visible, with a quadratic strain response at short times, in agreement with Equation (4.2.3). It is also noted from the creep-ringing experiments that the change in magnitude of viscoelastic moduli is a very sharp function of surfactant concentration over a narrow concentration range, indicating that there is not only displacement of the protein from the interface, but also disruption of the network structure formed between the protein molecules at the interface above certain critical concentration. This is in accordance with other recent findings in literature (Dickinson and Hong, 1994; Miller et al., 2000b which have reported a sharp reduction of surface shear viscosity, even though a considerable amount of protein remains adsorbed at the interface. The drop in viscoelastic moduli is likely to be a combination of displacement of protein molecules at the interface, as well as the disruption of the inter-molecular network structure formed by the partially-unfolded protein molecules that form the interfacial layer (Dickinson, 1992b).

For lower concentrations of surfactant, interfacial creep-ringing is still observed and an estimate of the progressive reduction in the storage and loss modulus can be made using the procedures described in this paper. The complex transient response in measurements of the effective interfacial properties involving surfactant-

protein mixtures reported by earlier researchers was also encountered in this study (see Figure 4.5.3). The irreversibility of the adsorption, the presence of heterogeneous domains and significant interfacial phase separation at the interface and the sensitivity of the structure of the interfacial layer to the adsorption history add to the complications involved in interfacial rheology measurements (Murray, 2010; Murray and Dickinson, 1996; Dominique Langevin, 2009). The DWR ring fixture provides a method for readily extracting an overall or effective viscoelastic property of the interface as it evolves. Microrheological techniques (Dhar et al., 2010; Prasad et al., 2006) combined with Brewster angle microscopy (Lipp et al., 1997; Morris and Gunning, 2008) will be needed to probe additional properties of these individual domains.

Our measurements show that even a relatively small amount of the polysorbate surfactant ($c_{\text{surf}} > 10^{-5}$ wt.%) suppresses the apparent bulk yield stress and shear thinning exhibited by surfactant-free BSA solutions (see Figure 3.2.1, pp. 50), further emphasizing the profound influence that the interface can have on bulk rheometry. This observation provides further support for the central conclusions of the previous chapter, that the apparent bulk yield stress exhibited by globular protein solutions in steady shear experiments on a torsional rheometer in fact arises as a result of interfacial adsorption, and not out of long-ranging weak colloidal structures as some other studies have suggested (Matsumoto and Chiba, 1990; Ikeda and Nishinari, 2000, 2001a).

The interfacial rheological properties of proteins and surfactant mixtures are often studied using a number of different techniques to quantify the viscosity and elasticity of the interfacial layer, as these affect properties like foam and emulsion stability or mass transfer between fluids (Miller and Liggieri, 2009; Murray and Dickinson, 1996; Mobius and Miller, 1998). But the actual use and processing of food products, physiological fluids like blood (Merrill, 1969), saliva (Waterman et al., 1988), synovial fluid and their synthetic replacements (Oates et al., 2006), cosmetics (Barry and Warburton, 1968; Laba, 1993), *etc.* requires an understanding of both their bulk and interfacial viscoelasticity. Such studies are often pursued independently of each other; however, in this chapter, we show that the apparent bulk rheological response can

itself change if surface-active molecules form "strong" viscoelastic interfacial layer at the liquid/air interface. In this case, the extra stress contribution to the effective bulk properties originates from the stiff interfacial network formed by close-packed protein molecules. Indeed, solutions of bovine serum albumin, ovalbumins and other globular proteins (Matsumoto and Chiba, 1990; Ikeda and Nishinari, 2000; Regev et al., 2010; Ikeda and Nishinari, 2001a), as well as acacia gum (Sanchez et al., 2002), and monoclonal antibody solutions (Patapoff and Esue, 2009) are all examples of systems that result in strong interfacial networks because their bulk rheological response measured on conventional torsional rheometers shows an apparent yield stress that arises from a contribution of this adsorbed protein layer. The quantitative decomposition of the interfacial and sub-phase contributions can be carried out using the additive model proposed by Sharma et al. (2011), or more pragmatically, the interfacial contribution can be simply minimized by the addition of low molecular weight mobile surfactants to these protein solutions. As has been shown in the present chapter, the concentration of non-ionic surfactant required to suppress protein adsorption and network formation at the interface is often so small that it does not affect the bulk properties of the original protein solution (see Figure 3.2.2), at least in the present polysorbate-BSA system. However creep experiments with the interfacial DWR fixture, coupled with the creep ringing analysis described here, provides a simple and rapid way of quantifying the pronounced changes in the protein/surfactant network structure formed at the liquid/air interface.

# Chapter 5

# Conclusion

This thesis has investigated the bulk as well as the surface rheology of globular proteins solutions using a model globular protein (BSA). The measurements show unequivocally that such solutions have a tendency to form a rigid viscoelastic film at the interface. We have discussed how these films can lead to viscoelastically-stabilized foams and emulsions, which play an important role in various applications and industries.

Chapter 3 describes in detail the viscoelastic properties of the adsorbed layer of protein formed at the air-water interface. It was observed that the interfacial film thus formed significantly influences the bulk rheology, and not accounting for these effects correctly can lead to misinterpretations of the bulk data. We show that globular protein solutions show strong shear thinning in bulk viscometric measurements even at low concentrations (see Figure 3.2.1) and the nature of the viscoelastic layer also shows a concentration dependence, with longer relaxation times for higher concentrations (see Figure 3.4.3). We also show how the bulk response can be modeled based on the interfacial response and knowledge of the specific bulk geometry used (see Equations (3.6.3) and (3.6.4), pp. 66).

Due to most real fluids being mixtures of proteins and other competing surface active molecules (for example blood (Merrill, 1969; Ariola et al., 2006)), we also examined in Chapter 4 the surface rheology of protein-surfactant mixtures. A new technique, interfacial creep ringing, was introduced to rapidly estimate the viscoelastic

storage and loss moduli (see Figure 4.4.2). It was also shown how this technique can be used to quantify the progressive, systematic changes that occur at the interface upon increasing the bulk concentration of a competing surfactant (Polysorbate 80) in the protein solution (see Figure 4.5.2) of the mixed interfaces. As discussed in Chapter 4 and the cited literature, the dynamics of these surfaces can be complex and sensitive to various initial conditions and parameters.

One of the questions that remains unanswered in this study is the possibility of wall slip between the interfacial layer of adsorbed protein and the double wall ring fixture. If slip is present, the rheological measurements would not represent a material property, due to the possibility of varying amounts of slip during the experiments. The good match between experiment and theory in the experiments presented here (see Figure 3.6.2) make the possibility of the presence of an arbitrary slip in this study unlikely, although this argument is circumstantial. One possible method to check definitively for the presence of slip is to position the ring at different gap heights once the ring has been placed such that it just touches the interface. Pushing the ring deeper into the interface will increase the normal force on the ring, and hence decrease slip, if slip is indeed present. If different gap heights give significantly different values of interfacial viscosity and interfacial viscoelastic moduli, it is an indicator of the presence of slip.

One avenue of future work would be to image these interfaces using the technique of Brewster Angle Microscopy (Lipp et al., 1997; Miller et al., 2000a). Brewster angle measurements exploit the polarization state of the light reflected from an interface, which in turn depends on the refractive index $n$ of the reflecting surface or medium (Castada, 2010). Figure 5.0.1, reproduced from a paper by Leiske et al. (2010), shows examples of the images produced by Brewster angle microscopy techniques, for human and animal Meibomian lipids, a lipid whose interfacial properties play a key role in the stability of tear films. These images are usually of high quality, with a spatial resolution of around 1 $\mu$m (Meunier, 2000). Direct observation the interfaces, especially in the case of protein-surfactant mixtures, could shed much light on the competition for adsorption at the interface and the dynamics of mixed systems in

general (Patino et al., 2007; Miller et al., 2008).

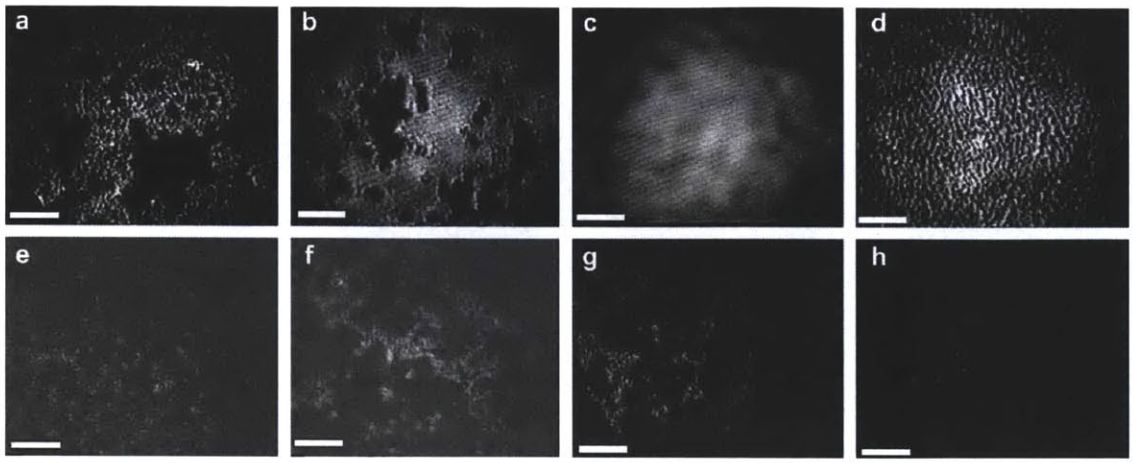


**Figure 5.0.1:** Examples of Brewster angle microscopy images of human and animal Meibomian lipids, adopted from Leiske et al. (2010). Scale bar is 250$\mu$m.

Yet another powerful technique would be to use particle-tracking-based microrheology (Ortega et al., 2010; Prasad et al., 2006; Murray, 2010) to investigate the nature of the interfacial phase separation of mixed protein-surfactant layers. These techniques can be readily employed in studying heterogeneous surfaces (Ortega et al., 2010), as is the case in the mixed protein-surfactant solutions. As explained in the conclusion section of Chapter 4 (pp. 99), these mixed solutions tend to form heterogeneous 'islands' at the interface. It can be hypothesized that tracer particles in the viscous surfactant domains are more mobile as compared to the viscoelastic domains of the adsorbed protein, and one would expect very different thermal motion of the particles in the two domains. Furthermore, the local viscoelasticity could lead to anomalous or 'non-Brownian' diffusion of the particles, where the mean square displacement $\langle \Delta r \rangle^2$ does not scale with time $t$ as $\langle \Delta r \rangle^2 \sim t$, but rather as $\langle \Delta r \rangle^2 \sim t^\alpha$ where $0 < \alpha < 1$ (Amblard et al., 1996). Such systems are particularly suited to be described using the fractional calculus, from which many useful quantitative conclusions can be drawn (Sokolov et al., 2002; Metzler and Klafter, 2000). Interestingly, fractional calculus would also be of use in describing the non-linear long time creep response in the experiments presented in this thesis (see the discussion on pp. 87).

The conclusion of Chapter 4 (pp. 99), also alludes to the 'orogenic' displacement

model proposed by Mackie et al. (1999) (also discussed in Morris and Gunning (2008) and the references therein). The difference in mobility or diffusion timescales of the tracer particles between the surfactant domains and viscoelastic protein domains could be exploited to study in more detail the physical process of the displacement of protein molecules by surfactants. Particle tracking microrheology studies of complex interfaces is an emerging field of interest, and Ortega et al. (2010) state in their recent review *"We will highlight that we are far from understanding microrheology results, and we hope that this review will stimulate future works on this subject."*

The author hopes that this thesis has elicited in the reader an interest in the field of the rheology of globular proteins and surface rheology in general. Much work has been done in this field, as is evident from the cited literature herein, but very possibly, much more is yet to come. Such is the nature of science, and as Michael Faraday insightfully pointed out (quoted by Jones, 1870),

> ...learn that which is already known to others, and then by the light and methods which belong to science learn for ourselves and for others; so making a fruitful return to man in the future for that which we have obtained from the men of the past.

# Bibliography

E. Abbot. *Flatland.* Seely and Co., 1884.

A. W. Adamson and A. P. Gast. *Physical Chemistry of Surfaces.* John Wiley & Sons, New York, 6th edition, 1997.

W. Alpers and H. Huhnerfuss. The Damping of ocean waves by surface films. *Journal of Geophysical Research*, 94:6251–6265, 1989.

F. Amblard, A. C. Maggs, B. Yurke, A. Pargellis, and S. Leibler. Subdiffusion and Anomalous Local Viscoelasticity in Actin Networks. *Physical review letters*, 77(21): 4470–4473, Nov. 1996.

H. Ancell. Course of lectures on the physiology of the blood and the other animal fluids. *Lancet*, 1:222, 1839.

F. S. Ariola, A. Krishnan, and E. A. Vogler. Interfacial rheology of blood proteins adsorbed to the aqueous-buffer/air interface. *Biomaterials*, 27(18):3404–12, June 2006.

P. Aussillous and D. Quere. Liquid marbles. *Nature*, 411(June):924–927, 2001.

C. Baravian and D. Quemada. Using instrumental inertia in controlled stress rheometry. *Rheologica Acta*, 37(3):223–233, June 1998.

H. A. Barnes, J. F. Hutton, and K. Walters. *An Introduction to Rheology.* Elsevier Science Publishers, New York, 1989.

B. Barry and B. Warburton. Some rheological aspects of cosmetics. *Journal of the Society of Cosmetic Chemists*, 19:725–744, 1968.

E. C. Bingham. The Rheology of the Blood. V. *The Journal of General Physiology*, 28(6):605–626, 1945.

R. B. Bird, R. C. Armstrong, and O. Hassager. *Dynamics of Polymeric Liquids.* John Wiley & Sons, second edition, 1987.

B. Biswas and D. A. Haydon. The rheology of some interfacial adsorbed films of macromolecules. I. Elastic and creep phenomena. *Proceedings of the Royal Society A: Mathematical, Physical and Engineering Sciences*, 271(1346):296–316, Jan. 1963.

M. A. Bos and T. Van Vliet. Interfacial rheological properties of adsorbed protein layers and surfactants: a review. *Advances in Colloid and Interface Science*, 91(3): 437–71, July 2001.

M. J. Boussinesq. Sur l'existence d'une viscosite' superficielle, dans la mince couche de transition separant un liquide d'une autre fluide contigu. *Annales des Chimie et des Physique*, 29:349–357, 1913a.

M. J. Boussinesq. The application of the formula for surface viscosity to the surface of a slowly falling droplet in the midst of a large unlimited amount of fluid which is at rest and possesses a smaller specific gravity. *Annales des Chimie et des Physique*, 29:357, 1913b.

C. F. Brooks, G. G. Fuller, C. W. Frank, and C. R. Robertson. An interfacial stress rheometer to study rheological transitions in monolayers at the air-water interface. *Langmuir*, 15(7):2450–2459, 1999.

A. Brown, W. Thuman, and J. McBain. The surface viscosity of detergent solutions as a factor in foam stability. *Journal of Colloid Science*, 8:491, 1959.

G. J. Brownsey, T. R. Noel, R. Parker, and S. G. Ring. The glass transition behavior of the globular protein bovine serum albumin. *Biophysical journal*, 85(6):3943–50, Dec. 2003.

D. C. Carter and J. X. Ho. *Structure of Serum Albumin*, pages 153–203. Academic Press, San-Diego, 1994.

L. G. Cascão Pereira, O. Théodoly, H. W. Blanch, and C. J. Radke. Dilatational Rheology of BSA Conformers at the Air/Water Interface. *Langmuir*, 19(6):2349–2356, Mar. 2003.

H. Z. Castada. Brewster Angle Microscopy study of model lung surfactant systems at the air-water and air-physiological buffer interfaces, 2010.

D. T. Chen, E. R. Weeks, J. C. Crocker, M. F. Islam, R. Verma, J. Gruber, A. J. Levine, T. C. Lubensky, and A. G. Yodh. Rheological microscopy: Local mechanical properties from microrheology. *Physical Review Letters*, 90(10):1–4, Mar. 2003.

J. Chen and E. Dickinson. Protein/surfactant interfacial interactions Part 3. Competitive adsorption of protein + surfactant in emulsions. *Colloids and Surfaces A: Physicochemical and Engineering Aspects*, 101(1):77–85, Aug. 1995.

J.-L. Courthaudon, E. Dickinson, and D. Dalgleish. Competitive adsorption of $\beta$-casein and nonionic surfactants in oil-in-water emulsions. *Journal of Colloid and Interface Science*, 145(2):390–395, Sept. 1991a.

J.-L. Courthaudon, E. Dickinson, Y. Matsumura, and D. C. Clark. Competitive adsorption of $\beta$-lactoglobulin + tween 20 at the oil-water interface. *Colloids and Surfaces*, 56:293–300, 1991b.

D. Craiem and R. L. Magin. Fractional order models of viscoelasticity as an alternative in the analysis of red blood cell (RBC) membrane mechanics. *Physical Biology*, 7 (1):13001, Jan. 2010.

J. M. Dealy. Official nomenclature for material functions describing the response of a viscoelastic fluid to various shearing and extensional deformations. *Journal of Rheology*, 28(3):181, 1984.

P. Dhar, Y. Cao, T. M. Fischer, and J. Zasadzinski. Active interfacial shear microrheology of aging protein films. *Physical Review Letters*, 104(1):1–4, Jan. 2010.

E. Dickinson. *Adsorbed Protein Layers in Food Emulsions*, page 25. Kluwer Academic Publishers, Dordrecht, Netherlands, 1992a.

E. Dickinson. Interfacial interactions and the stability of oil-in-water emulsions. *Pure and Applied Chemistry*, 64(11):1721–1724, 1992b.

E. Dickinson. Adsorbed protein layers at fluid interfaces: interactions, structure and surface rheology. *Colloids and Surfaces B: Biointerfaces*, 15(2):161–176, Sept. 1999.

E. Dickinson and S.-T. Hong. Surface coverage of beta-Lactoglobulin at the oil-water interface: Influence of protein heat treatment and various emulsifiers. *Journal of Agricultural and Food Chemistry*, 42(8):1602–1606, Aug. 1994.

D. B. Dingwell. *The Physics of Explosive Volcanic Eruptions.* The Geological Society, Cambridge, U.K, 1998.

Dominique Langevin. *Mixed surfactant - polyelectrolyte layers.* Koninklijke Brill NV, 2009.

J. T. Edsall, H. Edelhoch, R. Lontie, and P. R. Morrison. Light scattering in solutions of serum albumin: Effects of charge and ionic strength. *Journal of the American Chemical Society*, 72(1948):4641–4656, 1950.

D. A. Edwards, H. Brenner, and D. T. Wasan. *Interfacial Transport Processes and Rheology.* Butterworth-Heinemann, Boston, 1991.

R. H. Ewoldt and G. H. McKinley. Creep ringing in rheometry or how to deal with oft-discarded data in step stress tests! *Rheology Bulletin*, 76(1):4–6, 2007.

M. L. Ferrer, R. Duchowicz, B. Carrasco, J. G. de la Torre, and A. U. Acuña. The conformation of serum albumin in solution: a combined phosphorescence depolarization-hydrodynamic modeling study. *Biophysical journal*, 80(5):2422–30, May 2001.

J. D. Ferry. *Viscoelastic Properties of Polymers.* John Wiley & Sons, 1980.

P. J. Flory. *Principles of Polymer Chemistry.* Cornell University Press, 1953.

E. M. Freer, K. S. Yim, G. G. Fuller, and C. J. Radke. Interfacial rheology of globular and flexible proteins at the hexadecane/water interface: Comparison of shear and dilatation deformation. *The Journal of Physical Chemistry B*, 108(12):3835–3844, Mar. 2004a.

E. M. Freer, K. S. Yim, G. G. Fuller, and C. J. Radke. Shear and dilatational relaxation mechanisms of globular and flexible proteins at the hexadecane/water interface. *Langmuir : the ACS journal of surfaces and colloids*, 20(23):10159–67, Dec. 2004b.

A. Gaigalas, J. Hubbard, M. McCurley, and S. Woo. Diffusion of bovine serum albumin in aqueous solutions. *The Journal of Physical Chemistry*, 96(5):2355–2359, 1992.

E. D. Goddard and K. P. Ananthapadmanabhan, editors. *Interactions of Surfactants with Polymers and Proteins.* CRC Press, 1993.

F. Goodrich. The theory of absolute surface shear viscosity II. The rotating disk problem. *Journal of Colloid and Interface Science*, 34(1):36–42, Sept. 1970.

D. E. Graham and M. C. Phillips. Proteins at Liquid Interfaces I. Kinetics of Adsorption and Surface Denaturization. *Colloid and Interface Science*, 70:415–426, 1979.

D. E. Graham and M. C. Phillips. Proteins at Liquid Interfaces V. Shear properties. *Journal of Colloid and Interface Science*, 76(1):240–250, Dec. 1980.

D. O. Grigoriev, S. Derkatch, J. Krägel, and R. Miller. Relationship between structure and rheological properties of mixed BSA/Tween 80 adsorption layers at the air/water interface. *Food Hydrocolloids*, 21:823–830, 2006.

S. E. Harding. The intrinsic viscosity of biological macromolecules. Progress in measurement, interpretation and application to structure in dilute solution. *Progress in biophysics and molecular biology*, 68(2):207–262, 1997.

F. He, G. W. Becker, J. R. Litowski, L. O. Narhi, D. N. Brems, and V. I. Razinkov. High-throughput dynamic light scattering method for measuring viscosity of concentrated protein solutions. *Analytical Biochemistry*, 399(1):141–143, Apr. 2010.

X. M. He and D. C. Carter. Atomic structure and chemistry of human serum albumin. *Nature*, 358:209–215, 1992.

S. Ikeda and K. Nishinari. Intermolecular forces in bovine serum albumin solutions exhibiting solidlike mechanical behaviors. *Biomacromolecules*, 1(4):757–63, Jan. 2000.

S. Ikeda and K. Nishinari. Solid-like mechanical behaviors of ovalbumin aqueous solutions. *International Journal of Biological Macromolecules*, 28(4):315–20, Apr. 2001a.

S. Ikeda and K. Nishinari. On solid-like rheological behaviors of globular protein solutions. *Food Hydrocolloids*, 15:401–406, 2001b.

H. Inoue and T. Matsumoto. Viscoelastic and SAXS studies of the structural transition in concentrated aqueous colloids of ovalbumin and serum albumins. *Journal of Rheology*, 38(4):973, July 1994.

H. Inoue and T. Matsumoto. Viscoelastic characterization of solid-like structure in aqueous colloids of globular proteins. *Colloids and Surfaces A: Physicochemical and Engineering Aspects*, 109:89–96, 1996.

C. Jaupart and S. Vergniolle. The generation and collapse of a foam layer at the roof of a basaltic magma chamber. *Journal of Fluid Mechanics*, 203:347, Apr. 2006.

B. Jones. The Life and Letters of Faraday. 2:402, 1870.

B. Kerwin. Polysorbates 20 and 80 used in the formulation of protein biotherapeutics: structure and degradation pathways. *Journal of Pharmaceutical Sciences*, 97(8): 2924–2935, 2008.

C. S. Kotsmar, V. Pradines, V. S. Alahverdjieva, E. V. Aksenenko, V. B. Fainerman, V. I. Kovalchuk, J. Krägel, M. E. Leser, B. A. Noskov, and R. Miller. Thermodynamics, adsorption kinetics and rheology of mixed protein-surfactant interfacial layers. *Advances in Colloid and Interface Science*, 150(1):41–54, Aug. 2009.

J. Krägel, R. Wüstneck, F. Husband, P. J. Wilde, A. V. Makievski, D. O. Grigoriev, and J. B. Li. Properties of mixed protein/surfactant adsorption layers. *Colloids and Surfaces B: Biointerfaces*, 12(3-6):399–407, Jan. 1999.

J. Krägel, S. R. Derkatch, and R. Miller. Interfacial shear rheology of protein-surfactant layers. *Advances in Colloid and Interface Science*, 144(1-2):38–53, Dec. 2008.

P. K. Kundu and I. M. Cohen. *Fluid Mechanics.* Academic Press, San Diego, second edition, 2002.

D. Laba, editor. *Rheological Properties of Cosmetics and Toiletries.* CRC Press, 1993.

D. Langevin. Influence of interfacial rheology on foam and emulsion properties. *Advances in colloid and interface science*, 88(1-2):209–22, Dec. 2000.

D. Langevin and F. Monroy. Interfacial rheology of polyelectrolytes and polymer monolayers at the airwater interface. *Current Opinion in Colloid & Interface Science*, 15(4):283–293, Aug. 2010.

R. G. Larson. *The Structure and Rheology of Complex Fluids.* Oxford University Press, 1999.

J. Lefebvre. Viscosity of concentrated protein solutions. *Rheologica Acta*, 21:620–625, July 1982.

D. L. Leiske, S. R. Raju, H. A. Ketelson, T. J. Millar, and G. G. Fuller. The interfacial viscoelastic properties and structures of human and animal Meibomian lipids. *Experimental eye research*, 90(5):598–604, May 2010.

A. J. Levine and T. C. Lubensky. One- and two-particle microrheology. *Physical review letters*, 85(8):1774–7, Aug. 2000.

M. M. Lipp, K. Y. Lee, A. Waring, and J. A. Zasadzinski. Fluorescence, polarized fluorescence, and Brewster angle microscopy of palmitic acid and lung surfactant protein B monolayers. *Biophysical Journal*, 72(6):2783–2804, 1997.

J. Liu, M. D. H. Nguyen, J. D. Andya, and S. J. Shire. Reversible self-association increases the viscosity of a concentrated monoclonal antibody in aqueous solution. *Journal of Pharmaceutical Sciences*, 94(9):1928–1940, Sept. 2005.

J. R. Lu, T. J. Su, and J. Penfold. Adsorption of serum albumins at the air/water interface. *Langmuir*, 15(20):6975–6983, Sept. 1999.

A. R. Mackie, A. P. Gunning, P. J. Wilde, and V. J. Morris. Orogenic displacement of protein from the air/water interface by competitive adsorption. *Journal of colloid and interface science*, 210(1):157–166, Feb. 1999.

C. W. Macosko. *Rheology: Principles, Measurements and Applications.* Wiley-VCH, 1994.

J. Maldonado-Valderrama and J. M. R. Patino. Interfacial rheology of protein-surfactant mixtures. *Current Opinion in Colloid & Interface Science*, 15(4):271–282, Aug. 2010.

J. Maldonado-Valderrama, A. Martin-Molina, A. Martin-Rodriguez, M. Cabrerizo-Vilchez, M. Galvez-Ruiz, and D. Langevin. Surface properties and foam stability of protein/surfactant mixtures: Theory and experiment. *Journal of Physical Chemistry C*, 111(6):2715–2723, Feb. 2007.

R. J. Mannheimer and R. S. Schechter. An improved apparatus and analysis for surface rheological measurements. *Journal of Colloid and Interface Science*, 32: 195–211, 1970.

T. Matsumoto and J. Chiba. Rheological and small-angle X-ray scattering investigations on the shape and ordered arrangement of native ovalbumin molecules in aqueous colloids. *Journal of the Chemical Society, Faraday Transactions*, 86(16): 2877, 1990.

T. Matsumoto and H. Inoue. Small angle X-ray scattering and viscoelastic studies of the molecular shape and colloidal structure of bovine and rat serum albumins in aqueous systems. *Chemical Physics*, 178(1-3):591–598, Dec. 1993.

T. Matsumoto and H. Inoue. Colloidal structure and properties of bovine serum globulin aqueous systems using SAXS and rheological measurements. *Chemical Physics*, 207(1):167–172, June 1996.

G. H. McKinley and T. Sridhar. Filament-stretching rheometry of complex fluids. *Annual Review of Fluid Mechanics*, 34(1):375–415, 2002.

D. E. McMillan. A comparison of five methods for obtaining the intrinsic viscosity of bovine serum albumin. *Biopolymers*, 13(7):1367–76, Jan. 1974.

M. Menin and A. A. Giaretta. Predation on foam nests of leptodactyline frogs (Anura: Leptodactylidae) by larvae of Beckeriella niger (Diptera: Ephydridae). *Journal of Zoology*, 261(3):239–243, Nov. 2003.

E. Merrill. Rheology of Blood. *Physiological Reviews*, 49(4), Mar. 1969.

R. Metzler and J. Klafter. The random walk's guide to anomalous diffusion: A fractional dynamics approach. *Physics Reports*, 339:1–77, 2000.

J. Meunier. Why a Brewster angle microscope? *Colloids and Surfaces A: Physicochemical and Engineering Aspects*, 171(1-3):33–40, Oct. 2000.

R. Miller and L. Liggieri, editors. *Interfacial Rheology*. Koninklijke Brill NV, 2009.

R. Miller, V. B. Fainerman, A. V. Makievski, J. Krägel, D. O. Grigoriev, V. N. Kazakov, and O. V. Sinyachenko. Dynamics of protein and mixed protein/surfactant adsorption layers at the water/fluid interface. *Advances in Colloid and Interface Science*, 86(1-2):39–82, May 2000a.

R. Miller, V. B. Fainerman, A. V. Makievski, J. Kragel, and R. Wüstneck. Adsorption characteristics of mixed monolayers of a globular protein and a non-ionic surfactant. *Colloids and Surfaces A: Physicochemical and Engineering Aspects*, 161(1):151–157, Jan. 2000b.

R. Miller, V. S. Alahverdjieva, and V. B. Fainerman. Thermodynamics and rheology of mixed proteinsurfactant adsorption layers. *Soft Matter*, 4(6):1141, 2008.

A. P. Minton and H. Edelhoch. Light scattering of bovine serum albumin solutions: Extension of the hard particle model to allow for electrostatic repulsion. *Biopolymers*, 21(2):451–458, Feb. 1982.

D. Mobius and R. Miller. *Proteins at Liquid Interfaces.* Elsevier, Amsterdam, 1998.

J. Morgan and H. Woodward. The weight of a falling drop and the laws of Tate. XI. The drop weight and surface tension of blood serum. *Journal of the American Chemical Society*, 35(9):1249–1262, 1913.

V. J. Morris and A. P. Gunning. Microscopy, microstructure and displacement of proteins from interfaces: Implications for food quality and digestion. *Soft Matter*, 4:943–953, 2008.

B. S. Murray. Interfacial rheology of food emulsifiers and proteins. *Current Opinion in Colloid & Interface Science*, 7(5-6):426–431, Nov. 2002.

B. S. Murray. Stabilization of bubbles and foams. *Current Opinion in Colloid & Interface Science*, 12(4-5):232–241, Oct. 2007.

B. S. Murray. Rheological properties of protein films. *Current Opinion in Colloid & Interface Science*, 16:27–35, June 2010.

B. S. Murray and E. Dickinson. Interfacial rheology and the dynamic properties of adsorbed films of food proteins and surfactants. *Food Science and Technology International, Tokyo*, 2(3):131–145, 1996.

S. Y. Nishimura, G. M. Magana, A. H. Ketelson, and G. G. Fuller. Effect of lysozyme adsorption on the interfacial rheology of DPPC and cholesteryl myristate films. *Langmuir*, 24(11):728–733, 2008.

K. M. N. Oates, W. E. Krause, R. L. Jones, and R. H. Colby. Rheopexy of synovial fluid and protein aggregation. *Journal of the Royal Society, Interface / the Royal Society*, 3(6):167–74, Feb. 2006.

S.-G. Oh and J. C. Slattery. Disk and biconical interfacial viscometers. *Journal of Colloid and Interface Science*, 67(3):516–525, Dec. 1978.

F. Ortega, H. Ritacco, and R. G. Rubio. Interfacial microrheology: Particle tracking and related techniques. *Current Opinion in Colloid & Interface Science*, 15(4): 237–245, Aug. 2010.

M.-S. Park, J.-W. Chung, Y.-K. Kim, S.-C. Chung, and H.-S. Kho. Viscosity and wettability of animal mucin solutions and human saliva. *Oral Diseases*, 13(2): 181–1866, Mar. 2007.

T. Patapoff and O. Esue. Polysorbate 20 prevents the precipitation of a monoclonal antibody during shear. *Pharmaceutical Development and Technology*, 14(6):659–664, 2009.

J. M. R. Patino, C. C. Sánchez, M. C. Fernández, and M. R. R. Niño. Protein displacement by monoglyceride at the air-water interface evaluated by surface shear rheology combined with Brewster angle microscopy. *The Journal of Physical Chemistry B*, 111(28):8305–13, July 2007.

T. Peters. *All About Albumin: Biochemistry, Genetics, and Medical Applications.* Academic Press, New York, 1996.

C. J. S. Petrie. *Elongational Flows.* Pitman publishers, 1979.

C. J. S. Petrie. One hundred years of extensional flow. *Journal of Non-Newtonian Fluid Mechanics*, 137(1-3):1–14, Aug. 2006.

C. Picart, J.-M. Piau, H. Galliard, and P. Carpentier. Human blood shear yield stress and its hematocrit dependence. *Journal of Rheology*, 42(1):1–12, 1998.

C. J. Pipe, T. S. Majmudar, and G. H. McKinley. High shear rate viscometry. *Rheologica Acta*, 47(5-6):621–642, Apr. 2008.

J. Plateau. Experiemental and theoretical researches into the figures of equilibrium of a liquid mass without weight VIII. Researches into the causes upon which the easy development and the persistence of liquid films depend .— On the superficial tension of liquids. *Philosophical Magazine Series*, 38:445–455, 1869.

V. Prasad, S. Koehler, and E. Weeks. Two-particle microrheology of quasi-2D viscous systems. *Physical Review Letters*, 97(17):1–4, Oct. 2006.

G. B. Proctor, S. Hamdan, G. H. Carpenter, and P. Wilde. A statherin and calcium enriched layer at the air interface of human parotid saliva. *The Biochemical journal*, 389(1):111–6, July 2005.

L. A. Pugnaloni, E. Dickinson, R. Ettelaie, A. R. Mackie, and P. J. Wilde. Competitive adsorption of proteins and low-molecular-weight surfactants: Computer simulation and microscopic imaging. *Advances in Colloid and Interface Science*, 107(1):27–49, Jan. 2004.

D. Quemada and C. Berli. Energy of interaction in colloids and its implications in rheological modeling. *Advances in Colloid and Interface Science*, 98(1):51–85, May 2002.

V. Rampon, C. Genot, A. Riaublanc, M. Anton, M. A. V. Axelos, and D. J. McClements. Front-face fluorescence spectroscopy study of globular proteins in emulsions: Displacement of BSA by a nonionic surfactant. *Journal of Agricultural and Food Chemistry*, 51(9):2482–2489, 2003.

O. Regev, S. Vandebril, E. Zussman, and C. Clasen. The role of interfacial viscoelasticity in the stabilization of an electrospun jet. *Polymer*, 51(12):2611–2620, May 2010.

M. Reiner. *Lectures on Theoretical Rheology.* North-Holland Publishing Company, Amsterdam, third edition, 1960.

S. Reynaert, C. F. Brooks, P. Moldenaers, J. Vermant, and G. G. Fuller. Analysis of the magnetic rod interfacial stress rheometer. *Journal of Rheology*, 52(1):261–285, 2008.

J. L. Richards. Viscosity and the shapes of macromolecules: A physical chemistry experiment using molecular-level models in the interpretation of macroscopic data obtained from simple measurements. *Journal of Chemical Education*, 70(8):685, Aug. 1993.

L. E. Rodd, T. P. Scott, J. J. Cooper-White, and G. H. McKinley. Capillary break-up rheometry of low-viscosity elastic fluids. *Applied Rheology*, 15(1):12–27, 2005.

J. M. Rodríguez Patino, C. Carrera Sánchez, and M. R. Rodríguez Niño. Implications of interfacial characteristics of food foaming agents in foam formulations. *Advances in Colloid and Interface Science*, 140(2):95–113, Aug. 2008.

M. Rubinstein and R. H. Colby. *Polymer Physics.* Oxford Univsersity Press, 2003.

W. B. Russel, D. A. Saville, and W. R. Schowalter. *Colloidal Dispersions.* Cambridge University Press, Cambridge, 1989.

C. Sanchez, D. Renard, P. Robert, C. Schmitt, and J. Lefebvre. Structure and rheological properties of acacia gum dispersions. *Food Hydrocolloids*, 16(3):257–267, 2002.

J. Scott. The historical development of theories of wave calming using oil. *History of Technology*, 3:163–186, 1978.

G. W. Scott Blair. An equation for the flow of blood, plasma and serum through glass capillaries. *Nature*, 183:613–614, 1959.

L. E. Scriven. Dynamics of a fluid interface. *Chemical Engineering Science*, 12:98–108, 1960.

D. Seuss. *Bartholomew and the Oobleck.* Turtleback Books, 1949.

V. Sharma, K. Park, and M. Srinivasarao. Colloidal dispersion of gold nanorods: Historical background, optical properties, seed-mediated synthesis, shape separation and self-assembly. *Materials Science and Engineering: R: Reports*, 65:1–38, May 2009.

V. Sharma, A. Jaishankar, Y.-C. Wang, and G. H. McKinley. Rheology of globular proteins : Apparent yield stress, high shear rate viscosity and interfacial viscoelasticity of Bovine Serum Albumin solutions. *Soft Matter*, 2011. doi: 10.1039/C0SM01312A.

I. M. Sokolov, J. Klafter, and A. Blumen. Fractional kinetics. *Physics Today*, 55(11): 48, 2002.

K. B. Song and S. Damodaran. Structure-function relationship of proteins: adsorption of structural intermediates of bovine serum albumin at the air-water interface. *Journal of Agricultural and Food Chemistry*, 35(2):236–241, Mar. 1987.

P. G. Squire, P. Moser, and C. T. O'Konski. The hydrodynamic properties of bovine serum albumin monomer and dimer. *Biochemistry*, 7(12):4261–72, Dec. 1968.

A. Stocco, E. Rio, B. P. Binks, and D. Langevin. Aqueous foams stabilized solely by particles. *Soft Matter*, 7(4):1260, 2011.

L. C. E. Struik. Free damped vibrations of linear viscoelastic materials. *Rheologica Acta*, 6(2):119–129, May 1967.

T. Svitova, M. Wetherbee, and C. Radke. Dynamics of surfactant sorption at the air/water interface: continuous-flow tensiometry. *Journal of Colloid and Interface Science*, 261(1):170–179, May 2003.

C. Tanford and J. G. Buzzell. The viscosity of aqueous solutions of Bovine Serum Albumin between pH 4.3 and 10.5. *The Journal of Physical Chemistry*, 60(2): 225–231, 1956.

N. W. Tschoegl. *The Phenomenological Theory of Linear Viscoelastic Behavior.* Springer-Verlag, New York, 1989.

T. van Vliet, A. H. Martin, and M. A. Bos. Gelation and interfacial behaviour of vegetable proteins. *Current Opinion in Colloid & Interface Science*, 7(5-6):462–468, Nov. 2002.

S. Vandebril, A. Franck, G. G. Fuller, P. Moldenaers, and J. Vermant. A double wall-ring geometry for interfacial shear rheometry. *Rheologica Acta*, 49(2):131–144, Dec. 2010.

V. L. Vilker, C. K. Colton, and K. A. Smith. The osmotic pressure of concentrated protein solutions: Effect of concentration and pH in saline solutions of Bovine Serum Albumin. *Journal of Colloid and Interface Science*, 79(2):548–566, Feb. 1981.

E. Wajnryb and J. S. Dahler. The viscosity of electrostatically stabilized dispersions of spherical colloid particles. *Journal of Colloid and iIterface Science*, 217(2):249–258, Oct. 1999.

K. Walters. *Rheometry.* Chapman and Hall, London, 1975.

J. Wang, S. M. Buck, and Z. Chen. The effect of surface coverage on conformation changes of bovine serum albumin molecules at the air-solution interface detected by sum frequency generation vibrational spectroscopy. *The Analyst*, 128(6):773, 2003.

H. A. Waterman, C. Blom, H. J. Holterman, E. J. 's Gravenmade, and J. Mellema. Rheological properties of human saliva. *Archives of Oral Biology*, 33(8):589–596, 1988.

A. K. Wright and M. R. Thompson. Hydrodynamic structure of bovine serum albumin determined by transient electric birefringence. *Biophysical Journal*, 15(2):137–141, Feb. 1975.

J. Wu and J. M. Prausnitz. Osmotic pressures of aqueous bovine serum albumin solutions at high ionic strength. *Fluid Phase Equilibria*, 155(1):139–154, Feb. 1999.

J. A. Zasadzinski, J. Ding, H. E. Warriner, F. Bringezu, and A. J. Waring. The physics and physiology of lung surfactants. *Current Opinion in Colloid & Interface Science*, 6(5-6):506–513, Nov. 2001.